AN INVESTIGATION INTO THE FLOW MECHANISM OF GAS-SOLIDS FLOW OF FINE AND DUSTY POWDERS

A THESIS SUBMITTED IN PARTIAL FULFILLMENT OF REQUIREMENT FOR THE DEGREE OF

MASTER OF TECHNOLOGY

IN THERMAL ENGINEERING

BY

KHUSRO KAMALUDDIN

REGISTRATION NO.: 801783008

UNDER SUPERVISION OF

DR. S. S. MALLICK

(ASSOCIATE PROFESSOR)

DR. ANU MITTAL

(ASSISTANT PROFESSOR)

MECHANICAL ENGINEERING DEPARTMENT

THAPAR INSTITUTE OF ENGINEERING & TECHNOLOGY, PATIALA-147004

PUNJAB, INDIA

JULY 2019

CERTIFICATION

This is to certify that the dissertation entitled **"An Investigation into the Flow Mechanism of Gas-Solids Flow of Fine and Dusty Powders"** is an authentic record of my work carried out as requirements for the award of the degree of **Master of Engineering** in **Thermal Engineering** at **Thapar Institute of Engineering and Technology, Patiala** under the supervision of **Dr. S.S. Mallick, Associate Professor and Dr. Anu Mittal, Assistant Professor, Mechanical Engineering Department**, Thapar Institute of Engineering & Technology, Patiala. No part of this thesis has been submitted for the award of any degree.

Date: 15 JULY 2019

Khusro Kamaluddin

Roll No. 801783008

Thapar Institute of Engineering and Technology, Patiala

It is certified that the above statement made by my student is correct to the best of my knowledge and belief.

Dr. S. S. Mallick
Associate Professor
Mechanical Engineering Department
T.I.E.T, Patiala

Dr. Anu Mittal
Assistant Professor
Mechanical Engineering Department
T.I.E.T, Patiala

ACKNOWLEDGEMENT

I would like to express my gratitude to my supervisors Dr. S. S. Mallick and Dr. Anu Mittal for their unconditional support and guidance throughout my research work. I have learnt a lot while working with them. This thesis work would not have been completed in time if they wouldn't have had confidence and trust in me. I would like to thank them for the environment and freedom that they gave me during my thesis work.

I would like to thank Gautam sir and Atul sir for their valuable suggestions and support throughout the various phases of my thesis work.

I was grateful to have Kapil sir and Gourav sir as my mentors who guided and supported me throughout my work. I was lucky to have Harpreet and Faiz as my colleagues who helped me in day to day activities at the lab.

I would like to thank the incharge of workshop, machine tool lab, metrology lab and venture lab for allowing me to use their facilities during my thesis work.

I would like to thank Caezen Technology, Bengaluru for providing free EDEM license for my use.

Finally, I would like to thank God and my parents for always being there for me.

ABSTRACT

Bulk solids handling of fine powders finds place in a wide variety of industries, such as mineral processing, coal-fired thermal power plants, petrochemical, food, and pharmaceutical. These industries require handling and conveying of various products such as pulverized coal & iron ore used in the blast furnace of steelmaking industries, fly-ash produced in thermal power plants and essential consumable products such as flour and powdered spices, etc used in food processing industries. Designing of such systems using simulation tools such as EDEM, provides a valuable platform. Although EDEM is well established in the areas where the particle size is large (i.e. from 10 mm to 0.5 mm) it has not been utilized in the area of fine powders (i.e. from 300 μm to 0.5 μm). In this work, an attempt has been made to simulate fundamental behavior of fine powders and validate it against experimentally obtained results.

Apart from handling equipment, design of a pneumatic conveying system is also a challenging task. The minimum amount of air required per unit weight of the material to avoid blockage in the line changes with the characteristics of the material to be conveyed. Therefore, it is a common practice to first generate the pneumatic conveying characteristic (PCC) in an experimental test rig. For the same purpose, a pilot plant was developed under an industrial research project sponsored by the National Thermal Power Corporation (NTPC) entitled *"On Developing Reliable Scale-up Procedures and Design Optimization for Pneumatic Fly Ash Conveying Systems for 500/800/1000 MW Units".* For the purpose of measurement of air flow rate required for conveying, various orifice flow meters were designed, fabricated, installed and calibrated. The equipment developed were found to be working properly.

National Thermal Power Corporation (NTPC) has experienced that in cases of rainy season/winter/high relative humidity condition with no air-drying plant installed downstream to the transport air compressor in the Ash Handling Plants in Coal-Fired Thermal Power Plants, there were cases of water droplets (dew formation) in the air stream (especially towards the end of pipeline). Thus, a case study was carried out. It was found out that for avoiding this problem, the installation of air-drying equipment is a must.

TABLE OF CONTENTS

CERTIFICATION ii

ACKNOWLEDGEMENT iii

ABSTRACT iv

LIST OF FIGURES vii

LIST OF TABLES x

NOMENCLATURE xi

CHAPTER 1 : INTRODUCTION AND OBJECTIVES 1

1.1 INTRODUCTION 1

1.2 OBJECTIVES 3

CHAPTER 2 : AIR FLOW MEASUREMENT IN PNEUMATIC CONVEYING 4

2.1 INTRODUCTION 4

2.2 PNEUMATIC CONVEYING 4

2.2.1 PRESSURE CONVEYING 5

2.2.2 VACUUM CONVEYING 5

2.2.3 PNEUMATIC CONVEYING CHARACTERISTICS (PCC) 6

2.3 NEED OF WORK 7

2.4 EXPERIMENTAL SETUP 8

2.4.1 PRESSURE CONVEYING TEST RIG 8

2.4.2 VACUUM CONVEYING TEST RIG 9

2.5 FLOW METER 9

2.5.1 ORIFICE FLOW METER 11

2.6 DESIGN OF ORIFICE FLOW METER 12

2.6.1 SELECTION OF β VALUES 12

2.6.2 MECHANICAL DESIGN 15

2.6.3 LAYOUT DESIGN 18

2.7 MANUFACTURING 20

2.8 CALIBRATION 22

2.9 FLUIDISATION AIR MEASUREMENT AT NTPC MAUDA 25

CHAPTER 3 : AN INVESTIGATION INTO THE REQUIREMENT OF AIR-DRYING PLANT IN TRANSPORT AIR SYSTEM FOR PNEUMATIC CONVEYING OF FLY ASH – A CASE STUDY 28

3.1 INTRODUCTION 28

3.2 CONVEYING CONDITION 28

3.3 MODELLING TEMPERATURE DISTRIBUTION 29
3.4 PRESSURE DEW POINT AND FLOW TRANSIENTS 32
3.5 CONCLUSION AND RECOMMENDATION 36
CHAPTER 4 : CALIBRATION OF FINE POWDER FOR DISCRETE ELEMENT METHOD 37
4.1 INTRODUCTION 37
4.2 LITERATURE REVIEW 37
4.2.1 CHARACTERIZATION OF BULK SOLIDS 37
4.2.2 DEM FUNDAMENTALS 45
4.2.3 FLOW PROPERTIES OF BULK SOLIDS 51
4.2.4 REVIEW OF PREVIOUS RESEARCH ON DEM CALIBRATION 54
4.2.5 SHORTCOMINGS OF PREVIOUS RESEARCH 58
4.3 OBJECTIVES 58
4.4 MATERIAL AND METHODS 58
4.5 SIMULATION 61
4.6 RESULTS AND DISCUSSION 65
4.7 CONCLUSION 72
CHAPTER 5 : CONCLUSION AND FUTURE SCOPE 73
5.1 CONCLUSION 73
5.2 FUTURE SCOPE 73
REFERENCES 74
COMMUNICATIONS 78
APPENDIX I 79
APPENDIX II 94

LIST OF FIGURES

Figure 2.1 : Pressure Conveying System 5

Figure 2.2 : Vacuum Conveying System 5

Figure 2.3 : Pneumatic Conveying Characteristics (PCC) 6

Figure 2.4 : Pressure Conveying Test Rig 8

Figure 2.5 : Vacuum Conveying Test Rig 9

Figure 2.6 : Beta selection graph for 3 Inch line 0.08 - 0.15 kg/s 14

Figure 2.7 : Section view of flowmeter 15

Figure 2.8 : Exploded view of flowmeter 16

Figure 2.9 : Schematic of pressure tapping 17

Figure 2.10 : Pressure transducer placed in tapping 17

Figure 2.11 : Orifice plate being replaced using jack bolts 17

Figure 2.12 : Bolt arrangement for 3-inch flowmeter 18

Figure 2.13 : Layout without conditioner 18

Figure 2.14 : Layout after adding flow conditioner 19

Figure 2.15 : Velocity streamline plot of flowmeter 19

Figure 2.16 : Flow profile at various section after flow conditioner 20

Figure 2.17 : Boring of 3-inch pipe 20

Figure 2.18 : Completely flushed pressure tapping 21

Figure 2.19 : Flow conditioners 21

Figure 2.20 : Flowmeter in 3-inch pressure line 21

Figure 2.21 : Iterative scheme for Cd calculation 24

Figure 2.22 : Calibration result for 3-inch pressure line 25

Figure 2.23 : Flow meter used in NTPC Mauda 26

Figure 2.24 : Orifice plate used at NTPC Mauda 26

Figure 2.25 : Calibration curve 27

Figure 2.26 : Flowmeter installed at NTPC Mauda 27

Figure 3.1: Control flow of air-ash flow through pipe 29

Figure 3.2: Variation of gas temperature along with distance from blow tank (winter season) 32

Figure 3.3: Variation of gas temperature along with distance from blow tank (monsoon season) 32

Figure 3.4: Typical pressure fluctuation curves for pneumatic conveying of powders (Mittal and Mallick, 2016) 34

Figure 3.5: Temperature of transport air and pressure dew point lines (with and without transient effects) with an increase in distance from blow tank (winter season) 35

Figure 3.6: Temperature of transport air and pressure dew point lines (with and without transient effects) with an increase in distance from blow tank (monsoon season) 35

Figure 4.1 : Particle Size Distribution 39

Figure 4.2 : Roundness 40

Figure 4.3 : Quantitative roundness scale(Powers, 1953) 41

Figure 4.4 : Different type of voids in particle 42

Figure 4.5 : Static angle of repose(Fraczek, Złobecki and Zemanek, 2007) 44

Figure 4.6 : Dynamic angle of repose(Kanakabandi and Goswami, 2019) 44

Figure 4.7 : Collison Modelling(Reza Norouzi *et al.*, 2016) 46

Figure 4.8 : Square-well method for interarticular forces(Reza Norouzi *et al.*, 2016) 47

Figure 4.9 : Schematic of two colliding particles and forces acting on them(Reza Norouzi *et al.*, 2016) 49

Figure 4.10 : Viscoelastic model(Reza Norouzi *et al.*, 2016) 50

Figure 4.11 : Normal pressure distribution in contact area of an elastic sphere(Reza Norouzi *et al.*, 2016) 50

Figure 4.12 : Uniaxial Compression Test(Schulze, 2010) 52

Figure 4.13 : Bulk density as a function of consolidation stress(Schulze, 2010) 52

Figure 4.14 : Unconfined yield stress as a function of consolidation stress(Schulze, 2010) 53

Figure 4.15 : Effect of consolidation time on flow function(Schulze, 2010) 53

Figure 4.16 : Instantaneous flow function along with constant flow function lines(Schulze, 2010) 54

Figure 4.17 : Brookfield Powder Flow Tester 59

Figure 4.18 : Bulk density vs normal stress for APH fly ash 60

Figure 4.19 : 3D model of PFT trough 61

Figure 4.20 : 3D model of PFT top lid (507) 61

Figure 4.21 : Trough filling 61

Figure 4.22 : Filled trough ready for compression 62

Figure 4.23 : Top lid compressing the particles 62
Figure 4.24 : Output from PFT trough simulation 63
Figure 4.25 : Cylinder dimensions 63
Figure 4.26 : Cylinder ready for compression 64
Figure 4.27 : Circular lid compressing the particles 64
Figure 4.28 : Comparison of trough and cylinder data 64
Figure 4.29 : Effect of particle density on bulk density test 65
Figure 4.30 : Effect of particle size on bulk density test 66
Figure 4.31 : Effect of shear modulus on bulk density test 66
Figure 4.32 : Effect of Poisson's ratio on bulk density test 67
Figure 4.33 : Effect of coefficient of restitution on bulk density test 68
Figure 4.34 : Effect of coefficient of static friction on bulk density test 68
Figure 4.35 : Effect of coefficient of rolling friction on bulk density test 69
Figure 4.36 : Tetrahedral Particle 70
Figure 4.37 : Effect of particle shape on bulk density test 70
Figure 4.38 : Calibration of bulk density test using spherical particles 71
Figure 4.39 : Calibration of bulk density using tetrahedral particle 71

LIST OF TABLES

Table 2.1 : Flow Range for Flow Meter 13

Table 2.2 : Coefficient of discharge values for various flow meters 25

Table 4.1 : Particle density definitions 42

Table 4.2 : Bulk properties for APH fly ash 59

Table 4.3 : Bulk density test for APH fly ash 60

Table 4.4 : Data query parameters 62

Table 4.5 : Geometric parameters of tetrahedral shape 70

NOMENCLATURE

English Symbols

T_0	Ambient Temperature [°C/K]
A	Area [m^2]
C_d	Coefficient of discharge
e	Coefficient of restitution
h_i	Convection coefficient inside the pipe [$W/m^2.K$]
h_o	Convection coefficient outside the pipe [$W/m^2.K$]
D	Diameter [m]
$D_{tapping}$	Diameter of tapping [mm]
θ	Excess temperature [°C]
f	Force [N]
F	Force [N]
$\vec{f}_i$	Force vector acting on i^{th} particle [N]
g	Gravity[m/s^2]
H	Height [m]
$\vec{J}$	Impulse [N.s]
h_1	Incoming specific enthalpy [J/kg]
ID	Internal Diameter [m]
L	Length [m]
m	Mass [kg]
q_m	Mass flow rate [kg/s]
m_i	Mass of i^{th} particle [kg]
$\vec{M}_{ij}$	Moment acting on the i^{th} particle due to j^{th} particle [Nm]
I_i	Moment of inertial of the i^{th} particle [kg/m2]
$\vec{n}_{ij}$	Normal vector from i^{th} particle w.r.t j^{th} particle
Nu	Nusselt number
h_2	Outgoing specific enthalpy [J/kg]
U	Overall heat transfer coefficient [$W/m^2.K$]
p	Perimeter [m]
x	Position [m]
$\vec{x}_i$	Position vector of the i^{th} particle
Δp	Pressure drop [Pa]
r, R	Radius [m]
r	Radius [m]
E_{out}	Rate of Energy Transfer going outside control volume [W]
E_{in}	Rate of Energy Transfer into the control volume [W]
Re_D	Reynolds Number corresponding to diameter D
G	Shear Modulus [Pa]
R	Specific Gas Constant for Air [0.287 KJ/Kg.K]
C_p	Specific Heat [J/kg.K]
s	Spring stiffness [N/m]
$\vec{t}_{ij}$	Tangential vector between the i^{th} and j^{th} particle
H_t	Tapping height [mm]
T	Temperature [°C]
ΔT	Temperature difference [°C]

K_m	Thermal Conductivity of pipe material [W/m.K]
t	Time [s]
$\vec{v}_i$	Velocity of the i^{th} particle [m/s]
$\vec{v}_{ij}$	Velocity vector of the i^{th} particle with respect to j^{th} particle
V	Volume[m^3]
E	Young's Modulus [Pa]

Greek Symbols

$\vec{\varphi}_i$	Angular position vector of the i^{th} particle
$\vec{\omega}_i$	Angular velocity vector of the i^{th} particle
μ	Coefficient of Friction
η	Dampening coefficient
ρ	Density [kg/m^3]
β	Diameter Ratio
μ	Dynamic Coefficient of Viscosity [Pa.s]
ε	Expansibility factor
κ_0	Frequency of undamped harmonic oscillator [Hz]
α	Friction angle [deg]
γ	Isentropic coefficient
Δx	Length of control volume [m]
σ_1	Normal stress [N/m^2]
δ	Overlap [m]
π	Pi
ν	Poisson's Ratio
ψ	Reduced damping coefficient
ϕ	Relative Humidity
k_o	Thermal conductivity of water [W/m.K]

Subscripts

b	Bulk
c	Consolidation
ca	Contact Area
$diss$	Dissipation
x	Distance in direction of flow [m]
eff	Effective
el	Elastic
f	Final
2	Final
ff	Flow function
ash	Fly ash
in	Incoming
i	Initial
1	Initial
l	Load
max	Maximum
min	Minimum

mix	Mixture
n	Normal
out	Outgoing
p	Particle
$p-w$	Particle-wall
sat	Saturation
s	Surface Area
t	Tangential
t	Total
v	Volume

Superscripts

c	Collision
ext	External
1	Final
$f-p$	Fluid-particle
0	Initial
$p-p$	Particle-particle
r	Radial
t	Tangential

Abbreviations

APH	Air Preheater
$ASTM$	American Society for Testing and Materials
BST	British Standard Tap
CFD	Computational Fluid Dynamics
DPT	Dew Point Temperature [°C]
DBT	Dry Bulb Temperature [°C]
FAD	Free Air Delivery
ISO	International Organization for Standardization
$NTPC$	National Thermal Power Corporation Limited
NB	Nominal Bore [m]
PSD	Particle Size Distribution
PCC	Pneumatic Conveying Characteristics
PFT	Powder Flow Tester
PMC	Pressure Minimum Curve
SMD	Sauter Mean Diameter [m]
WBT	Wet Bulb Temperature [°C]
ZFC	Zanker Flow Conditioner

CHAPTER 1 : INTRODUCTION AND OBJECTIVES

1.1 INTRODUCTION

Bulk solids handling of fine powders finds place in various industries. These products range from pulverized coke and iron ore used in blast furnace in steelmaking industries, fly ash produces in thermal power plants and to essential products that find significant importance in our daily life such as powdered spices. For guaranteeing the quality of fine powder products and the system performance, it is imperative that one has an effective bulk solid handling system. Which requires a proper understanding of the product at macro and micro level followed by proper designing of the system such that while maintaining the quality of the fine powder product whether it may be paracetamol powder for tablet making or dry fly ash used for making cement, the system remains energy efficient, without having harmful effect on the environment and minimal material wastage.

Pneumatic conveying of bulk solids is a bulk solid handling technique where the bulk solids are conveyed by the use of air. It can be by using compressed air i.e. in the case of pressure pneumatic conveying or by the use of vacuum i.e. in the case of vacuum conveying. The amount of air required in pneumatic conveying is an important operational parameter. If an excessive amount of air is used, the material is properly conveyed but the operational cost increases and on the other hand, if the amount of air is too low then the air is not able to move the material thus causing a blockage. Thus, it is important to select an appropriate air flow rate. This flow rate is affected by a variety of bulk and particle properties. Thus, the best method to design a pneumatic conveying system is to first convey the material in a test rig and study the behavior of the material. Then the results obtained are scaled up and used for the actual system. In the present work airflow measurement equipment was designed, manufactured and calibrated for use in a pneumatic conveying test rig at Thapar Institute of Engineering and Technology, Patiala under and an NTPC sponsored industrial project entitled *"Developing Reliable Scale - up Procedures and Design Optimization for Pneumatic Fly Ash Conveying Systems for 500/800/1000 MW Units"*

A case study was carried out to determine the cause of dew formation inside the pneumatic conveying pipeline in NTPC thermal power plants during winter and monsoon season. Air drying plant for the pneumatic conveying system at NTPC power plants was not supplied by the suppliers. The suppliers were of the opinion that such a situation should not happen. But

NTPC understood that the formation of dew or moisture in the pipeline can cause agglomeration of particles which can lead to pipe blockage. Even if the blockage doesn't take place the pressure drop along the length of pipeline would increase due to the formation of particle layers inside the pipeline. Thus, the matter was investigated.

Appropriate designing of bulk solids handling equipment is in itself a tedious task, but when handling fine powders, the design of the same equipment becomes even more demanding. The reason behind it is that when particles are coarse in nature, they tend to flow easily but as the size of the particles in the powder reduces the flowability reduces. This is due to the fact that fine powders are more cohesive in nature(Schulze, 2010). The reason for such behavior is the increase in the particle-particle interactions in the fine powder. For the same amount of coarse powder, the number of particles is higher in fine powders, due to this the interparticle forces which were negligible in coarse grain powders become predominant in case of fine powder(Schulze, 2010). These forces include van der Waals forces, electrostatic force, the formation of liquid bridge etc.

Although a large number of collision models are available that can be used to model the behaviour of fine powders and simulation packages like LIGGGHTS, YADE and EDEM make it very easy to run to apply these collision models to a large number of particles in dynamic situations. But modelling of these particles is a challenging task. This is because of two reasons. First of all, it is difficult to measure certain particle properties such as coefficient of restitution (i.e. particle-particle, particle-equipment), shear strength, Young's modulus, Poisson's ratio, rolling and sliding friction (i.e. particle-particle, particle-equipment). Secondly, where the properties can be easily measured (like particle density, etc.) proper results are not obtained by using such properties due to the complex nature of flow and contact mechanics. The particle and the bulk properties that are measured during the characterization tests are not the same as that which exist during the actual flow conditions.

Modelling of a particle in such a way that the bulks properties exhibited by it are similar to the bulk solid at hand is termed as calibration in DEM simulation. One of the most popular method of calibration is to conduct bulk solids experiments and then replicate the findings in simulation software. In most of the calibration techniques simple test that can mostly be attributed to angle of repose test by various means are used such as rotating drum, baffled rotating drum(Marigo and Stitt, 2015), angle of repose by emptying(Derakhshani, Schott and Lodewijks, 2015),

piling(Alizadeh *et al.*, 2018) and pouring(Rackl and Hanley, 2017; Roessler and Katterfeld, 2019) method.

In this work, the author has made an attempt to calibrate DEM parameters for fine powders by using powder flow tester (PFT) machine. The bulk density test was simulated on the EDEM software package. The effect of various particle properties on the bulk density test was studied. The simulation results were compared against practically obtained results.

1.2 OBJECTIVES

1. Design, fabrication, and installation of air flow meter for pressure and vacuum pneumatic conveying system.
2. To measure the fluidization air in pneumatic conveying system at NTPC power plant at Mauda, Maharashtra.
3. To simulate bulk density test in EDEM and then validate the simulation results against practical results.

CHAPTER 2 : AIR FLOW MEASUREMENT IN PNEUMATIC CONVEYING

2.1 INTRODUCTION

Pneumatic conveying of bulk materials finds its application in various industries such as power plants, steelmaking industries, pharmaceutical industries, etc. In many cases these system work round the clock throughout the year. Thus, it is important that these systems are reliable and deliver a certain level of performance throughout their operation. This reliability in the performance can be ensured only if the system design is robust. Designing of such a system requires an understanding of the material both at the particle and the bulk level. And, it is after carefully understanding the properties of the bulk material, that an adequate system can be designed. As the mechanism in pneumatic conveying is multiphase flow, there are many ways that errors can creep into the design in one form or another. Thus, to have a trustworthy system design, the best way is to convey the bulk material into a test rig and understand it's behavior before finalizing the design. This completely eliminates any chance of over or underprediction of the parameters that might have taken place if the pure theoretical calculation were to be used. Although the satisfactory performance of a pneumatic conveying system relies on a number of operating parameters which must be properly designed and controlled. Amount of air flow is one of the critical parameters to be critically monitored and controlled to ensure that the required amount of product has been conveyed.

In the present work airflow measurement equipment was designed, manufactured and calibrated for use in a pneumatic conveying test rig at Thapar Institute of Engineering and Technology, Patiala under and an NTPC sponsored industrial project entitled *"Developing Reliable Scale - up Procedures and Design Optimization for Pneumatic Fly Ash Conveying Systems for 500/800/1000 MW Units"*

2.2 PNEUMATIC CONVEYING

Pneumatic conveying is bulk solids transportation technique in which the bulk material is transported in closed conduits via the use of compressed air or vacuum. When using compressed air, the material in the pipeline is pushed towards the delivery point, this is known as positive pressure or pressure conveying. While in vacuum or negative pressure pneumatic

conveying the material is sucked towards the delivery point by developing a negative gauge pressure towards the end of the pipeline.

2.2.1 PRESSURE CONVEYING

In the pressure conveying system the compressor is placed just before the blowtank. It sucks air from the atmosphere and discharges it so that the compressed air pushes the material that falls into the pipeline from the blow tank. This mixture of air and bulk material finally reaches the silo for storage of the material and further discharge. A bag filter is attached to the silo make sure that only air leaves the silo.

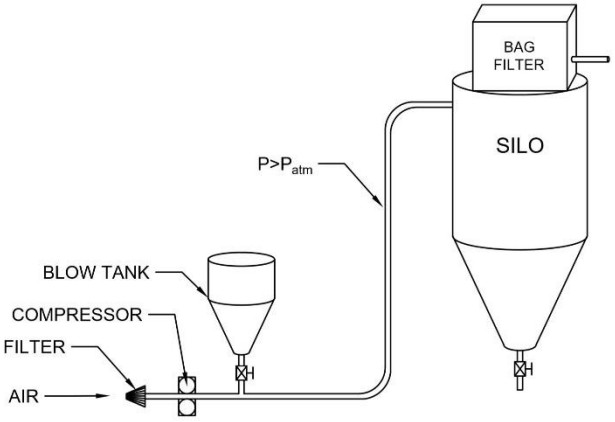

Figure 2.1 : Pressure Conveying System

The inner surface of the pipeline and the bends in the transport pipeline tend to restrict the flow of material and there is associated pressure drop. Thus it is important that the pressure of air discharged by the compressor can overcome this obstruction. In case of positive pressure conveying we deal with positive pressure thus there is no practical upper limit of the pressure of air that can be supplied. Thus the material can be conveyed to a comparatively larger distance.

2.2.2 VACUUM CONVEYING

Vacuum conveying employs a vacuum pump that creates a negative gauge pressure towards the bag filter and remote silo. This causes the air to flow beneath the blow tank due to the pressure differential. This air then carries the material that enters the pipeline from the blow tank to the remote silo.

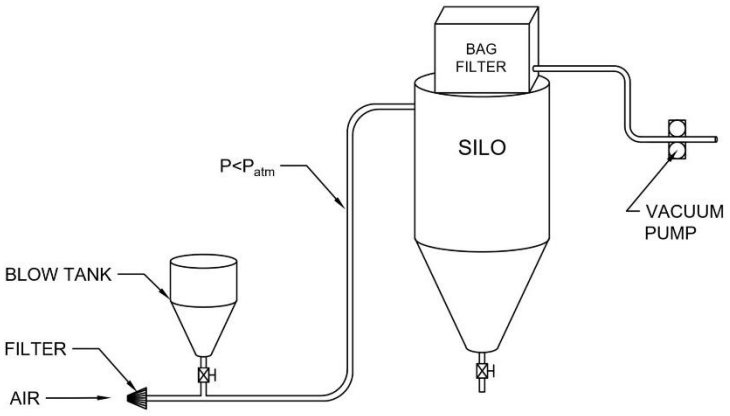

Figure 2.2 : Vacuum Conveying System

Theoretically, the maximum pressure drop that can be developed across the vacuum conveying system is limited to 1 atm. This limits the distance to which the material can be conveyed along with the rate of material transport. Thus, vacuum conveying is usually used cases where that distance to be conveyed is less and the material is prone to contamination.

2.2.3 PNEUMATIC CONVEYING CHARACTERISTICS (PCC)

The pneumatic conveying characteristics of a particular material is developed by conducting various pneumatic conveying experiments. The vertical axis denotes the pressure drop across the pipeline while the horizontal axis denotes the mass flow rate of air that is used for conveying.

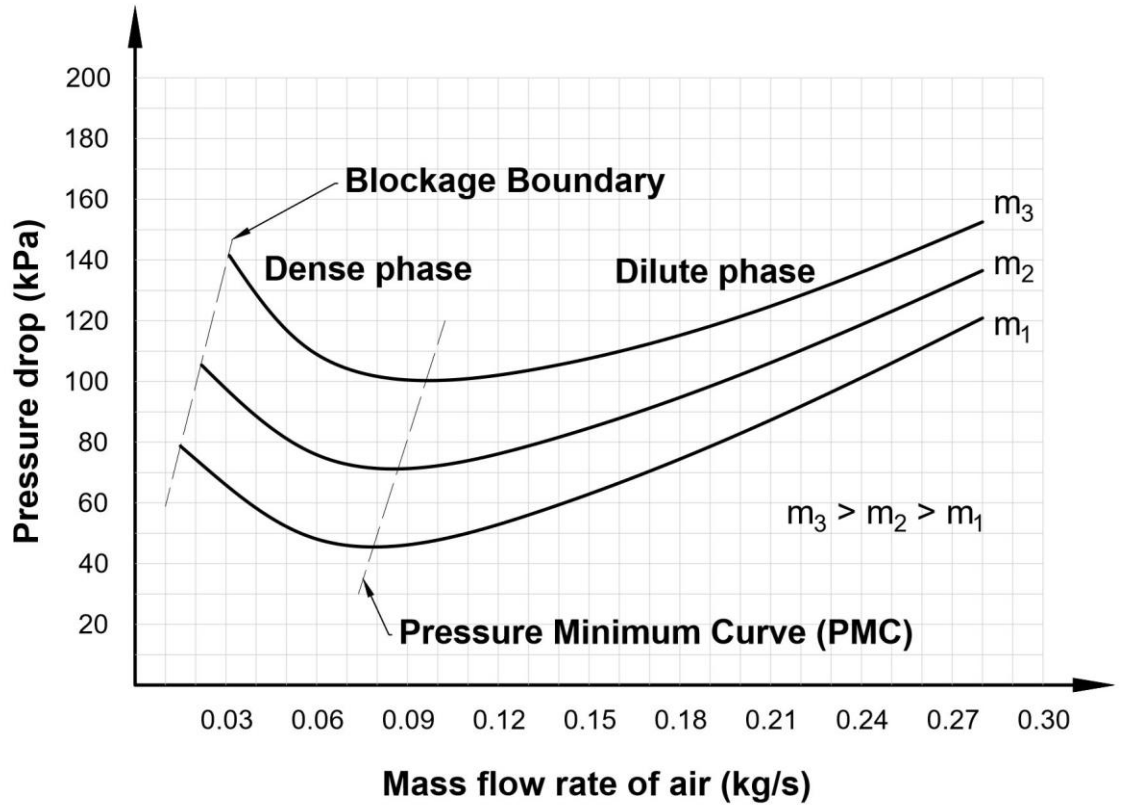

Figure 2.3 : Pneumatic Conveying Characteristics (PCC)

The three curves denote the conveying for three different material mass flow rates in ton/hr. The curve at the top corresponds the maximum material mass flow rate while the bottom curve corresponds to the minimum material mass flow rate. As the air flow rate decreased the pressure drop decreases followed by a steep rise. The locus of the minimum pressure drop is known as the pressure minimum curve (PMC). For larger material flow rate the PMC shifts to the right. As the mass flow rate further decreases below PMC the pressure drop increases up to a point

where the momentum provided by air to the material is insufficient for it to flow. This causes the material to start piling up in the pipeline, thus causing a pipeline blockage. The blockage boundary is a vague representation of the working region prone to blockage.

The region between the blockage boundary and the pressure minimum curve is known as the dense phase. Here the conveying takes place with the minimum required amount of air. Here more material is conveyed per kg of air hence called dense phase. Not all materials can be conveyed in the dense phase. Only the materials that can be fluidized(i.e. have air retention capability) can be conveyed in dense phase pneumatic conveying. (Geldart, 1973) has classified these materials as Geldart A type materials.

It is always possible to supply a large amount of air to convey material but this requires large compressor work. This comes at the expense of a large amount of energy, thus making the transport inefficient. Thus, it is preferred to supply the minimum amount of air for conveying, but also maintaining a safe margin from the blockage boundary. Thus, efficient utilization of compressed air demands for dense phase mode of conveying. However, to obtain the exact location of the blockage boundary and PMC it is essential that one has reliable test facilities and accurate scaling up techniques to estimate these operating conditions.

2.3 NEED OF WORK

It was found that the air flow meters previously used in the test rig i.e. Vortex Flow Meter was not very reliable for measuring air flow in pneumatic conveying. This is because of the fact that the air flow in pneumatic conveying is not steady and very erratic in nature. Due to the varying discharge of powder from the blow tank to the pipeline. This material discharge keeps changing in a fraction of seconds. Thus, producing high fluctuations in the air flow in the pipeline. Therefore, there was a requirement of a robust air flow measurement device that would take measurements accurately and not require re-calibration at after small intervals of time.

Moreover, two other types of air streams that are required for the proper working of blowtank apart from conveying air. These are fluidization air and top/side air. Fluidization air is the air that is made to flow through fluidizing pads at the bottom to facilitate easy flow of the material. Top/side air is the air that is required to balance the pressure of the blow tank along the conveying line to avoid backflow of air in blow tank during conveying. It was required to

design and develop accurate air flow measuring device for all the three streams (i.e. conveying air, fluidizing air, and top air).

2.4 EXPERIMENTAL SETUP

Although the basic components were the same as in a typical pneumatic conveying setup. Many measurement sensors were provided for extracting valuable data in the test rig. Unlike the system used in actual powerplants for fly ash conveying, the test rig was a closed loop pipeline. This allows the material to flow through the pipeline again and again.

2.4.1 PRESSURE CONVEYING TEST RIG

In the pressure conveying test rig, a multilevel screw compressor *(Discharge Pressure = 7 Bar)* along with an air receiver was attached in the beginning. A flow meter was attached to the line just after the air receiver. Further arrangements were made to individually measure Fluidization and Top/Side Air. Conveying pipeline were fitted with pressure transmitters, the data from which would be used for modelling solid friction factor and further developing PCCs. Both receiver bin and blow tank were mounted on load cells for measuring the material discharge rates.

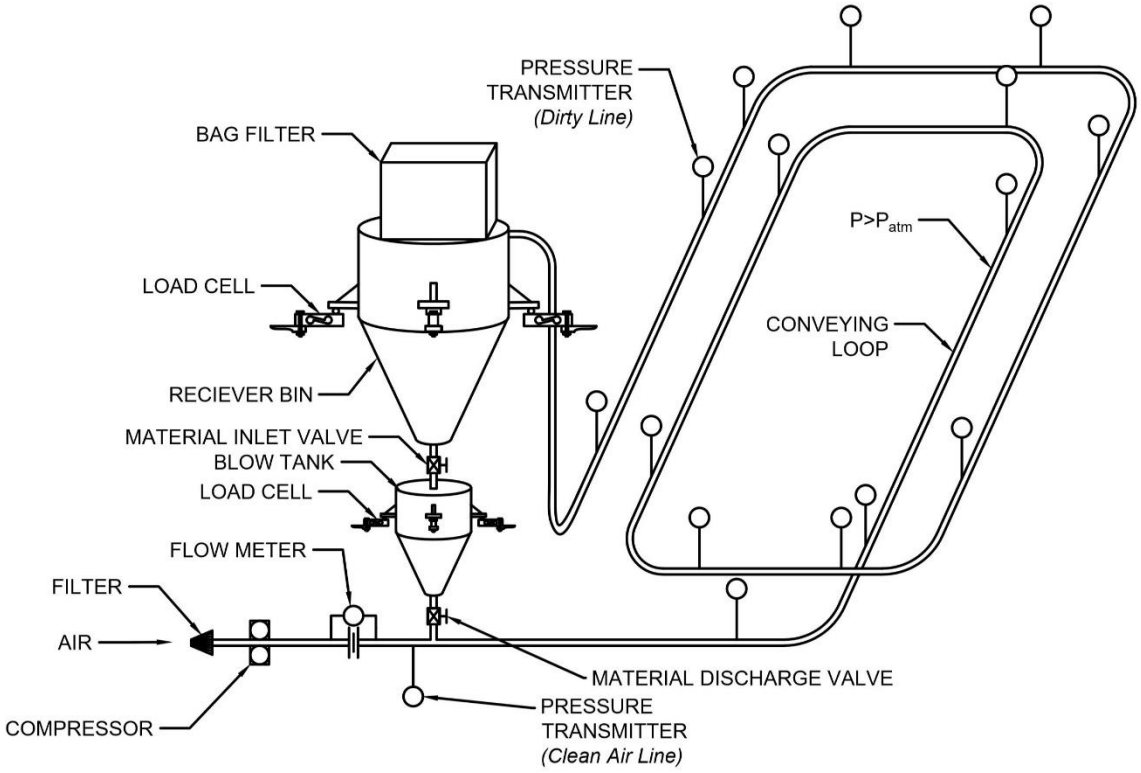

Figure 2.4 : Pressure Conveying Test Rig

2.4.2 VACUUM CONVEYING TEST RIG

The vacuum conveying test rig consists of a vacuum pump capable of producing 85 kPa vacuum attached to the bag filter. This vacuum pump generates suction in the receiver bin. This, in turn, causes the air to flow in the pipeline below the blow tank. The flowmeter just before the blow tank measures the amount of air flowing in the pipeline. The receiver bin and the transfer hopper are mounted on load cells to measure the mass flow rate of material from the hoppers. Blower and heater arrangements are available to provide heated fluidization air for both receiver bin and transfer hopper.

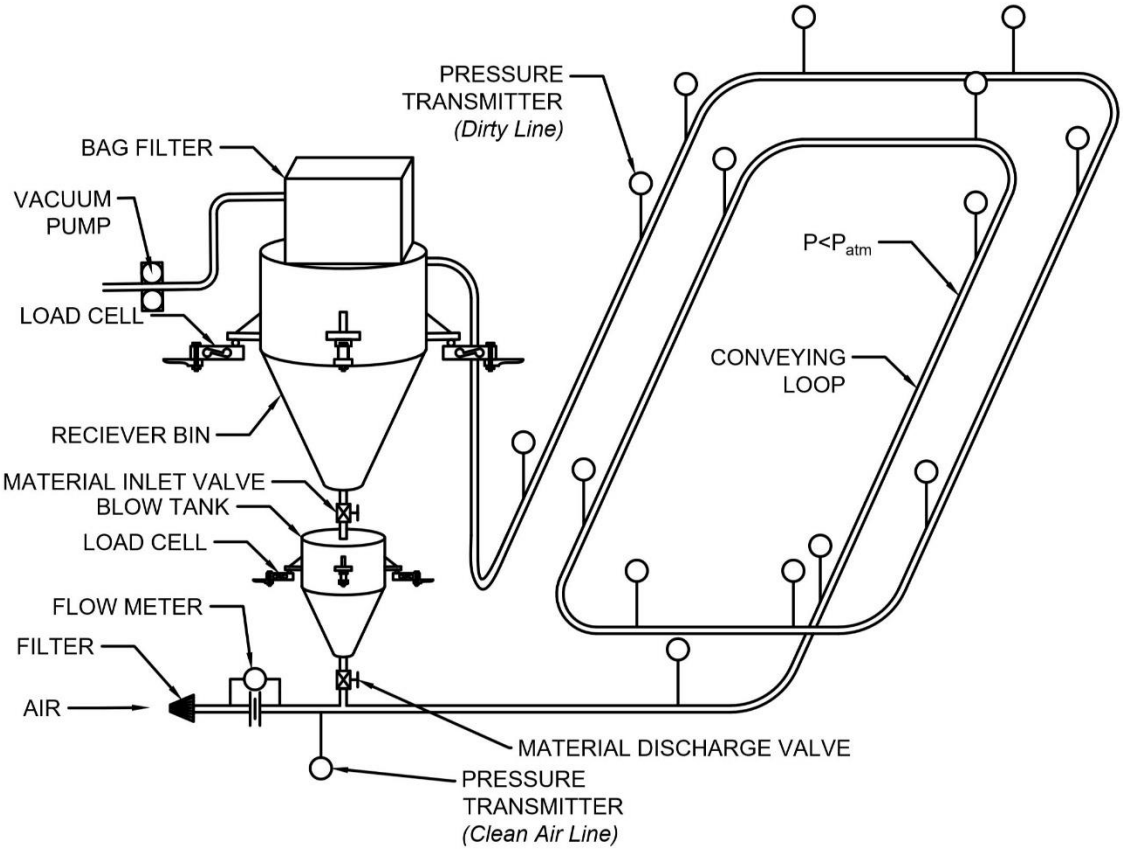

Figure 2.5 : Vacuum Conveying Test Rig

2.5 FLOW METER

Flow meter is a device which can be used to measure the discharge of a fluid in an open or closed conduit. In the present case, a closed conduit flow meter was required. These flow meters are capable to provide both the volumetric as well as mass flow values. Like all other measuring instruments, these are also based on various physical phenomena governed by the

basic laws of physics. Following are the various types of flow meters used categorized upon their working principles:

i. **Bernoulli's Principle:** Also known as variable area type flow meters. These flow meters work on the basis of Bernoulli's principle which simply means that the total energy of the fluid in motion remains constant. This property is exploited by disturbing the kinetic energy of flowing fluid, usually by an obstruction to obtain the pressure difference obtain which in turn is used to calculate the discharge. The obstruction can be provided by a slow contacting and expanding cross-section (as in venturi meter), slowly constricting and suddenly expanding cross-section(as in flow nozzle), sudden change in cross-section(as in orifice meter) or in the shape of a small pipe placed perpendicular to flow field(as in annubar).

   The advantage of such flow meters is their simple construction and working.

ii. **Electromagnetic Induction:** Usually known as mag meter, these flowmeters work on the Faraday's law of electromagnetic induction. Here a conductive fluid is made to flow inside a magnetic field perpendicular to the direction of the velocity vector. As the amount of fluid flow increases, the amount of flux increases the current produces in the fluid which in turn gives rise to the formation of potential difference in the cross-section. This voltage potential is absent if there is no flow and is directly proportional to the velocity of the fluid in the conduit. Two electrodes attached in the insulated pipe perpendicular to the plan of the velocity vector and the magnetic field are responsible for detecting the voltage produced due to the magnetic field acting on the flowing fluid. This voltage is then used to calculate the discharge of fluid.

   The disadvantage with this type of flow meter is that the fluid should be conducting in nature.

iii. **Vortex Shredding:** Also known as vortex meter, these flow meters are based on the phenomena of vortex shredding. When a buff body is introduced inside a uniform fluid flow, vortex or eddy start to emanate from either side of the buff body. The trail downstream of the buff body is known as Von Karman vortex street. As the velocity of the flow increases, the vortex start to generate more rapidly i.e. the frequency of vortex generation is proportional to the velocity of flow. This principle is employed in fluid flow measurement. A piezoelectric element is placed downstream of the buff body which generates potential difference upon encounter with a vortex thus helping to measure the frequency of vortex generation which is further used to calculate the

velocity in the conduit. This velocity is then used to finally get the flowrate of fluid in the pipeline.

The disadvantage of such flowmeters is the complex nature of physics involved and regular calibration requirement in case of pulsating flows, as the flowmeter requires a steady flow of fluid which is not available in our case.

iv. **Coriolis Effect:** In Coriolis flow meter the inertial force caused by the moving fluid is utilized for measurement of flow rate. The fluid is made to flow through an artificially oscillating U-shaped tube. As the flow through the tube starts to increase the tube starts to twist in such a way that the motion of the two arms is not in phase with each other. This phase change is sensed by extremely sensitive optical sensors. The phase change is not present when the fluid is at rest. The proportionality of phase change to mass flow is used to directly give the mass flow rate of fluid in the tube. The density can also be calculated as the frequency of the vibrations is directly proportional to the density of fluid present in the pipeline.

2.5.1 ORIFICE FLOW METER

The orifice flow meter is perhaps the most commonly used flow meter in industries. This is due to its simple construction, easy maintenance and the low cost associated with it. It belongs to the category of flowmeter that works on Bernoulli's principle. In an orifice flow meter, a flat plate with a hole present is placed in the fluid stream in order to disturb the flow of fluid.

Various type of pressure tapping can be done to measure the pressure drop across the primary device. These are flange tapping, corner tapping and D D/2 tapping.

The mass flow rate can be calculated by the following formula:

$$q_m = \frac{C_d}{\sqrt{1-\beta^4}} \varepsilon \frac{\pi}{4} d^2 \sqrt{2\Delta p \rho_1} \tag{2.1}$$

The expansibility factor (ε) is responsible for including the compressible behavior of the fluid. It depends on the pressure ratio, Reynolds number as well as the isentropic coefficient of fluid. Its value is unity for incompressible fluid and less than unity for a compressible fluid.

The empirical formula for computing the expansibility/expansion factor (ε) is for the three types of tapping arrangements is given by :

$$\varepsilon = 1 - (0.351 + 0.256\beta^4 + 0.93\beta^8)\left[1 - \left(\frac{p_2}{p_1}\right)^{\frac{1}{\gamma}}\right] \tag{2.2}$$

2.6 DESIGN OF ORIFICE FLOW METER

The designing of the flowmeter can be broadly differentiated into two process

i. Selection of β values for the different flow meters.
ii. Mechanical design of the flow meter and its assembly.
iii. Design of layout

Following were the flow ranges for the various type of flowmeters to be designed with their corresponding nominal diameters.

2.6.1 SELECTION OF β VALUES

The ratio of the orifice hole to the internal diameter of the pipe is represented by β. If the orifice diameter is very small there will be a huge pressure drop across and vice versa.

$$\beta = \frac{d}{D} \tag{2.3}$$

The β values were selected in such a way that the pressure drop in the line is neither too high nor too low. This was done so that the pressure drop does not reduce to such low value that the pressure transmitter cannot measure the pressure-drop accurately and in another case too high so that improper amount of pressure is supplied for conveying.

The selection of β value was restricted to a range of 0.4 to 0.7 only. The reason for having such a range was to avoid the comparatively more stringent geometrical requirements in the excluded region(ISO 5167-2, 2003).

As the flow to be measured had to be varied during experimentation. There were chances that while using single orifice of the complete range of flow condition will cause inaccuracy in measurements. This was due to the reason that pressure drop may reduce to such small levels that measurements by the pressure transmitter would be impractical or otherwise so high during high flow regions that not enough pressure would be available for conveying. This problem was solved by breaking the flow range into three regions for measurement of flow rate. These flow ranges are tabulated in Table 2.1.

Air Line	Flow Range (kg/s)
Total Air	0.01 to 0.08
	0.08 to 0.15
	0.15 to 0.20
Conveying air for pressure system	0.04 to 0.06
	0.06 to 0.12
	0.12 to .020
Fluidizing Air	0.02 to 0.04
	0.04 to 0.06
	0.06 to 0.08
Top/side Air	0.04 to 0.06
	0.06 to 0.12
	0.12 to .020
Conveying air for vacuum system	0.04 to 0.06
	0.06 to 0.12
	0.12 to .020

Table 2.1 : Flow Range for Flow Meter

The value for β for each range was determined by plotting a graph between pressure drop and the beta value. Here, the minimum and the maximum flowrates for the given range were plotted to get an idea of the minimum and maximum pressure drop respectively. Further, it was noticed that the pressure drop was also dependent on the upstream pressure of the fluid.

$$\Delta p = \frac{1}{2\rho_1}\left(\frac{4q_m\sqrt{1-\beta^4}}{C_d \varepsilon \pi d^2}\right)^2 \tag{2.4}$$

$$\rho_1 = \frac{p_1}{RT} \tag{2.5}$$

This was due to the presence of the density term in the pressure drop relation. Thus, for a higher upstream pressure, a lower pressure drop was obtained and vice-versa.

Thus, to get a wholesome image of all the parameters and their effect on the pressure drop, three different upstream pressures were also plotted to the corresponding minimum and maximum flow rates.

Then a particular β value was selected. Illustrated is the graph which was used to determine the β value for the 3-inch pressure in the flow range of 0.08 to 0.15 kg/s.

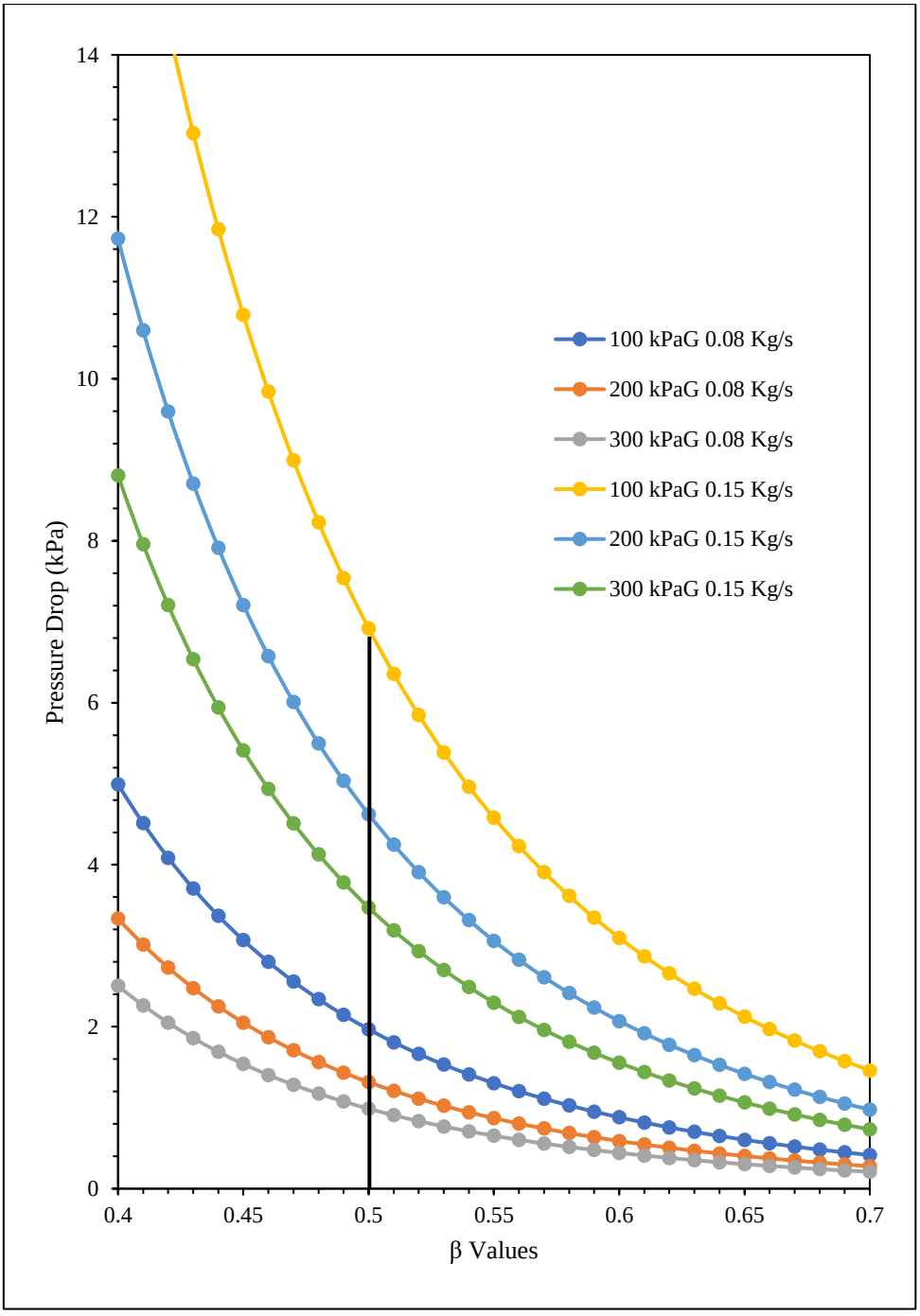

Figure 2.6 : Beta selection graph for 3 Inch line 0.08 - 0.15 kg/s

Here β was taken to be 0.5 as shown in Figure 2.6. Here the pressure drop would remain in the range of 2.5 to 6 kPa. Similarly, all the other β values were calculated. See Appendix I.

2.6.2 MECHANICAL DESIGN

2.6.2.1 Material Selection

Considering the ease of manufacturing and availability of the material, mild steel was chosen for the orifice plate housing and the pipes. SS 202 was used for manufacturing of the orifice plates. This was because of the fact that it was easier to machine and machining cost was less as compared to the first choice i.e. SS 304.

2.6.2.2 Selection of Pipe ID

The first task was to select a particular pipe schedule and a particular internal diameter. The diameter was selected so that boring of the pipe removes minimum material in a way that all the pipes have the same inner diameter. This step was very crucial because all the parameters in the calculation were based on the diameter. Further, unlike the case of stainless steel, mild steel standard (‘ISO 1239 (Part 1)’, 2004) does not have a fixed ID for a particular schedule of the pipe but has a range of acceptable diameter. The internal diameters for 2-inch and 3-inch pipes were taken as 54 mm and 83 mm respectively.

2.6.2.3 Orifice Plate Housing

The design of the flowmeters was to be done in such a way that the manufacturing cost of the equipment was minimum without compromising the performance of the flowmeter. All the major design-related decisions were taken based on BS ISO 5167-1.

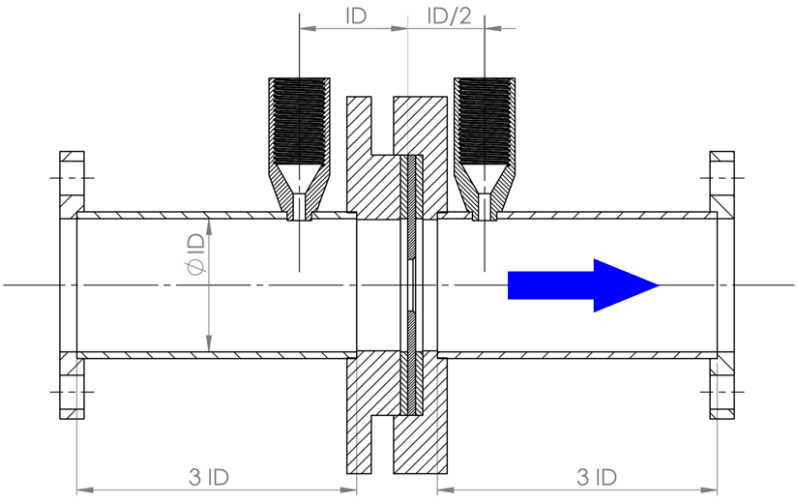

Figure 2.7 : Section view of flowmeter

The plate is pressed between the two main flanges in such a way that the plate remains perpendicular to the flow stream. A pair of gasket packs the plate in its place. The plate along with the gaskets are placed in the recess in the downstream flange and are pressed by the other flange which is protruding in nature.

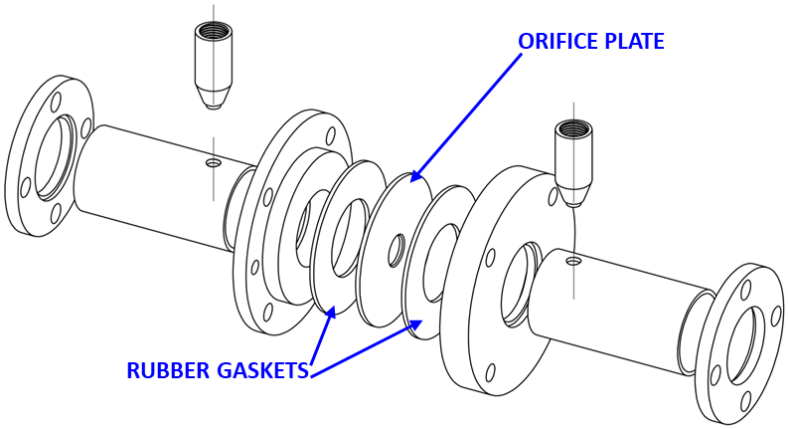

Figure 2.8 : Exploded view of flowmeter

Clause 5.2.2.7 of (ISO 5167-2, 2003) states that:

"The diameter of pressure tapping shall be less than 0,13D and less than 13 mm."

Clause 5.2.2.8 of (ISO 5167-2, 2003) states that :

"The pressure tapping shall be circular and cylindrical over a length of at least 2,5 times the internal diameter of the tapping, measured from the inner wall of the pipeline."

For Size and Height of Tapping:

ID_{MIN} = 54 mm *(for 2" Orifice Meter)*

$D_{tapping} = 0.13 \times ID_{MIN} = 0.13 \times 54$ mm = 7.02 mm

Hence, diameter of pressure tapping is taken as **5 mm** for all the pressure tappings.

Minimum Height of Tapping ($H_{t(min)}$) = 2.5 x $D_{tapping}$

$\Rightarrow (H_{t(min)}) = 2.5 \times 5$ mm = **12.5 mm**

Thus, the height of the straight section is taken as 23 mm which is far much greater than the suggested value.

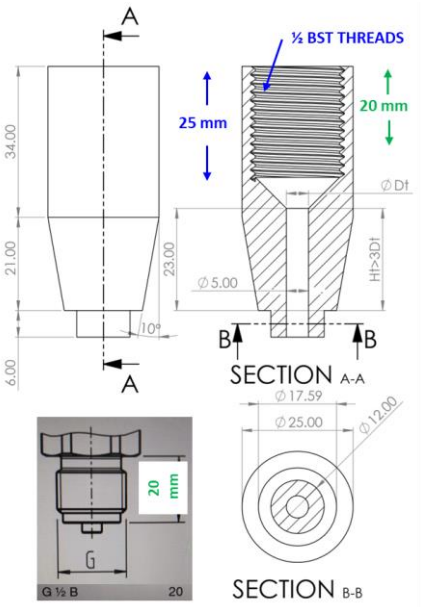

Figure 2.9 : Schematic of pressure tapping

This arrangement ensures leak-proof mounting of the plate. The D and D/2 distances are measured from the upstream face of the orifice plate. The tappings are designed in such a way that the pressure transmitters properly fit in the final assembly and do not interfere with any other part.

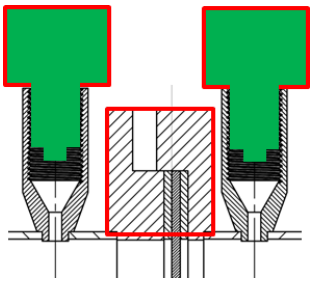

Figure 2.10 : Pressure transducer placed in tapping

Jack bolts were attached to one side of the flange so that they can be used for opening the flowmeter for changing the orifice plate.

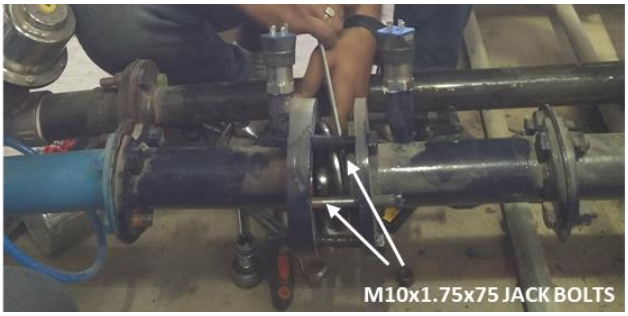

Figure 2.11 : Orifice plate being replaced using jack bolts

The flange bolts are designed on the basis of rubber gasket sealing pressure. The 2” and the 3” orifice meter flange have 4 and 8 bolts respectively. These bolts are GR8.8 Hex Bolt with 2H Heavy Hex Nut, Length= 4 Inch, Dia = ½ Inch. The bolts are a little longer in length so that when the plates are opened the flanges stay in alignment.

Figure 2.12 : Bolt arrangement for 3-inch flowmeter

2.6.3 LAYOUT DESIGN

IS 5167-2 specifies the minimum upstream and downstream straight pipe distance for orifice meter. It states that in case no flow conditioner is used there must be a minimum distance of 44 times the internal diameter of the pipeline upstream and downstream of the primary device.

Therefore,

$(L_{total})_{2Inch} \approx$ **88 x 54 = 4752 mm**

$(L_{total})_{3Inch} \approx$ **88 x 83 = 7304 mm**

These straight lengths were not possible in the designed lab layout.

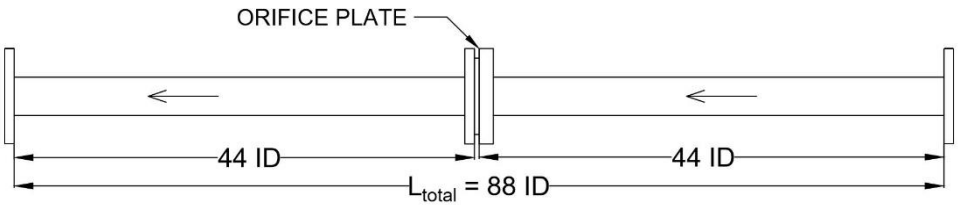

Figure 2.13 : Layout without conditioner

Thus, we decided to use a flow conditioner to reduce these lengths to acceptable levels. Flow conditioners are devices that are used to restore the flow profile in a pipeline. These are usually used to restore the profile and eliminate any swirl that the flow attains while flowing through a bend. Many types of flow conditioners are available such as 19-tube bundle straightener, Zanker flow conditioner plate, Gallagher flow conditioner, K-lab NOVA flow conditioner etc. These can be of fin type, tube type, plate type or combination of any two. In our case, the

Zanker flow conditioner plate was used due to its simple construction. Following are the function of a flow conditioner:

1. To shorten the straight pipe run
2. To restore the distorted flow profile
3. To eliminate swirl

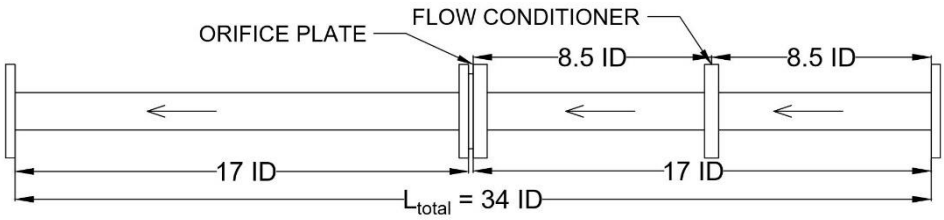

Figure 2.14 : Layout after adding flow conditioner

After using flow conditioner, the minimum distance reduces from 44 to 17 times the internal diameter. Therefore,

$(L_{total})_{2Inch}$ ≈ **34 x 54 = 1836 mm**

$(L_{total})_{3Inch}$ ≈ **34 x 83 = 2822 mm**

To ensure that the conditioner is doing its designated operation successfully a CFD simulation was carried out in the 3 Inch line with maximum flow rate. Figure 2.15 shows the results obtained.

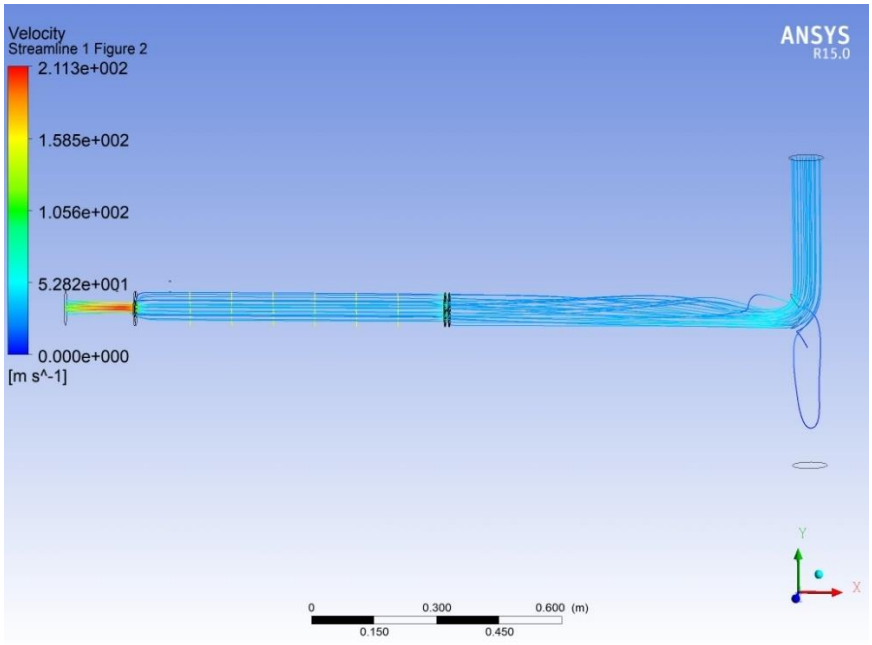

Figure 2.15 : Velocity streamline plot of flowmeter

It is evident from the result that there was no swirl present in the fluid flow downstream of the flow conditioner. The velocity profiles were measured at the sections shown in Figure 2.15. The velocity profile at these sections was plotted in Figure 2.16. It was found that the flow profile was developed and was parabolic in nature just before the orifice.

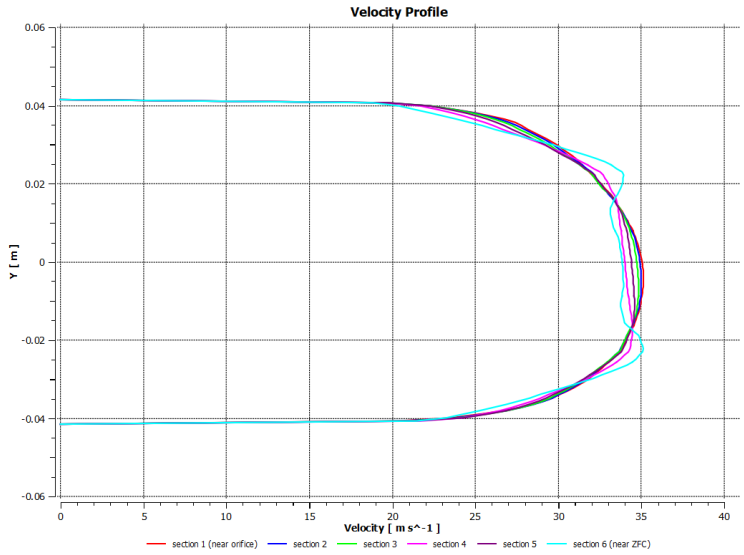

Figure 2.16 : Flow profile at various section after flow conditioner

2.7 MANUFACTURING

All of the raw materials were purchased from Ludhiana. These include the large cylindrical stocks, the thick MS plates along with the stainless steel used for orifice plates.

All the pipe lengths were bored to get exact internal diameter used for theoretical calculations.

Figure 2.17 : Boring of 3-inch pipe

The final lengths of the pipes were finished on the lathe so that no distortion takes place in the overall assembly and the pipe is always perpendicular to the plate. Tapping were made with extra protruded end. In order to get a flushed tapping at the exact D and D/2 locations. First holes were made in the pipe. Then the tappings were welded to the pipe followed by boring the

pipe to the exact internal diameter. This gave a flushed finish without any protrusion into the pipe cavity as shown in Figure 2.18.

Figure 2.18 : Completely flushed pressure tapping

The flow conditioners were made using transparency templates. The templates were used to find the exact center of the holes for punching pilot before drilling. Standard drills with diameter nearest to the calculated diameter were used for making holes in the flow conditioner. The conditioners were made from mild steel blind flanges.

Figure 2.19 : Flow conditioners

Figure 2.20 : Flowmeter in 3-inch pressure line

2.8 CALIBRATION

Calibration for orifice flow meter means the determination of its coefficient of discharge. Usually, such calibrations are required to be done by standard institutions. But as our flowmeters were large in quantity and comparably simpler to the other type of flowmeters we calibrated the flowmeters by ourselves. Hence saving the time and money required in the calibration of flowmeters from an external agency.

The empirical formula applicable to flowmeters with D and D/2 tapping is given by The Reader-Harris/Gallagher (1998) equation, subject to the condition that the flowmeter geometry conforms to the guidelines laid by (ISO 5167-1, 2003), (ISO 5167-2, 2003) and (ISO TR 9464, 1998).

The Reader-Harris/Gallagher (1998) equation:

$$C_{d_{(D>71.12\ mm)}} = 0.5961 + 0.0261\beta^2 - 0.0216\beta^8 + 0.000521\left(\frac{10^6\beta}{Re_D}\right)^{0.7} + (0.0188 + 0.0063A)\beta^{3.5}\left(\frac{10^6}{Re_D}\right)^{0.3} + (0.043 + 0.080e^{-10L_1} - 0.123e^{-7L_1})(-0.11A)\frac{\beta^4}{1-\beta^4} - 0.031\left(M'_2 - 0.8M'^{1.1}_2\right)\beta^{1.3} \quad (2.6)$$

$$C_{d_{(D<71.12\ mm)}} = 0.5961 + 0.0261\beta^2 - 0.0216\beta^8 + 0.000521\left(\frac{10^6\beta}{Re_D}\right)^{0.7} + (0.0188 + 0.0063A)\beta^{3.5}\left(\frac{10^6}{Re_D}\right)^{0.3} + (0.043 + 0.080e^{-10L_1} - 0.123e^{-7L_1})(1 - 0.11A)\frac{\beta^4}{1-\beta^4} - 0.031\left(M'_2 - 0.8M'^{1.1}_2\right)\beta^{1.3} + 0.011(0.75 - \beta)\left(2.8 - \frac{D}{25.4}\right) \quad (2.7)$$

Where,

$\beta(= d/D)$ is the diameter ratio, with the diameters d and D expressed in millimeters

Re_D is the Reynolds number calculated with respect to D

$L_1(= l_1/D)$ is the coefficient of the distance of the upstream tapping from the upstream face of the plate and the pipe diameter

$L'_2(= l'_2/D)$ is the coefficient of the distance of the downstream tapping from the upstream face of the plate and the pipe diameter

$$M'_2 = \frac{2L'_2}{1-\beta} \tag{2.8}$$

$$A = \left(\frac{19000\beta}{Re_D}\right)^{0.8} \tag{2.9}$$

It can be observed that there are two variants of the formula one which is for D<71.12mm (used for 2-inch line) and one which is for D>71.12mm (used for 3-inch line).

It can be observed that the value of C_d depends on β, Re_D, D, L_1, and L'_2.

For D and D/2 tappings:

$$L_1 = 1 \tag{2.10}$$

$$L'_2 = 0.47 \tag{2.11}$$

Thus,

$$C_d = f(\beta, Re_D, D) \tag{2.12}$$

For a particular flowmeter, the internal pipe diameter(D) and the orifice diameter are already defined.

$$Re_D = \frac{\rho V D}{\mu} = \frac{4q_m}{\pi \mu D} \tag{2.13}$$

$$\mu = f(T) \tag{2.14}$$

Therefore, assuming temperature to be constant,

$$C_d = f(q_m) \tag{2.15}$$

Also, from equation (2.1),

$$q_m = f(C_d, \beta, D, \varepsilon, \rho, \Delta p) \tag{2.16}$$

$$\varepsilon = f(\beta, \Delta p, p_1, \gamma) \tag{2.17}$$

Thus, it can be pointed out that q_m depends on C_d which intern depends on the value of q_m .

Hence to calculate the value of C_d an iterative scheme was employed using solver in MS Excel.

For the calibration process a guess value of q_m along with values d, D, p_1, p_2 and T were required.

The iterative scheme use has been shown in Figure 2.21.

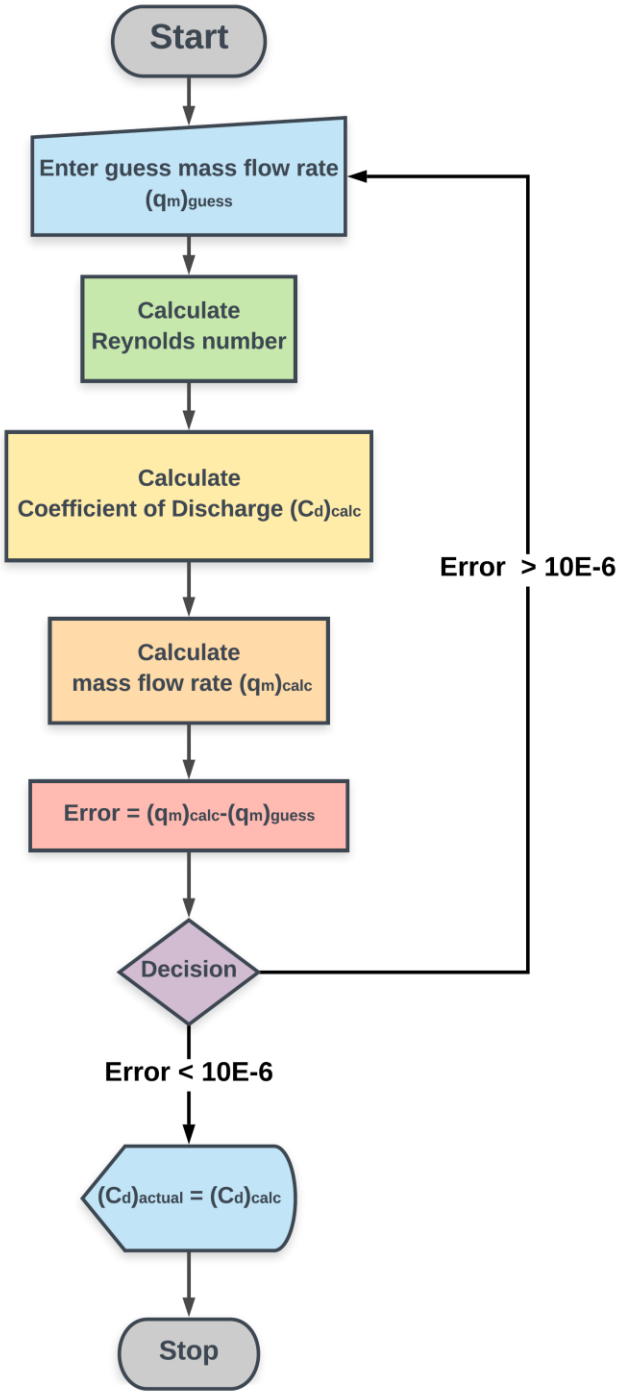

Figure 2.21 : Iterative scheme for Cd calculation

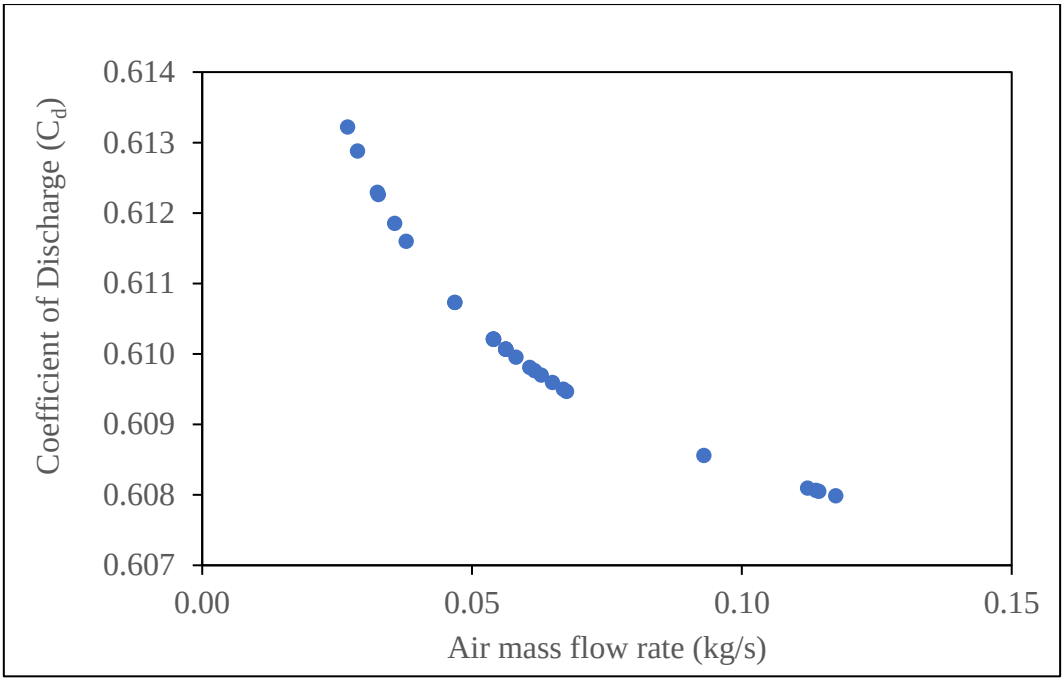

Figure 2.22 : Calibration result for 3-inch pressure line

The coefficient of discharge values for various flow metes are tabulated in the table below. A particular value was selected from a range of Cd value as given by graphs like Figure 2.22. Thus, finally obtaining a value that can be used for future calculation in the pneumatic conveying setup.

Location	Line size	B value	C_d
Pressure Line	3 inch	0.40	0.61018
Conveying Air	2 inch	0.70	0.61100
Top/Side Air	2 inch	0.55	0.61202

Table 2.2 : Coefficient of discharge values for various flow meters

2.9 FLUIDISATION AIR MEASUREMENT AT NTPC MAUDA

During a visit to an NTPC thermal power plant in Mauda, Maharashtra it was required to measure the air flow rate in the fluidization line of blow tank of the pneumatic conveying system. The vortex flowmeter available at our lab was of limited range and required external power for its functioning. Thus, an orifice flow meter was designed and manufactured in a very limited amount of time.

Figure 2.23 : Flow meter used in NTPC Mauda

The manufacturing was done in 3 days and the orifice plate used for this flow meter was made from a mild steel blind with square bevel edge. The flow meter was to be used on a 2-inch line. D and D/2 tapping were used.

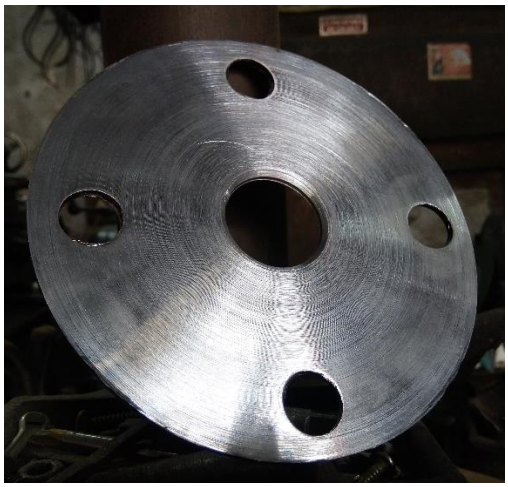

Figure 2.24 : Orifice plate used at NTPC Mauda

Due to lack of time, the flow meter was calibrated in the lab by using previously available flow meter. Pressure transducers were attached to the tapping for pressure drop measurement. Different readings were taken by varying the air flow. The mas flow rate was plotted against *X*. This was done to get a linear relationship between the two values. Both the terms in *X* were dependent on the upstream pressure.

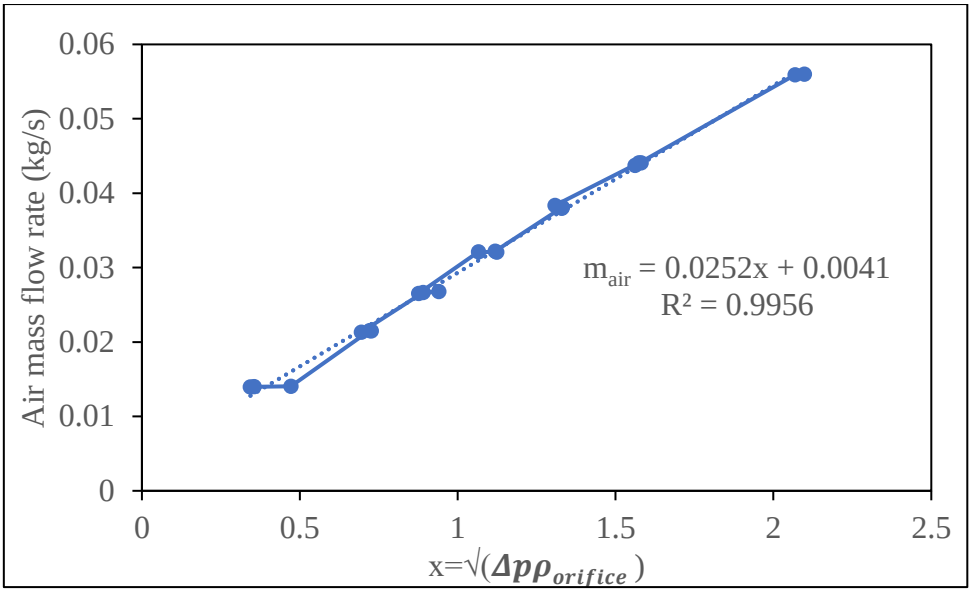

Figure 2.25 : Calibration curve

The equation for obtaining the mass flow rate was reduced to:

$$q_m = K\sqrt{2\Delta p \rho_1} \tag{2.18}$$

Thus, for measurement of air flow rate the upstream and downstream pressure was measured. Density was calculated using ideal gas equation. The calculated root term was used in the equation below to find the air flow rate.

$$m_{air} = 0.0252x + 0.0041 \tag{2.19}$$

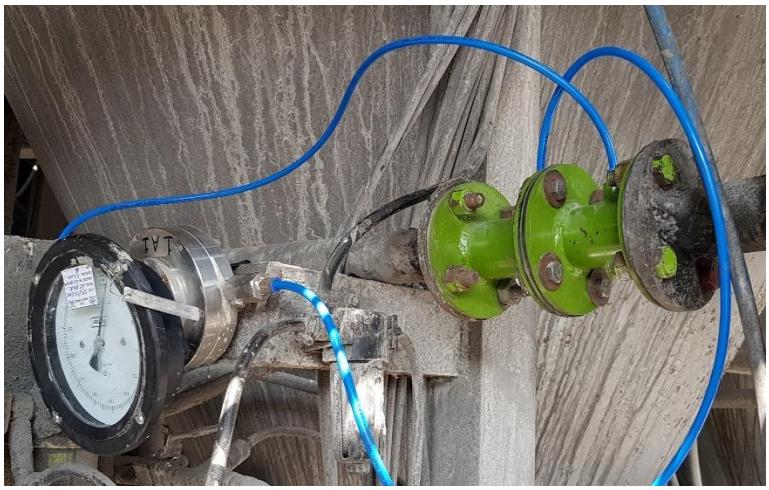

Figure 2.26 : Flowmeter installed at NTPC Mauda

The flow rate in the fluidization line was found to be 0.12 kg/s which was 5.64% of the total compressed air.

CHAPTER 3 : AN INVESTIGATION INTO THE REQUIREMENT OF AIR-DRYING PLANT IN TRANSPORT AIR SYSTEM FOR PNEUMATIC CONVEYING OF FLY ASH – A CASE STUDY

3.1 INTRODUCTION

National Thermal Power Corporation (NTPC) has experienced that in cases of rainy season/winter/high relative humidity condition with no air-drying plant installed downstream to the transport air compressor in the ash handling plants in coal-fired thermal power plants, there are chances of water droplets (dew formation) in the air stream (especially towards the end of pipeline). NTPC explained that certain ash handling supplier(s) were of the opinion that such situation should not occur as theoretically the air temperature in the pipeline would vary from 100 to 70^{o}C (approx.) along the pipeline, which is much higher than the dew point temperature corresponding to the local pipeline pressure, (i.e. dew point of 3.2^{o}C towards the end of pipeline, where the pipeline pressure is almost equal to that of atmospheric (as quoted by the supplier). However, NTPC understands that moisture/dew formation (with chances of ash agglomeration and line chocking) is a practical problem and cannot be ignored. NTPC decided to investigate into the matter jointly with TIET.

3.2 CONVEYING CONDITION

The conveying conditions for a particular case of pneumatic pressure conveying of fly ash are as follows:

- Ash flow rate per stream: 92.8 t/h
- Air flow rate: 6060 m^3/hr (FAD)
- There is no air drying plant
- Total pipeline length: 1103 m (250/300 NB)
- Pressure below blow tank: 2.4 bar
- Summer: dry bulb temperature: 43.5^{o}C; wet bulb temperature: 25.5^{o}C
- Monsoon: dry bulb temperature: 38^{o}C; wet bulb temperature: 27^{o}C
- Winter: dry bulb temperature: 15^{o}C; wet bulb temperature: 10^{o}C
- Air-only line pipe-length of 480 m is insulated

It is apparent that the claim of the supplier that the air temperature would only vary from 100 to 70^{o}C (approx.) is based on the following assumptions:

- The flow through the entire pipeline is “air-only” (i.e. for the estimation of convective heat transfer coefficient on the inner side of the pipe surface, the formed boundary layer corresponds to air only with a low value of heat transfer coefficient);
- The outer surface of the pipe is covered with air (generally static), i.e. predominantly natural convection is occurring from the outlet side of pipe wall with air as the outer medium.

The above assumptions result in rather low values of heat transfer coefficients on the inner and outer boundary wall to be considered for the purpose of calculation; whereas in the practical/under ash flow situation, highly turbulent ash/dune flow occurs on the inner side of the pipe and the outer surface is subjected to impingement cooling by rain-water (under heavy rainfall situation). Both these situations (on the inner and outer wall of the pipe) would lead to the rapture of the hydrodynamic/thermal boundary layer (with a high rate of heat transfer due to the impingement flow of powder dunes and water/rainfall).

3.3 MODELLING TEMPERATURE DISTRIBUTION

The following figure (Figure 3.1) shows the mass and energy interaction across a pipe section. The heat generated due to the friction of powder dune on the inner wall of the pipe and kinetic energy of the solid-air mixture is trivial (and hence neglected) compared to the heat transfer across the pipe-wall.

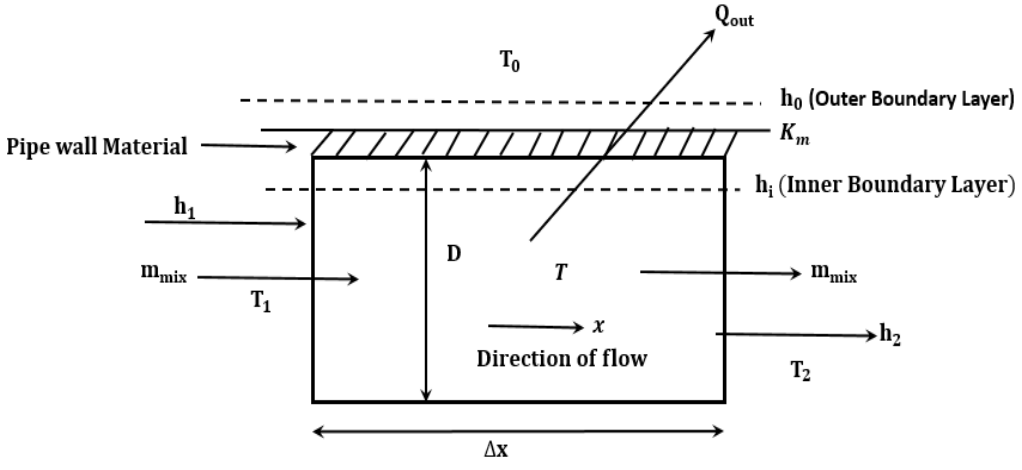

Figure 3.1: Control flow of air-ash flow through pipe

Energy balance equation across the control volume:

$$m_{mix}h_1 = m_{mix}h_2 + UA(T - T_0) \tag{3.1}$$

$$or, \quad m_{mix}(h_1 - h_2) = UA\,(T - T_0) \tag{3.2}$$

$$or, \quad m_{mix}\,C_{p\,mix}\,\Delta T = UA\,(T - T_0) \tag{3.3}$$

$$or, \ \frac{\Delta T}{T - T_0} = UA/\,(m_{mix} \times C_{p\,mix}) = \frac{dT}{T - T_0} \tag{3.4}$$

$$Let, \quad T - T_0 = \theta = excess\ temperature \tag{3.5}$$

$$or, \quad dT = d\theta \tag{3.6}$$

$$or, \frac{d\theta}{\theta} = \frac{UA}{(m_{mix} \times C_{p\,mix})} = \frac{U\,\pi D\Delta x}{(m_{mix} \times C_{P\,mix})} = \frac{U\pi D d_x}{m_{mix} \times C_{p\,mix}} \tag{3.7}$$

$$or, \int_{\theta_1}^{\theta_0} \frac{d\theta}{\theta} = \frac{-U\pi D}{m_{mix}\,C_{P\,mix}} \int_0^x dx \ \left[As \frac{d\theta}{dx}\ is\ negative\right] \tag{3.8}$$

$$or, \frac{T - T_0}{T_1 - T_0} = e^{-\left[\frac{U\pi D}{m_{mix}\,C_{p\,mix}}\right] \times x} \tag{3.9}$$

$$or, T\ (temperature\ at\ any\ length\ x) = T_0 + (T_1 - T_0)\,e^{-\frac{U\pi Dx}{m_{mix}\,C_{p\,mix}}} \tag{3.10}$$

Now,

$$\text{UA} = \frac{1}{{}^{1}/_{h_i A_i} + {}^{1}/_{h_0 A_0} + {}^{1}/_{2\pi K_m L} \ln {}^{r_i}/_{r_0}} \tag{3.11}$$

Where,

r_i=Inner pipe radius

r_0=Outer pipe radius

K_m is much high (metallic conduction); also h_i is high - approx. 100 w/m^2 k due to fluidized turbulent condition (Abdelmotalib *et al.*, 2015; Hofer, Schöny and Pröll, 2018) . Hence,

$$\frac{1}{h_i A_i} \cong 0\ , \frac{1}{2\pi K_m L} \ln {}^{r_i}/_{r_0} \cong 0, and\ A_i \cong A_0 \cong A \tag{3.12}$$

$$U \cong h_0 \tag{3.13}$$

Therefore, the governing equation becomes:

$$T_x = T_0 + (T_1 - T_0)e^{-\frac{h_0 \pi D x}{m_{mix} \times C_{p\,mix}}} \tag{3.14}$$

$$or, \qquad T_x = T_0 + (T_1 - T_0)e^{-\frac{Nuk_0 x}{m_{mix}\, C_{p\,mix}}} \tag{3.15}$$

Outer cooling of the pipe is due to impingement water cooling during the rainy condition. For such a condition,

Nu = Nusselt number for impingement cooling (varies from 100 to 500) (Janssen, Blocken and Carmeliet, 2007; Choo and Kim, 2010; Kuraan, Moldovan and Choo, 2017)

'Nu' taken here as: 100

'k_0 taken here as: 0.60 W/mK (corresponding to water/rainwater)

It is given that the temperature of the air at the outlet of transport air compressor is 150°C and the air only line is insulated. Hence, transport air temperature at the blow tank location (feed point) is considered as 150°C.

Using Nu = 100, k_0= 0.60 w/mk, x = 1103 m (total pipeline length); T_1 = 150°C, T_0 = 10°C for winter and 27°C for monsoon, $m_{mix} = 27.8\ kg/s$ (the ambient temperatures have been considered equal to the WBT for the worst condition, i.e. when relative humidity is 100% corresponding to raining or highly humid condition – see the text below illustrating this point); $c_{p\,mix} = 740\ J/kgK$ and using equation (3.15), T_x (the temperature at different locations of the pipe) have been calculated with an increase in 'x' for winter and monsoon seasons (shown in Figure 3.2 and Figure 3.3, respectively).

The variation of gas temperature for both winter and monsoon were concave upwards. The temperature drop in winter is more than that for monsoon. The exit temperature for winter is lower than that of monsoon. This is because of the low ambient temperature during winter. The reduced temperature facilitates the heat transfer thus reducing the temperature of the gas in the pipeline.

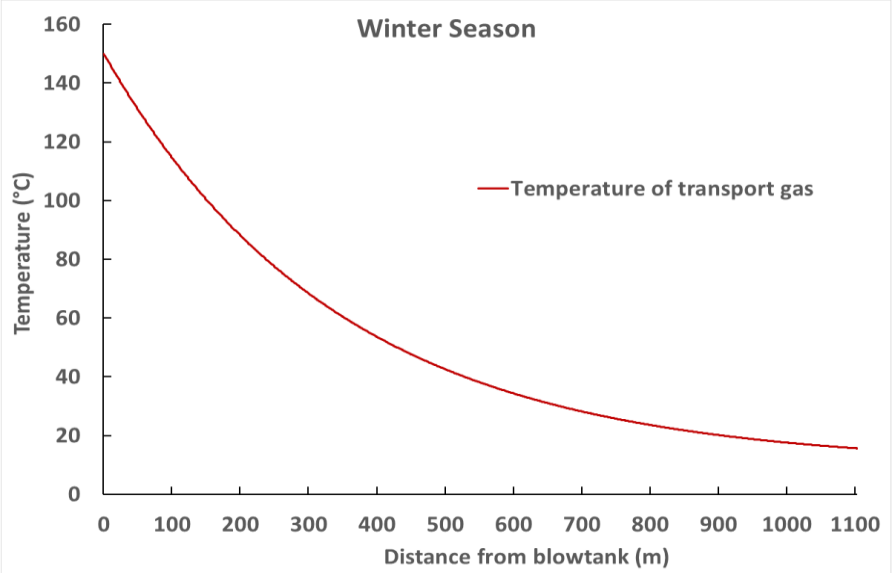

Figure 3.2: Variation of gas temperature along with distance from blow tank (winter season)

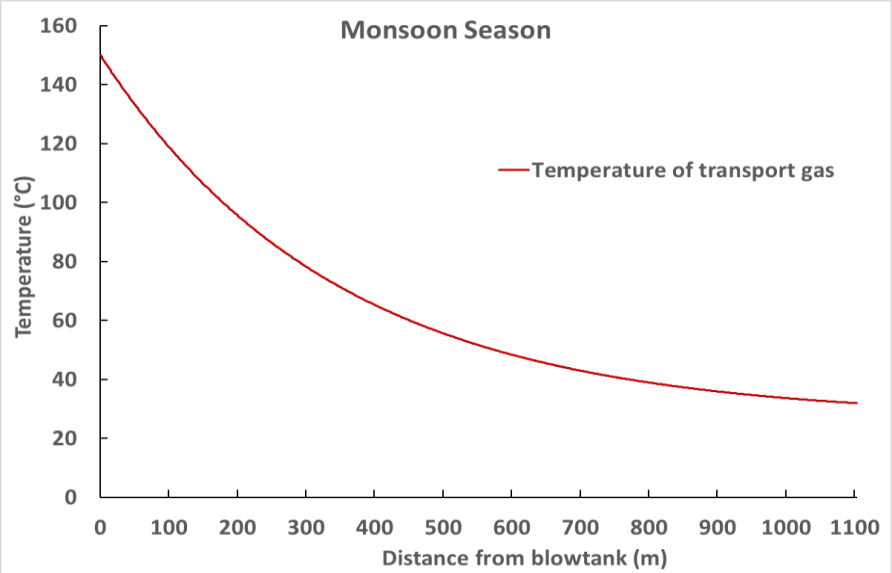

Figure 3.3: Variation of gas temperature along with distance from blow tank (monsoon season)

3.4 PRESSURE DEW POINT AND FLOW TRANSIENTS

Dew point temperature depends on both dry bulb temperature and relative humidity. The criteria for dew formation at any given temperature is based on 100% relative humidity and this would correspond to a condition when DBT drops down equal to WBT. Based on the atmospheric condition that in winter i.e. dry bulb temperature of 15^{o}C and wet bulb temperature of 10^{o}C, the value of relative humidity is found to be 53% from the psychometric chart. Similarly, for the monsoon season, from i.e. dry bulb temperature of 38^{o}C and wet bulb

temperature of 27°C, the corresponding value of relative humidity is found to be 43%. The atmospheric condition at the silo end for winter and monsoon seasons are 5.5°C and 23°C, respectively. The claim of the supplier that dew point temperature is to be considered as 3.2°C at silo end is not clear, but it appears that the supplier might have designed the system with the worst case of 53% relative humidity. However, 53% relative humidity is practically not the worst condition in the Indian context and the system should have been designed for 100% relative humidity (i.e. for very humid or raining condition). For considering the worst case (i.e. 100% relative humidity), DBT and WBT would be identical. It appears that the provided data of dry bulb and wet bulb temperatures corresponding to winter and monsoon (i.e. 15 °C and 10°C and 38 and 27°C, respectively) are either the day time temperatures or the mean temperatures for a whole day further averaged over a season.

[NOTE: From experience, dew formation occurs in North India towards the end of the month of November when the minimum night-time temperature is about 10 to 15°C (which are higher than 3.2°C or even 5.5°C).]

Considering linear pressure drop profile of transport air from 2.4 bar at blow tank location to atmospheric pressure at silo (over 1103 m), pressure dew point temperatures at different points along the pipeline (with an increase in 'x' from 0 to 1103) have been calculated corresponding to the ambient conditions of 10°C and 27°C (WBT) for winter and monsoon months, respectively corresponding to the worst case (100% relative humidity). The increase in dew point temperatures due to the prevailing pipeline pressure (due to compressed gas flows) w.r.t the atmospheric dew point temperatures have been calculated using the following set of equations.

$$\phi = \frac{p_v}{p_{vs}} \tag{3.16}$$

$$\ln(p_{sat}) = \frac{C_1}{T} + C_2 + C_3 T + C_4 T^2 + C_5 T^3 + C_6 \ln(T) \quad \text{(Ramgopal, 2009)} \tag{3.17}$$

Where,

$C_1 = -5.80022006 \times 10^3$; $C_2 = -5.516256$; $C_3 = -4.8640239 \times 10^{-2}$;

$C_4 = 4.1764768 \times 10^{-5}$; $C_5 = -1.4452093 \times 10^{-8}$; $C_6 = 6.5459673$

$$W = 0.622 \frac{p_v}{p_t - p_v} \tag{3.18}$$

$$DPT = \frac{4030(DBT + 235)}{4030 - (DBT + 235)ln\phi} - 235 \tag{3.19}$$

It can be seen that increase in gas temperature would tend to lower the relative humidity, while elevated pressure would act to counteract the temperature effect cause an increase relative humidity (and thus an increase in dew point temperature). Moreover, the pressure fluctuations due to solid-air flow turbulence increase towards the end of the pipeline (compared to the starting of pipe) (Mittal and Mallick, 2016). Figure 3.4 shows a typical pressure versus time plot for the pneumatic conveying of powders (Mittal and Mallick, 2016).

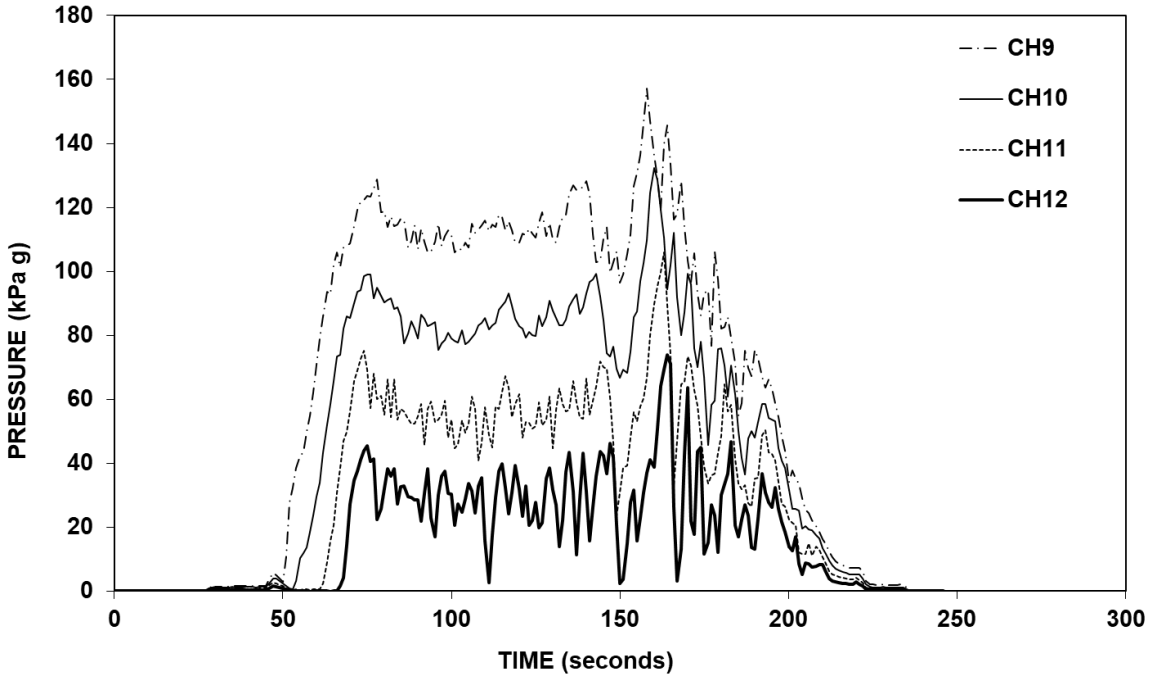

Figure 3.4: Typical pressure fluctuation curves for pneumatic conveying of powders (Mittal and Mallick, 2016)

In Figure 3.4 CH9, CH10, Ch11 & CH12 represent the pressure variations at various location in the conveying pipeline. From (Mittal and Mallick, 2016), the magnitude of fluctuation could be as high as 80% of the mean line pressure due to the highly turbulent and transient nature of the solids-gas flows (with % of pressure fluctuation increasing towards the end of pipeline). Figure 3.5 and Figure 3.6 show the pressure dew point lines for winter and monsoon seasons, respectively superimposed in Figure 3.2 and Figure 3.3 for the following conditions:

1. Neglecting pressure transients/fluctuations
2. Considering 30% pressure transients/fluctuations
3. Considering 60% pressure transients/fluctuations

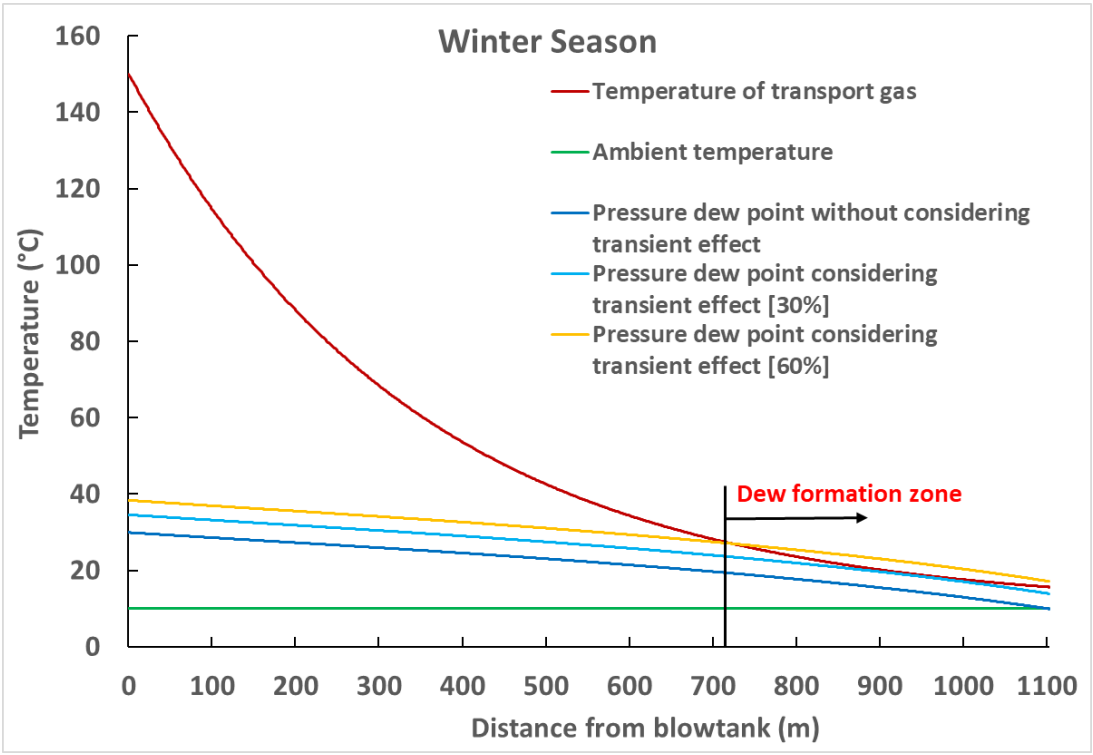

Figure 3.5: Temperature of transport air and pressure dew point lines (with and without transient effects) with an increase in distance from blow tank (winter season)

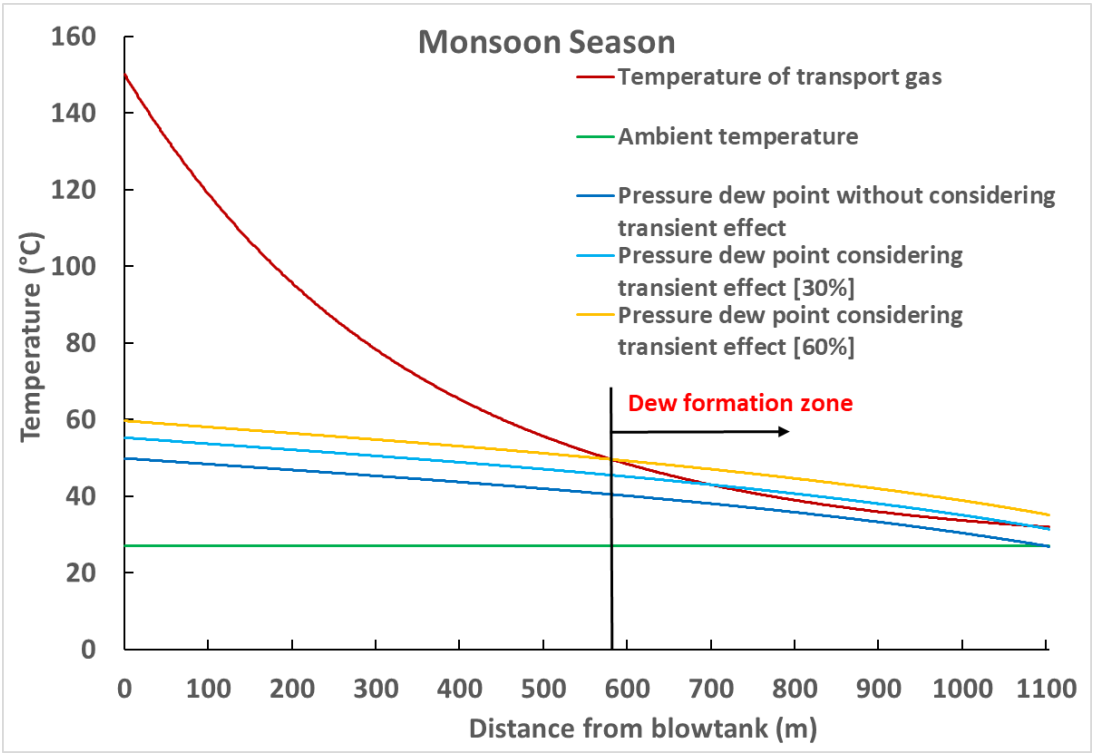

Figure 3.6: Temperature of transport air and pressure dew point lines (with and without transient effects) with an increase in distance from blow tank (monsoon season)

The results (Figure 3.5 and Figure 3.6) show that the temperature of transport air drops below or to that of the pressure dew points for both winter and monsoon seasons considering both 30 and 60% pressure fluctuation/transient effects. This indicates that dew formation is likely to occur in both winter and monsoon seasons after about 720 m and 580 m of travel distance/pipe lengths, respectively in case, no air drier is used in the compressed air system.

3.5 CONCLUSION AND RECOMMENDATION

Due to the highly turbulent ash-air mixture at the inner side of the pipe and impingement cooling by water on the outer side (resulting in large heat transfer coefficient due to the rapture of the boundary layer), there will be rapid heat transfer /rapid cooling of the ash-air mixture. The given conditions of Dry and Wet Bulb Temperatures (i.e 15^{o}C and 10^{o}C for winter and 38^{o}C and 27^{o}C for the monsoon season) correspond to only 53 and 43% relative humidity. Such moderate values of relative humidity conditions are not adequate to represent the "worst case" scenario. It is recommended that the design practice to determine the requirement of the air drier should be based on 100% relative humidity (which corresponds to dry and wet bulb temperatures being identical), as practically such situation could happen due to extremely humid or rainy conditions. Moreover due to the pressure fluctuation of air-ash mixture, the local peak pressure could go to higher than the mean pressure by a margin of as high as 60% (sometimes even higher fluctuations have been reported, Mittal and Mallick, 2016) with a corresponding rise in dew point temperature/pressure dew point causing dew formation (under high humid and rainy condition). Therefore, it is recommended that to cater for the worst-case scenario (having 100% relative humidity and considering pressure transients), the compressor should be supplied with an air-drying plant.

CHAPTER 4 : CALIBRATION OF FINE POWDER FOR DISCRETE ELEMENT METHOD

4.1 INTRODUCTION

Bulk solids handling of fine powders finds a place in various industries. These products range from pulverized coke and iron ore used in a blast furnace in steelmaking industries, fly ash produced in thermal power plants and to essential products that find significant importance in our daily life such as powdered spices.

Appropriate designing of bulk solids handling equipment is in itself a tedious task, but when handling fine powders, the design of the same equipment becomes even more demanding. The reason behind it is that when particles are coarse in nature, they tend to flow easily but as the size of the particles in the powder reduces, the flowability reduces. This is due to the fact that fine powders are more cohesive in nature. The reason for such behavior is the increase in the particle-particle interactions in the fine powder. For the same amount of coarse powder, the number of particles is higher in fine powders, due to this the interparticle forces which were negligible in coarse grain powders become predominant in case of fine powder. These forces include van der Waals forces, electrostatic force, the formation of liquid bridge, etc.

Simulation of these powders can be performed using software working on Discrete Element Method such as EDEM, LIGGGHTS, YADE, Newton, etc. But the performance of the simulation is as good as the modelling of the material required to be simulated. In recent years various calibration schemes have been developed for calibration of DEM parameters. But the material calibrated has always been powders with large particle size (i.e. greater than 0.5 mm). In this work, effort have been made to calibrate DEM parameters for fine powders.

4.2 LITERATURE REVIEW

4.2.1 CHARACTERIZATION OF BULK SOLIDS

Particle Size

Particle size is a representation of the particle size in a quantitative term. It is used for comparison of dimensions of a solid particle.

Following are the various type of particle size:

i. Volume-based particle size(D_v): It is equal to the diameter of the sphere that has the same volume as a given particle.

$$D_v = 2\sqrt[3]{\frac{3V}{4\pi}} \tag{4.1}$$

ii. Area-based particle size(D_s): It is equal to the diameter of the sphere that has the same surface area as a given particle.

$$D_s = \sqrt[2]{\frac{4A}{\pi}} \tag{4.2}$$

iii. Hydrodynamic/aerodynamic particle size: It is equal to the diameter of the sphere that has the same drag coefficient as a given particle

iv. D_{50}: It is the diameter of the particle that 50% of a sample's mass is smaller than and 50% of a sample is larger than.

v. Arithmetic diameter($\overline{D}10$/D[1,0]): It is the average diameter of a particle in a sample

vi. Volume/surface mean or $\overline{D}32$/D[3,2]: In fluid dynamics, Sauter mean diameter (SMD, d_{32} or $D[3, 2]$) is an average of particle size. It is defined as the diameter of a sphere that has the same volume/surface area ratio as a particle of interest.

vii. Mean diameter over volume or $\overline{D}43$/D[1,0]: It is the centre of mass for frequency distribution and is also called the DeBroukere mean.

viii. Ferret diameter: Minimum and maximum Ferret diameters are the diameters that are minimum and maximum distance measuring the extent of a particle boundary in a silhouette.

Particle Size Distribution

Particle size distribution (PSD) of a powder is a mathematical function that represents the frequency of particle size available in the sample. Cumulative PSD can be of two types undersize or oversize. In undersize cumulative PSD, the frequency of the particle having a size less than a particular value are reported and vice-versa. Figure 4.1 shows the undersize PSD of a powder sample.

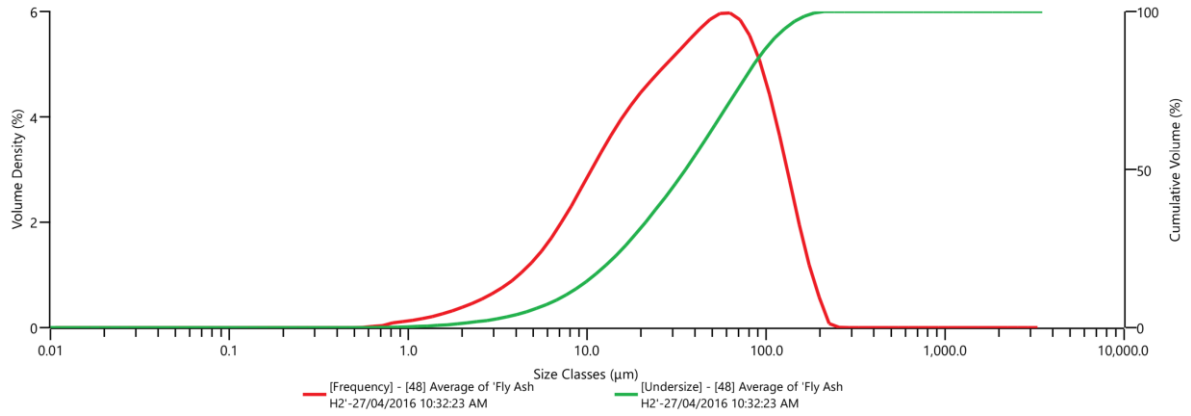

Figure 4.1 : Particle Size Distribution

Following are the measurement methods available to obtain particle size distribution:

i. Sieving Analysis
   Standard: ASTM C136 / C136M – 14
ii. Dynamic Image Analysis
   Standard: ISO 13322-1, ISO 13322-2
iii. Laser Diffraction
   Standard: ISO 13320:2009

Particle Shape

Particle shape is the external appearance of a particle. Various different aspects of particle shape are of interest and a range of parameters have been devised to describe particle shape for different applications.

Particle shape can be described qualitatively using the following descriptors:

i. Width/length ratio: It is the ratio of the shortest to the largest diameter or minimum Ferret diameter to maximum Ferret diameter. Sometimes it is also made necessary that the shorter measurement is made in a direction perpendicular to the largest distance.

$$Width/length\ ratio = \frac{shortest\ diam.}{longest\ diam.} = \frac{\perp\ to\ longest\ diam.}{longest\ diam.} = \frac{F_{min}}{F_{max}} \qquad (4.3)$$

ii. Convexity: It is a measure of the irregularity of the particle. It is represented by the root of the ratio of the actual area to the area formed by joining the outer most points of the particle's convex area. Mathematically it is given by the equation (4.4).

$$Convexivity = \sqrt{\frac{A_{real}}{A_{convex}}} \tag{4.4}$$

iii. Symmetry: It is representative of the symmetry of the particle.

$$Symmetry = \frac{1}{2}\left(1 + min\left(\frac{r_1}{r_2}\right)\right) \tag{4.5}$$

iv. Circularity: The degree to which the ratio of the area to the circumference approaches the same for circle. If can be defined in the following ways:

- Cox's Circularity or classic shape factor (1927)

$$\text{Cox's Circularity or classic shape factor (1927)} = \frac{4\pi A}{p^2} \tag{4.6}$$

- True Circularity or degree of circularity *(Wadell,1933)*

$$\text{True Circularity} = \frac{\text{circumference of equivalent circle}}{\text{circumference of the figure}} \tag{4.7}$$

- Lappung's quotient (Beckmann, 1962)

$$\text{Lappung's quotient} = \frac{1}{\text{True circularity}} \tag{4.8}$$

- Irregularity (Umbaugh, 2005)

$$\text{Irregularity} = \frac{1}{\text{Cox's circularity}} \tag{4.9}$$

v. Roundness: It is the quantitative measure of the roundness of the particle edges. It is given by:

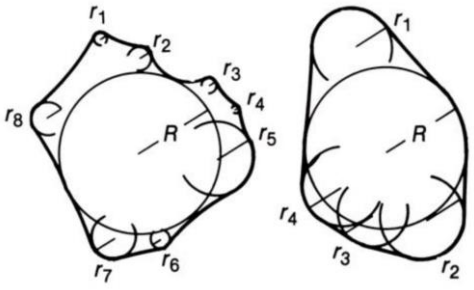

Figure 4.2 : Roundness

$$Roundness = \frac{\sum_{i=0}^{n}\left(\frac{r_i}{R}\right)}{n} \tag{4.10}$$

Where,

r_i is the radius of curvature of particle corners

R is the radius of the largest inscribed sphere

n is the number of particle corners measured

vi. Sphericity: It is the measure of how closely a particle resembles the shape of a sphere. It is given by the following:

- Cox's True Sphericity(1927): The degree to which the ratio of its volume to its surface approaches the same ratio for a sphere

$$\text{True sphericity} = \frac{\text{surface area of equivalent sphere}}{\text{surface area of the body}} \tag{4.11}$$

- Tickell's Sphericity(1931)

$$\text{Tickell's sphericity} = \frac{\text{area of figure}}{\text{area of circumcircle}} = \frac{\text{volume of body}}{\text{volume of circumsphere}} \tag{4.12}$$

- Wadell's sphericity(1933)

$$\text{Wadell's sphericity} = \frac{\text{dia of equivalent circle}}{\text{dia of circumcircle}} = \frac{\text{dia of equivalent sphere}}{\text{dia of circumsphere}} \tag{4.13}$$

The difference between roundness and sphericity can be understood by the quantitative roundness scale given by powers(Powers, 1953).

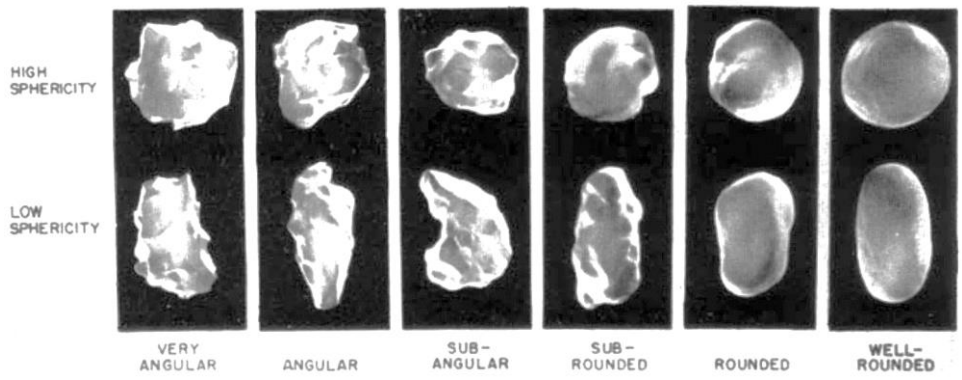

Figure 4.3 : Quantitative roundness scale(Powers, 1953)

Particle Density

Particle density or True density of a particulate solid or powder, is the density of the particles that make up the powder. Here the mass of the particles can easily be measured by precision weight balance but measurement of the volume turns out to be tricky. This is because particles

have various type of cavities and different standards measure them differently i.e. excluding or including some of them. The various types of voids are shown in Figure 4.4 and the volumes considered by various standards are tabulated in Table 4.1.

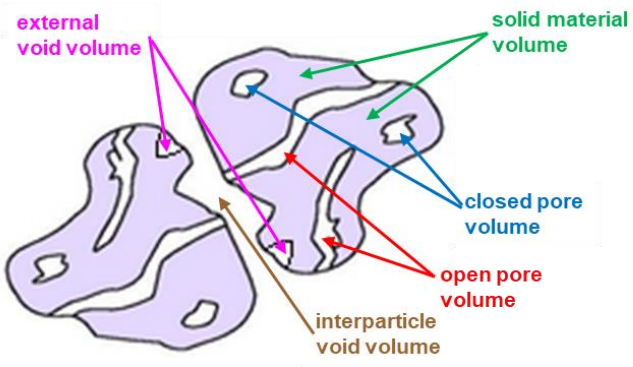

Figure 4.4 : Different type of voids in particle

Density definitions	Volumes included in the definition				
	Solid material volume	**Open pore volume**	**Closed pore volume**	**Inter-particle void volume**	**External void volume**
Absolute powder density (BSI)	X				
Theoretical density (ASTM)	X				
True density (BSI)	X				
Apparent particle density (BSI)	X		X		
Skeletal density (ASTM D3766)	X		X		
Effective particle density (BSI)	X	X	X		
Envelope density (BSI)	X	X	X		X
Envelope density (ASTM D3766)	X	X	X	X	X

Table 4.1 : Particle density definitions

It is measured by water displacement method by:

$$\rho_p = \frac{m_f - m_i}{V_f - V_i} \text{(ASTM C 693)} \tag{4.14}$$

Where,

m_f :Mass of measuring cylinder filled with water+powder

m_i :Mass of measuring cylinder filled with water

V_f :Volume of measuring cylinder filled with water+powder

V_i :Volume of measuring cylinder filled with water

Measurement Methods for determination of particle density:

i. Water Pycnometer
   Standard: ASTM D854 – 14, DIN EN 725-7
ii. Gas Pycnometer
   Standard: ASTM D5550-06
iii. Mercury Porosimetry
   Standard: ISO 1183-1:2004, ASTM D854

Bulk Density

Bulk density of the powder is the density of bulk solids including the voids between the particles. Bulk density is not an intrinsic property of a material; it can change depending on how the material is handled (storage and treatment). For example, a powder poured into a cylinder will have a particular bulk density. If the cylinder is disturbed, the powder particles will move and usually settle closer together, resulting in a higher bulk density.

Therefore, two bulk densities are usually measured:

i. **Loose Poured Bulk Density:** Loose poured bulk density is the density of bulk solid which is measured when the powder is aerated and is freely settled in the measuring container. It is used to calculate the maximum volume that is required to contain a bulk solid.

   Standard: ISO 697

ii. **Tapped Bulk Density:** Tapped bulk density is an increased bulk density attained after mechanically tapping a container containing the powder sample. The minimum packed volume thus achieved depends on a number of factors including particle size distribution, true density, particle shape and cohesiveness due to surface forces including moisture. Therefore, the tap density of a material can be used to predict both its flow properties and its compressibility.

   Standard: ASTM D7481 – 18

Compacted Bulk Density

Compacted bulk density is the density of bulk solids measured with the application of load/consolidation stress. Due to the self-weight of the powder, its bulk density, that controls the stresses acting on the powder while flowing or at rest condition in processing lines/silos,

etc. Compacted bulk density measurement delivers repeatable results at different consolidated stress without direct operator involvement.

Measurement Method:

Powder Flow Tester

Standard: ASTM D6128

Equipment: AMETEK Brookfield/BROOKFIELD Powder Flow Tester

Angle of Repose

The angle of repose is defined as the natural slope of the surface of a bulk solid observed during a specified test, and this can be regarded as a property of the material. It reflects the flowability of bulk solids in the unconsolidated state. It can be both static or dynamic. In the static angle of repose, the angle formed by a heap of the particle is measured. Whereas in the dynamic angle of repose, the angle measured in a rotating drum rotating at particular rpm.

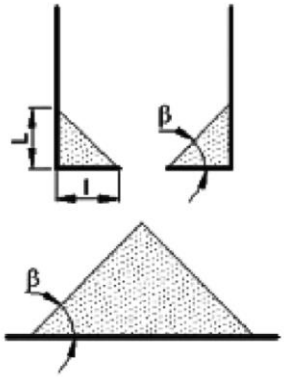

Figure 4.5 : Static angle of repose(Fraczek, Złobecki and Zemanek, 2007)

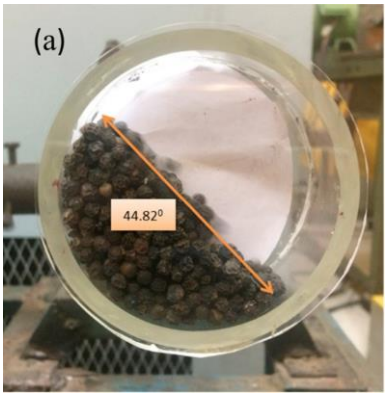

Figure 4.6 : Dynamic angle of repose(Kanakabandi and Goswami, 2019)

4.2.2 DEM FUNDAMENTALS

The foundation of the discrete element method or DEM were laid by Peter A. Cundall in the year 1971. It was originally developed for solving the problems related to rock mechanics. Over the passage of time, researchers started using DEM as a simulation field in various other fields also. Nowadays DEM is applied to fields such as agriculture, food processing, pharmaceutical, and mining, etc.

Unlike computational fluid dynamics (CFD) in which the fluid is modelled as a continuum, DEM models each and every particle individually. This modelling employs pure Newtonian mechanics. Broadly DEM modelling techniques can be classified into two approach:

i. Hard sphere approach
ii. Soft sphere approach

Hard Sphere Approach

In hard sphere approach, the particle is assumed to be rigid. This means deformation of the particle during collision is not taken into consideration. Although, some amount of deformation would always be present. But, this type of approach proves instrumental in certain applications where collisions are not frequent. This allows the use of larger time step, thus saving on the computational cost. This approach has been successfully applied to granular particles in rotating drum(Campbell, 1985; Gui and Fan, 2009; Richardson *et al.*, 2011), formation of bubble and slug in fluidized bed(Hoomans *et al.*, 1996), segregation of particles in fluidized bed(Hoomans, Kuipers and Van Swaaij, 2000; Dahl and Hrenya, 2004, 2005) and for studying high pressure fluidization characteristics(Li and Kuipers, 2002, 2005).

Equation of Motion

The motion of the particle is governed by Newton's second law of motion. The generalized version of these equations is given below.

$$m_i \frac{d\vec{v}_i}{dt} = m_i \frac{d^2\vec{x}_i}{dt^2} = m_i\vec{g} + \vec{f}_i^{f-p} + \vec{f}_i^{p-p} + \vec{f}_i^{ext} \tag{4.15}$$

This equation governs the linear velocity and the position of the particle. The left-hand side of the equation denotes the rate of change of linear momentum and the right-hand side is the summation of all possible forces acting on the particle. These include gravitational force, the force due to particle-fluid interaction, the force due to the influence of other particles (i.e.

collision or interparticle forces) and any external forces that are acting on the particles. This can be the forces caused by magnetic fields, electrostatic fields or the force acting on the particles by the surface of the containers in which these are stored.

$$I_i \frac{d\vec{\omega}_i}{dt} = I_i \frac{d^2\vec{\varphi}_i}{dt^2} = \vec{M}_{ij}^{t} + \vec{M}_{ij}^{r} \tag{4.16}$$

This equation governs the angular velocity and displacement of the particle. The left-hand side represents the rate of change of angular momentum while the right-hand-side of the equation is the sum of all the moments acting on the particle. These moments comprise of two parts. First is the moment caused by the tangential contact of the particle during a collision while the other is to take into account the rolling friction that acts on the particle and subsequently tends to rotate it.

Collision Modelling

Consider two particles with radii R_i and R_j, position vectors $\vec{x}_i$ and $\vec{x}_j$, and masses m_i and m_j. They are moving with translational velocities $\vec{v}_i^0$ and $\vec{v}_j^0$, and rotating with rotational velocities $\vec{\omega}_i^0$ and $\vec{\omega}_j^0$.

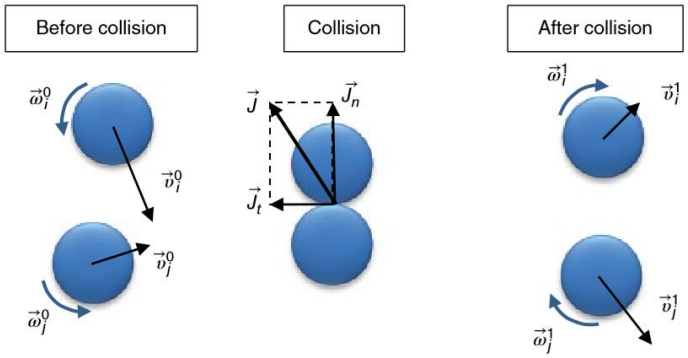

Figure 4.7 : Collison Modelling(Reza Norouzi *et al.*, 2016)

The translational and angular velocity if these particles after a collision are given by:

$$m_i\vec{v}_i^1 = m_i\vec{v}_j^0 + \vec{J} \tag{4.17}$$

$$m_j\vec{v}_j^1 = m_j\vec{v}_j^0 - \vec{J} \tag{4.18}$$

$$I_i\vec{\omega}_i^1 = I_i\vec{\omega}_i^0 + R_i\vec{n}_{ij} \times \vec{J} \tag{4.19}$$

$$I_j\vec{\omega}_j^1 = I_j\vec{\omega}_j^0 + R_j\vec{n}_{ij} \times \vec{J} \tag{4.20}$$

$$\vec{J} = J_n \vec{n}_{ij} + J_t \vec{t}_{ij} \tag{4.21}$$

Here $\vec{n}_{ij}$ represents the unit vector pointing from particle *i* to particle *j*, $\vec{t}_{ij}$ is the tangential vector perpendicular to the plane of the collision, $\vec{J}$ is the impulse force and *I* is the moment of inertia of the particle.

The relative velocities between the particles at the point of contact is given by:

$$\vec{v}_{ij} = \vec{v}_i - \vec{v}_j + (R_i \vec{\omega}_i + R_j \vec{\omega}_j) \times \vec{n}_{ij} \tag{4.22}$$

$$\vec{v}_{ij}^{\,n} = (\vec{n}_{ij} \cdot \vec{n}_{ij}\,) \times \vec{n}_{ij} \tag{4.23}$$

$$\vec{v}_{ij}^{\,t} = \vec{v}_{ij} - \vec{v}_{ij}^{\,n} \times (\vec{n}_{ij} \times \vec{v}_{ij}) \tag{4.24}$$

Coefficient of restitution is related to the relative velocity of a particle before and after the collision. It is the ratio of relative velocity after a collision to the relative velocity before the collision. The coefficient of restitution acts in both normal and tangential direction, given by the following equations:

$$\vec{n}_{ij} \cdot \vec{v}_{ij}^{\,1} = -e_n \left(\vec{n}_{ij} \cdot \vec{v}_{ij}^{\,0}\right), \quad 0 \le e_n \le 1 \tag{4.25}$$

$$\vec{t}_{ij} \cdot \vec{v}_{ij}^{\,1} = -e_t \left(\vec{t}_{ij} \cdot \vec{v}_{ij}^{\,0}\right), \quad -1 \le e_t \le 1 \tag{4.26}$$

Interparticle Forces

Interparticle forces are non-contact forces. These can be either attractive or repulsive in nature. These forces are inversely proportional to the square of the distance between the particles, similar to gravitational force.

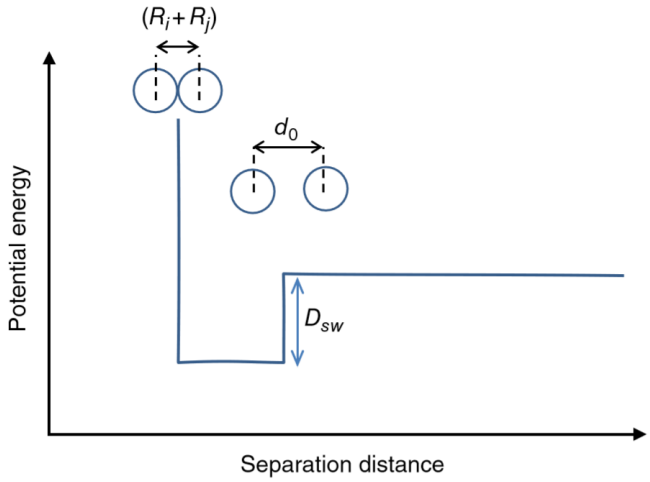

Figure 4.8 : Square-well method for interarticular forces(Reza Norouzi *et al.*, 2016)

$$F_{Inter-Particle} \propto \frac{1}{d^2} \tag{4.27}$$

But while modelling interparticle forces it is not possible to calculate these forces for all the particles. Thus (Weber, Hoffman and Hrenya, 2004) introduced the square-well method for modelling interparticle forces in granular flows. Here interparticle forces are modelled in such a way that the interparticle forces come into effect only when the distance between the two particles become equal to or less than a particular threshold distance d_0. Thus, the interparticle force is modelled as a step function.

Soft Sphere Approach

In the soft sphere, the instantaneous collisions of the hard sphere approach are replaced by multiple contacts in progression. This is because the bodies are assumed to be deformable. Unlike hard sphere approach where the interaction between particles is considered just at a single point, in a soft sphere approach, interaction takes place over an overlap area, although this area is very small. The overlaps changes throughout the collision, reaches a maximum which depends on the physical properties of the material. The force acting on the particles before and after a collision, linear and angular velocities are governed by the Newtonian laws of motion.

Force-Displacement Law

When two particles come into contact force displacement laws dictate the property of the collision taking place. Both normal and tangential overlap takes place during the collision. It is here that multiple collisions take place. The force tending to separate the two bodies depends on the overlap. The normal overlap of the two particles is given by:

$$\delta_n = R_i + R_j - \left|\vec{x}_j - \vec{x}_i\right| \tag{4.28}$$

If $\delta_n \not\geq 0$ there is no physical contact between the particles. The tangential overlap is calculated from the tangential relative velocity.

$$(v_{rt} = \vec{v}_{ij}\vec{t}_{ij}) \tag{4.29}$$

The collision gives rise to both normal as well as tangential forces. The collision force is given by the sum of both of these forces.

$$\vec{f}_{ij}^{c} = \vec{f}_{ij}^{n} + \vec{f}_{ij}^{t} \tag{4.30}$$

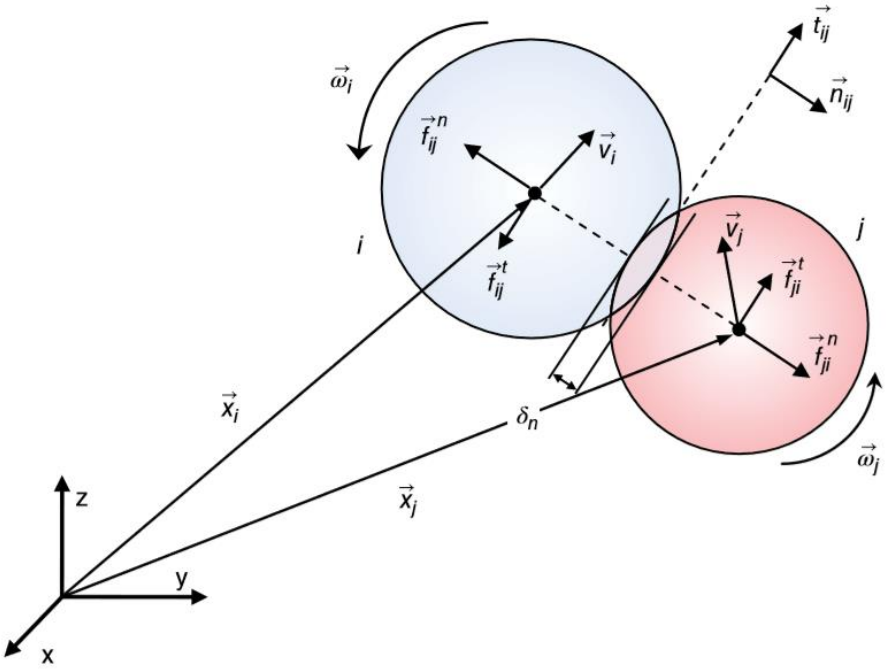

Figure 4.9 : Schematic of two colliding particles and forces acting on them(Reza Norouzi *et al.*, 2016)

Linear Viscoelastic Model

Linear spring-dashpot model is one of the most common force displacement law. This model is widely used due to its ease of implementation. Here the collision force in the normal direction consists of both elastic and viscous force. The elastic force can be calculated using Hook's law which is directly proportional to change in position i.e. overlap. The viscous force acts in the direction opposite to the direction of motion. It is directly proportional to the velocity of the particle.

$$\vec{f}_{ij}^{\,n} = \vec{f}_{el}^{\,n} + \vec{f}_{diss}^{\,t} = -(s_n \delta_n)\vec{n}_{ij} - (\eta_n v_{rn})\vec{n}_{ij} \tag{4.31}$$

$$(v_{rn} = \vec{v}_{ij}\vec{n}_{ij}) \tag{4.32}$$

Where s_n is the spring stiffness in the normal direction, η_n is the normal dampening coefficient and v_{rn} is the relative velocity in the normal direction.

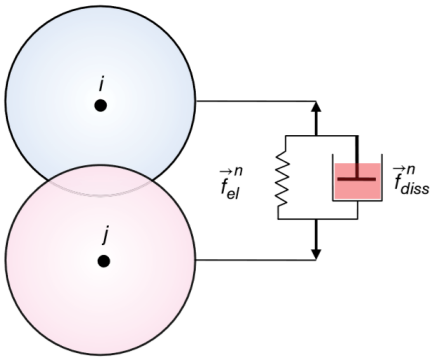

Figure 4.10 : Viscoelastic model(Reza Norouzi *et al.*, 2016)

The equation of motion of the particles in the normal direction is given by the following differential equation:

$$\frac{d^2\delta_n}{dt^2} + 2\psi\frac{d\delta_n}{dt} + \kappa_0^2\delta_n = 0 \tag{4.33}$$

$$\psi = \frac{\eta_n}{2m_{eff}} \tag{4.34}$$

$$\kappa_0^2 = \frac{s_n}{m_{eff}} \tag{4.35}$$

Nonlinear Viscoelastic Model

Although the spring-dashpot model is simple it fails to represent the force-displacement model of two spherical particles accurately. The model for a collision between two spherical elastic particles was first developed by Hertz (Hertz, 1882) but Mindlin and Deresiewicz (Mindlin and D., 1953) also used elastic tangential contacts between particles. Here the contact area is considered circular. The area is discretized into concentric annular areas each of which has the same amount of stress.

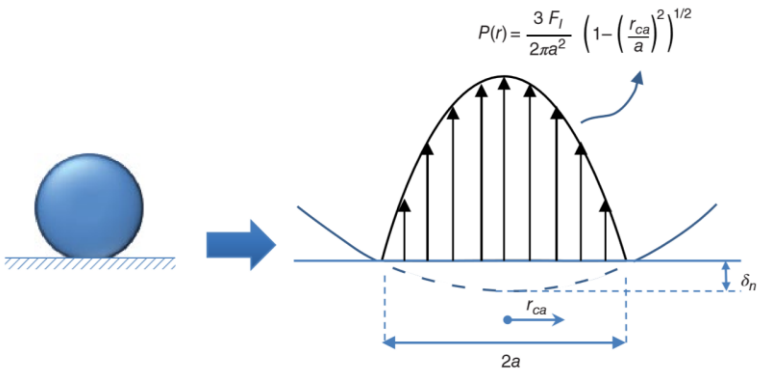

Figure 4.11 : Normal pressure distribution in contact area of an elastic sphere(Reza Norouzi *et al.*, 2016)

Consider a spherical elastic particle in contact with a frictionless wall. The particle deforms, causing a normal force F_l to act in the direction perpendicular to the wall. The sphere comes in to contact with the wall through a circular area. The radius of this area is a. The asymmetric normal pressure is a function of the radial coordinate of the contact area. which is given by:

$$P(r) = P_{max}\left(1 - \left(\frac{r_{ca}}{a}\right)\right)^{\frac{1}{2}} \tag{4.36}$$

In such cases, the contact area is negligible in comparison to the radius of the particle. This the maximum pressure produced at the center of the contact area is

$$P_{max} = \frac{3F_l}{2\pi a^2} = \left(\frac{6F_l E_{eff}^2}{\pi^3 R_{eff}^2}\right)^{\frac{1}{3}} \tag{4.37}$$

The area of contact as a function of the normal force F_l and effective Young's Modulus is calculated as

$$a = \left(\frac{3}{4}\frac{F_l R_{eff}}{E_{eff}}\right)^{\frac{1}{3}} \tag{4.38}$$

Also, the normal deformation is obtained by:

$$\delta_n = \frac{a^2}{R_{eff}} = \left(\frac{9}{16}\frac{F_l^2}{R_{eff}E_{eff}^2}\right)^{\frac{1}{3}} \tag{4.39}$$

4.2.3 FLOW PROPERTIES OF BULK SOLIDS

The flow behavior of a bulk solid depends on various properties like particle size distribution, particle shape, particle density, moisture, temperature, etc. Therefore, it is not easy to estimate the behaviors of a bulk solid theoretically. And even if the behavior is determined theoretically, it is not appropriate to comment without any physical test.

In bulk solids handling a good bulk solid means a material that easily flows out of a silo or a container. Whereas, the materials which don't flow easily are said to have poor flow properties. Flowing means that the bulk solid is deformed plastically due to the load of material acting on it.

Figure 4.12 shows a fine-grained bulk solid placed inside a cylindrical container. A top plate exerts a stress σ_1 onto the surface. This stress is known as consolidation stress. Regardless of the material the volume of the bulk solid decreases on the application of normal stress. A large

change in the volume indicates that the material is compressible in nature. A material which shows relatively more change in the volume for the same amount of applied stress is known to be more compressible.

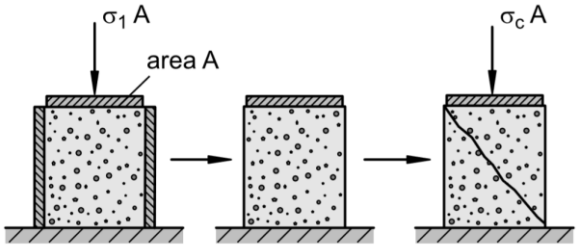

Figure 4.12 : Uniaxial Compression Test(Schulze, 2010)

Moreover, an increase in the strength of the specimen is observed after the application of consolidation stress. Thus, when the specimen is relieved of the consolidation stress and the cylindrical enclosure is taken away, the material retains the shape provided by the cylinder. Now if the material is loaded with vertical compressible stress, the material will fail at a particular stress. This is known as the unconfined yield stress σ_c. Thus, in any case of bulk solid flow if the normal stress acting on the material is higher than the unconfined yield stress, the material with yield and start to flow. Thus, unlike other branches of engineering where it is made sure that the material does not fail in loading condition. In bulk solids, it is favorable that the material continuously fails in compressibility so that that good flowability is achieved.

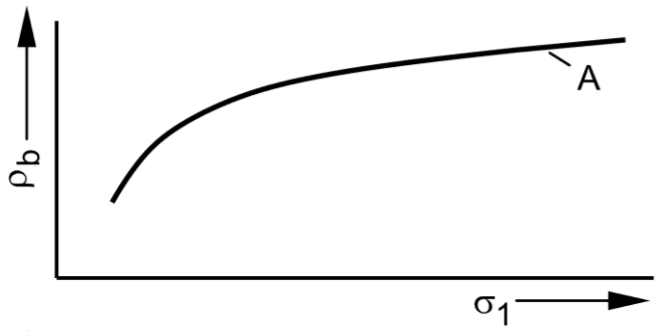

Figure 4.13 : Bulk density as a function of consolidation stress(Schulze, 2010)

Figure 4.13 shows a typical plot of bulk density as a function of consolidation stress. It can be seen that as the consolidation stress increases the bulk density start to increase very rapidly in the beginning but at a later stage, with further increase in consolidation stress, the increase in bulk density observed is comparatively lesser.

When a uniaxial compression test is conducted at various levels of consolidation stress, the unconfined yield stress is obtained corresponding to consolidation stress. The typical relation obtained between these two parameters is shown in Figure 4.14.

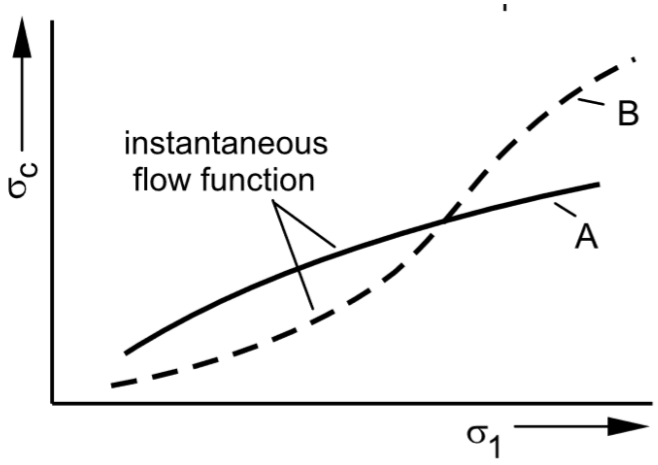

Figure 4.14 : Unconfined yield stress as a function of consolidation stress(Schulze, 2010)

As shown in Figure 4.14 the curve A represents the typical behavior of a bulk solid. This shows that as the consolidation stress increases the unconfined yield stress increases. This curve is known as the flow function or the instantaneous flow function as it shows the strength measured directly after applying consolidation stress. Figure 4.15 shows the difference between instantaneous and time consolidated flow function.

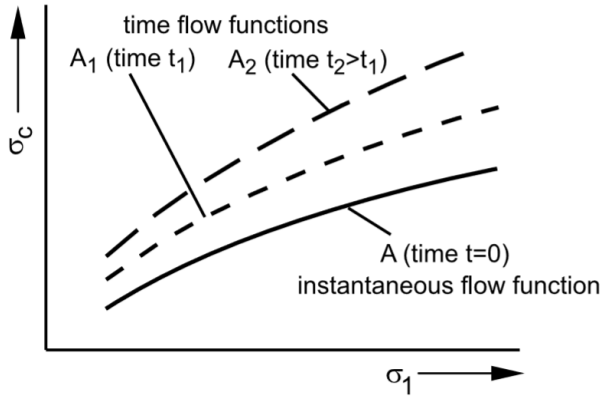

Figure 4.15 : Effect of consolidation time on flow function(Schulze, 2010)

When the unconfined yield stress is measured just after the applying consolidation stress, it is known as instantaneous flow function($t = 0$). But when the unconfined yield is measured progressively after some time the unconfined yield stress increases. This is due to the fact that interparticle forces come into the picture. Due to the presence of these interparticle forces the strength of the unconfined sample increase. Thus, the unconfined yield stress for the same

sample increases. It can also be observed that as time increases the strength of the material keeps on increasing.

Flowability of bulk material is characterized by the relation of its unconfined yield stress as a function of consolidation stress. Thus, numerically flowability is defined as:

$$ff_c = \frac{\sigma_1}{\sigma_c} \tag{4.40}$$

The larger the value of flow function the easier it is for the material to flow. This is because for the same consolidation stress the unconfined yield stress has comparatively less value. Hence, the material will continuously fail and thus attribute to good flow behavior.

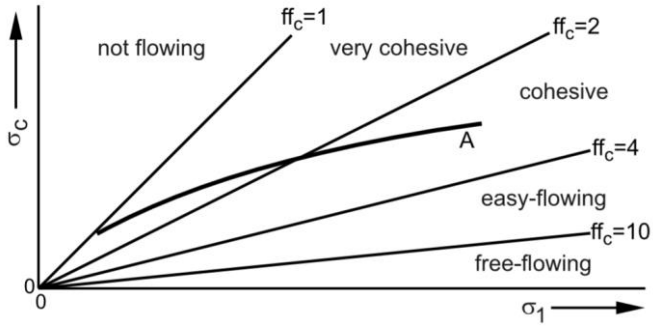

Figure 4.16 : Instantaneous flow function along with constant flow function lines(Schulze, 2010)

As can be seen in Figure 4.16, the flow characteristics can be classified as:

- $ff_c < 1$ not flowing
- $1 < ff_c < 2$ very cohesive
- $2 < ff_c < 4$ cohesive
- $4 < ff_c < 10$ easy flowing
- $10 < ff_c$ free flowing

4.2.4 REVIEW OF PREVIOUS RESEARCH ON DEM CALIBRATION

González-Montellano *et al.*, 2012 used direct mechanical methods to measure the various properties of maize and olives. The properties measured were particle density (ρ_p), Young's modulus (E_p), shear modulus(G_p) particle-wall coefficient of restitution(e_{p-w}), particle-particle coefficient of restitution(e_{p-p})and particle-wall coefficient of friction(μ_{p-w}).

Particle density (ρ_p) was measured using two methods. In the first method, the density of the particle was measured by measuring the mass of particle using a precise balance and then the

estimation of the volume by using the approximate shape of the particle. While in the second method the volume was measured using the pycnometer method. Young's Modulus (E_p) was measured by using Hertz Contact model which required the particles to be compressed with a compression tool and measurement of the particle deformation for the same. Shear Modulus(G_p) was obtained using the relation:

$$G_p = \frac{E_p}{2(1-\nu)} \tag{4.41}$$

Here the approximate value of Poisson's ratio(ν) was used. Particle-wall coefficient of restitution(e_{p-w}) was measured by dropping the particle on a horizontal surface and measuring the height of a particle before and after collision using high-speed camera. The value was computed using:

$$e_{p-w} = \sqrt{\frac{H_1}{H_0}} \tag{4.42}$$

Particle-particle coefficient of restitution(e_{p-p}) was measured by mounting two particles on different pendulums and were made to collide with each other in a way that the position of both the particles (H_1) and (H_2) was measured after the collision for a varied amount of initial height(H_0). The value was computed using:

$$e_{p-p} = \frac{\sqrt{H_2} - \sqrt{H_1}}{\sqrt{H_0}} \tag{4.43}$$

Particle-wall coefficient of friction(μ_{p-w}) was measured by mounting some particles on sample trough and was made to slide on a hinged inclined plane with angle (α). The value was computed by:

$$\mu_{p-w} = \tan\alpha \tag{4.44}$$

Marigo and Stitt, 2015 calibrated the input parameters for pellets by performing various types of experiments such as fill level experiments in cylindrical containers, piling experiment, baffled rotating the drum and dynamic angle of repose in rotating drum. The results obtained in these experiments were replicated using DEM simulations. The pellets were modelled using the multi-sphere approach. The modelling of the pellets was also optimized by changing the arrangements and adding more small spheres at the edges of the cylindrical pellets.

Yan *et al.*, 2015 studied the effect of the input parameters to the DEM simulations using statistical analysis. The angle of repose simulations was done in which cylindrical container with an annular hole at the bottom was filled with spherical particles and then allowed to form heap on the ground and on the inner side of the cylinder. Three leveled sensitivity analysis was conducted with increasing complexities. Flow rate, angle of repose and particle velocity were the properties under observation. Changes in the simulation were observed by varying Young's modulus, coefficient of restitution and static/rolling coefficient of friction. It was observed that changing Young's modulus caused a change in the average velocity of the particles, but the height of the pile and the discharge time remained the same. Also, the computational time was found to be greatly reduced by decreasing Young's modulus value. Changes in the pile shape were observed in selective regions of the coefficient of restitution. A correlation between the effect of friction and the coefficient of restitution was observed. Friction terms had a more dominant effect on the flow rate and angle of repose. Increasing friction terms caused an increase in the angle of repose and a decrease in the flow rate.

Quist and Evertsson, 2015 proposed a generalized framework in the DEM model calibration (i.e. V-model for calibration of DEM model). This took into account the interdependencies of each property on one and hence by merely finding a single property would not guarantee the model performing best. Thus, it was proposed that the calibration process starts with calibration tests for various properties and then further verified by laboratory scale bulk density tests. Once the model performs satisfactorily in the laboratory test, then it could be applied to an industrial level problem. Therefore simulation with the appropriate calibration of the parameters affecting the flow phenomenon would reduce the time and efforts required for understanding and design of the system under consideration. The lab experiments proposed in this framework include multiple baffles in a transparent enclosure where a measured amount of material is allowed to flow. Properties such as the angle of repose, trajectory and settling time were observed with the change in hopper angle.

Derakhshani, Schott and Lodewijks, 2015 calibrated quartz sand for the angle of repose by employing periodic boundary condition. Both cylinder lifting and annular discharge methods were used. The effect of both sliding and rolling friction were studied on the angle of repose. It was found that rolling friction has a more dominant effect on the angle of repose than sliding friction. The discharge time was found to decrease with rolling friction but was not much affected by the sliding friction. Increase in the diameter of particle caused a decrease in the angle of repose.

Benvenuti, Kloss and Pirker, 2016 utilized artificial neural networks for calibration of bulk behavior. A number of DEM simulation were performed for training the artificial neural network. These simulations were the angle of repose and shear cell tests. After the neural network was trained, it was used to predict bulk experiments.

Rackl and Hanley, 2017 developed a new methodology for DEM calibration. Instead of performing simulations at fixed valued of input parameters, the simulations were carried for parameters with a range of values. These ranges were taken as an input for Latin hypercube modelling which made certain random sets of input data from the given range of input values. The result of these simulations was fed for kringing. Here the output given by the simulations were used to find the input values to get results in between the data provided by the simulation. In the next step, the error in the kringing was optimized by performing the simulation on the previous set of data. Thereby finally getting the DEM parameters calibrated.

Cabiscol, Finke and Kwade, 2018 calibrated the DEM parameters for cylindrical tablets using multi-sphere approach. Hertz-Mindlin model was used for particle-particle as well as particle-wall interactions. Coefficient of restitution was determined by dropping test. Uniaxial compression tests were conducted to find the shear modulus. Experiments included pouring test, angle of repose test and baffled rotating drum. First, the shape was calibrated to duplicate the tablet without having too many spheres. After that, a sensitivity analysis was done to find the effect of change in properties of bulk experiments. Further friction terms were calibrated one by one in the following order: sliding friction by using the dynamic angle of repose test in a baffled rotating drum, rolling friction test from pouring experiments and again a sliding friction calibration to filter out any interdependencies between the two terms. The final acceptability of the calibration was confirmed by the baffled rotating drum test.

Roessler and Katterfeld, 2018 worked on calibration by using the angle of repose test in such a way that larger sized particles were used for representing smaller actual particle. In this way, the computational speed increased as the number of independent particles reduced. The experimental setup consisted of a cylinder which was filled with dry sand and was lifted via a cable pulley arrangement. It was found that the angle of repose test was independent of the test rig size. The cylinder lifting velocity affected the angle of repose. It was found that the same coefficient of friction terms can be used for a different type of particles.

Ye *et al.*, 2019 used backpropagation neural network for the calibration of DEM parameters. The static and dynamic angle of repose was used to train the neural network. It was found that

the lower angle of repose increases with an increase in elastic modulus. The angle of repose increases with an increase in static friction coefficient. The upper angle was higher for dynamic and lower for the static angle of repose. It was found that the angle of repose was more sensitive to static friction coefficient between wall and particle in the case of the dynamic angle of repose

Kanakabandi and Goswami, 2019 calibrate DEM parameters for black pepper using the angle of repose test. The sensitivity analysis showed that the angle of repose increases with the increase of the following in decreasing order: coefficient of rolling friction(particle-particle), coefficient of static friction(particle-particle), coefficient of static friction(particle-wall), coefficient of restitution(particle-wall), coefficient of rolling friction(particle-wall) followed by coefficient of restitution(particle-particle). A reduction of the angle of repose was reported with an increase in shear modulus.

4.2.5 SHORTCOMINGS OF PREVIOUS RESEARCH

The literature review done points out the following:

i. Calibration has only been done for large and coarse powders (10 mm to 0.5 mm).
ii. The angle of repose test is most extensively used.
iii. Method of selection of time step is not discussed.
iv. The experimental setups used required manual intervention which could lead to substantial error.

4.3 OBJECTIVES

i. To simulate bulk density test in EDEM
ii. To find the effect of various particle properties on bulk density test.
iii. To validate simulation results against practical results.
iv. To calibrate the powder for bulk density test

4.4 MATERIAL AND METHODS

Material

The bulk material used for the fine powder calibration is air preheater (APH) flyash.

The measured properties are given in Table 4.2.

Property	Value
Particle Density	1870 kg/s
Tapped Density	1229 kg/s
Bulk Density	815 kg/s

Table 4.2 : Bulk properties for APH fly ash

Standard bulk density test was performed on APH fly ash on Brookfield Powder Flow Tester (PFT) shown in Figure 4.17. Powder flow tester is used to analyze the flow characteristics of powders. It is used to measure various flow properties of a bulk solid such as unconfined failure strength, major principle consolidation stress, angle of internal friction, angle of wall friction, cohesive strength and bulk density.

Figure 4.17 : Brookfield Powder Flow Tester

The powder sample is placed in the sample trough and then prepared by using a plow. Depending upon the type of test different side of the plow and different type of lid are used. For bulk density test the flat side of the plow is used which makes the upper surface of the powder sample flat. The lid used in bulk density test is also flat.

The test starts after the trough and lid are placed into position. The top lid moves downwards and starts to compress the sample. The results obtained are simultaneously displayed on the computer.

Standard Bulk Density Test results for APH fly ash are given in Table 4.3.

$\sigma_1(kPa)$	$\rho_b(kg/m^3)$
0.095	859.80
0.288	878.80
0.529	899.43
1.065	932.43
2.262	979.27
4.930	1023.43

Table 4.3 : Bulk density test for APH fly ash

Figure 4.18 is a plot between the bulk density and the normal stress obtained for APH fly ash. There was an increase of about 150 kg/m3 in the density of the sample during the test. This curve shows a rapid increase in density at the beginning. The change in density corresponding to normal stress decreases at higher stress values.

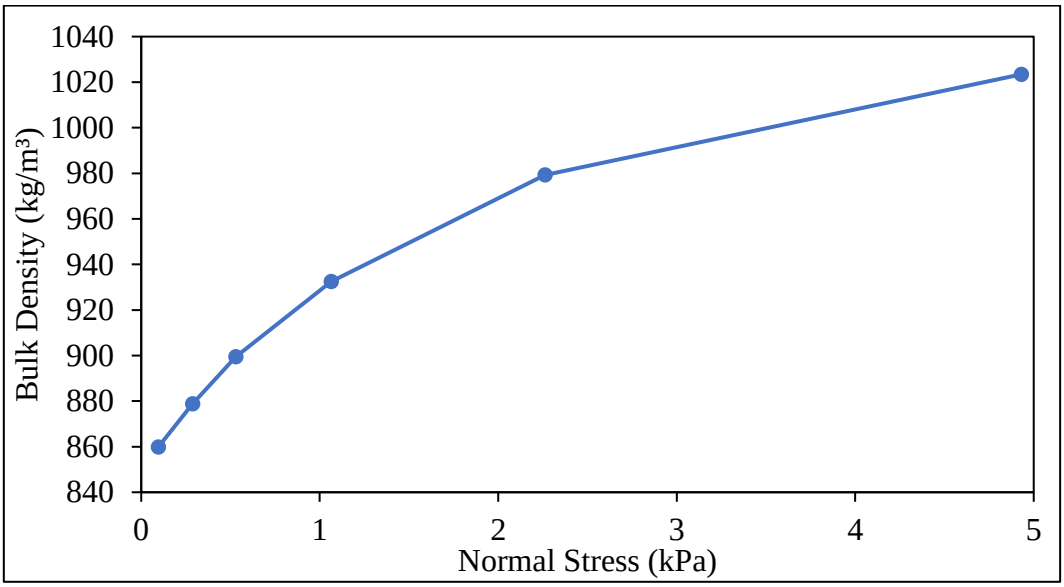

Figure 4.18 : Bulk density vs normal stress for APH fly ash

Method

Bulk density test was simulated in EDEM. Various DEM parameters were varied to study the effect on the test results. The test parameters for standard bulk density test were obtained by using basic mathematical calculations. Raw data obtained from the simulation was first changed into density and stress data. The complete data was filtered to find out the density values at the specific stress values that were obtained by the actual powder testing done on PFT. The stress values that were obtained from the simulation data was not exactly the same as the stress value obtained by PFT. These stress values were the closest stress values that were available.

4.5 SIMULATION

3D model of the PFT trough (Figure 4.19) and the top lid(Figure 4.20) were made.

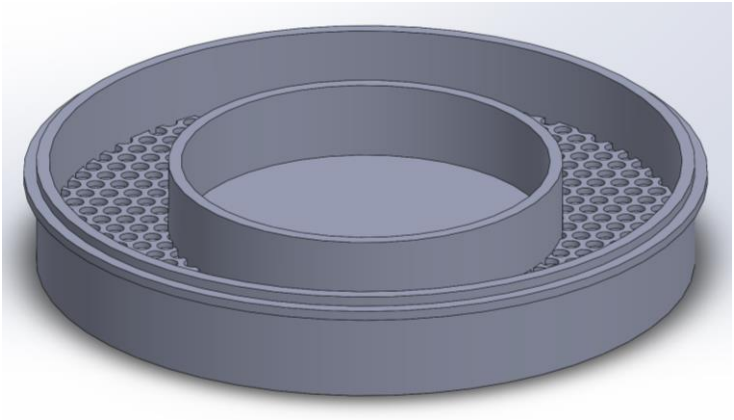

Figure 4.19 : 3D model of PFT trough

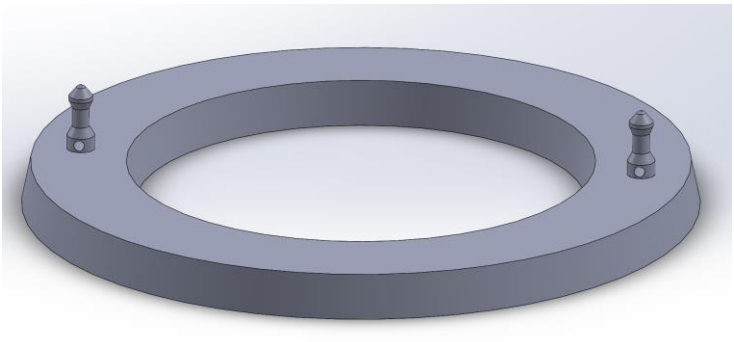

Figure 4.20 : 3D model of PFT top lid (507)

The bottom plate was filled with particles from an annular-shaped factory. The middle portion of the trough was removed to get rid of any particles that get trapped in it. The overfilled trough is shown in Figure 4.21.

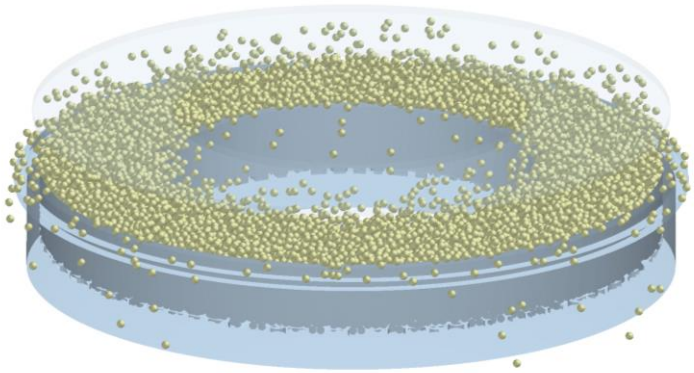

Figure 4.21 : Trough filling

The excess material was removed after the trough was filled (Figure 4.22). The removal of the extra particle was done by reducing the computational boundary. This ensured that the particles are not compressed in the process.

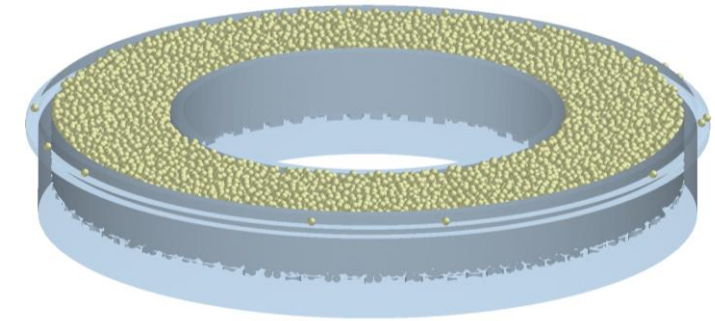

Figure 4.22 : Filled trough ready for compression

Now the top lid was used to compress the particles in the trough (Figure 4.23). The speed of the trough was 1 mm/s. This speed was obtained from the actual PFT result. The lid was pressed against the particles until the stress reached around 5kPa. This was done because the maximum stress in the standard bulk density was around 5kPa.

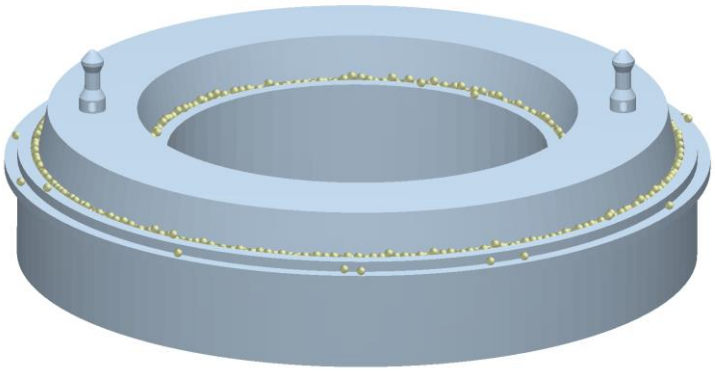

Figure 4.23 : Top lid compressing the particles

The raw data from the simulation was used to obtain bulk density at the stress corresponding to standard bulk density test. It was found that a very specific data query is to be made as there are many options is EDEM. The query parameters used in this case are tabulated in Table 4.4.

Attribute	**Component**	**Type**	**Group**	**Selection**
Mass		Total	Particle	All
Distance	Z-axis	Minimum	Geometry	TOP_PFT_01
Total Force	Z-axis	Total	Geometry	TOP_PFT_01

Table 4.4 : Data query parameters

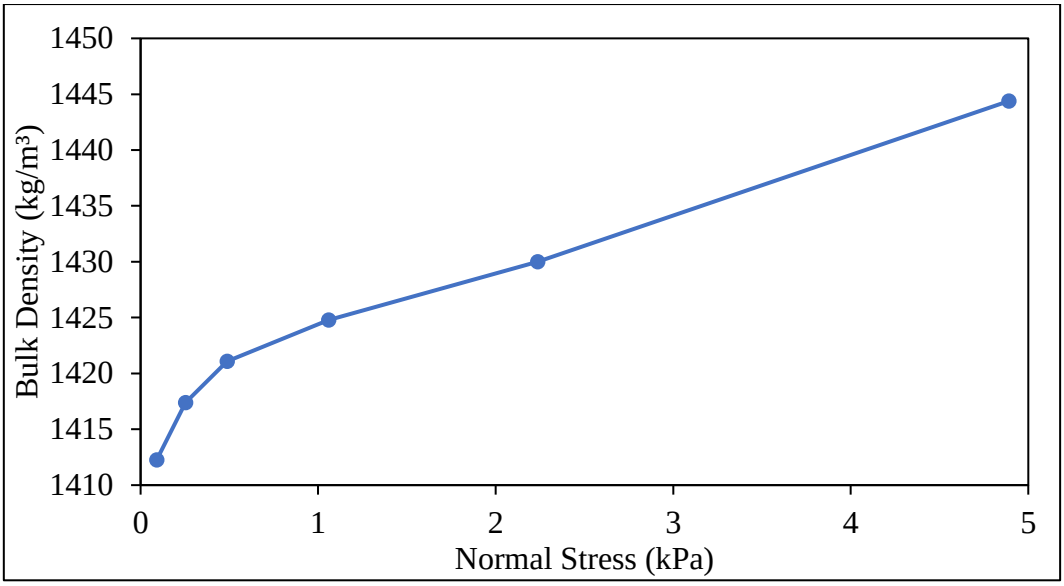

Figure 4.24 : Output from PFT trough simulation

Figure 4.24 shows the bulk density curve obtained for spherical particles of diameter equal to 2mm. The PFT trough simulation took a lot of simulation time. Due to the complications of the experiment, each experiment required manual intervention at each and every step i.e. filling, scraping, compressing. Thus, to reduce the computational time a comparatively smaller setup was used. In this setup, a cylinder with an open top was used to replace the PFT trough and a simple circular disc was used to compress the bulk material. This approach reduced the computational time from 4 days to 3 hours for a specific size of particles. Figure 4.25 shows the dimensions of the cylinder used for bulk density test.

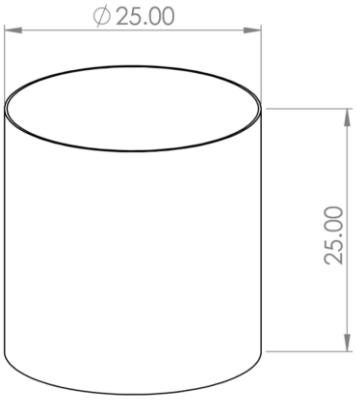

Figure 4.25 : Cylinder dimensions

Figure 4.26 shows the cylindrical container after it has been filled with spherical particles. The extra particles were removed by reducing the environment boundaries of the simulation.

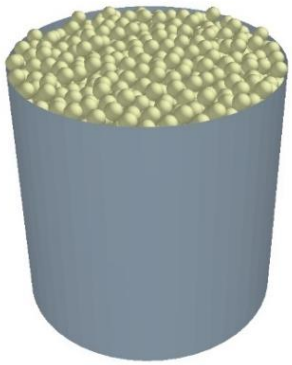

Figure 4.26 : Cylinder ready for compression

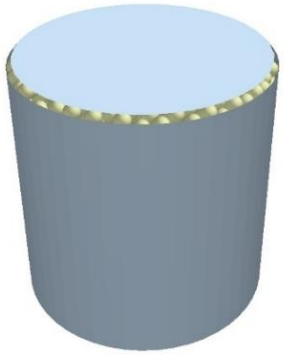

Figure 4.27 : Circular lid compressing the particles

It was found that there was a difference in the results given by the trough and the cylinder (Figure 4.28). The density given by the trough compression was comparatively higher for the same DEM parameters.

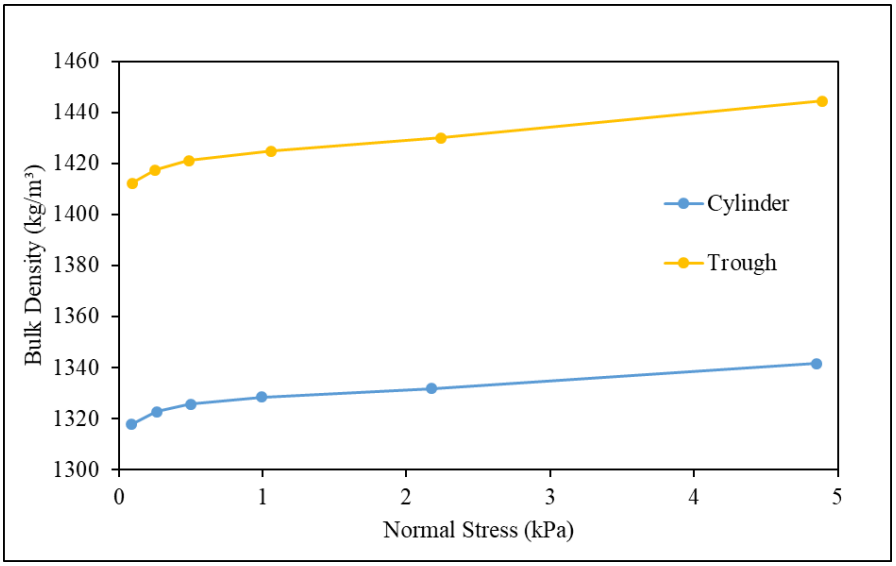

Figure 4.28 : Comparison of trough and cylinder data

The bulk density simulation results for the same particles done using PFT trough and cylindrical container are compared in Figure 4.28. It can be observed that both the curves are similar in nature except that both are at an offset to each other. This offset is due to the scaling down of the experimental setup. For the same size of particles, the void percentage in the small cylinder would be more thus the density of the particles will comparatively less. Because the prime objective of the calibration would be to get the same curve shape. It would be further discussed that changing the particle density during calibration can take care of the offset in the result. Thus, the curve generated by the cylinder simulation is an offset to the curve given by PFT trough.

4.6 RESULTS AND DISCUSSION

Following parameters were varied to find their effect on the standard bulk density test:

1. **Particle Density:** It was found that if the density of the particles increased and all the other properties were kept the same then the shape of the graph remains the same. Figure 4.29 shows that even though the shape of the curves remains the same, the graphs obtained by varying the particle density were an offset to each other. This is because particle density has a direct effect on the bulk density of the material. The offset for a constant amount of change in particle density is same. The curve denoting higher bulk density corresponds to the simulation where particle density was higher.

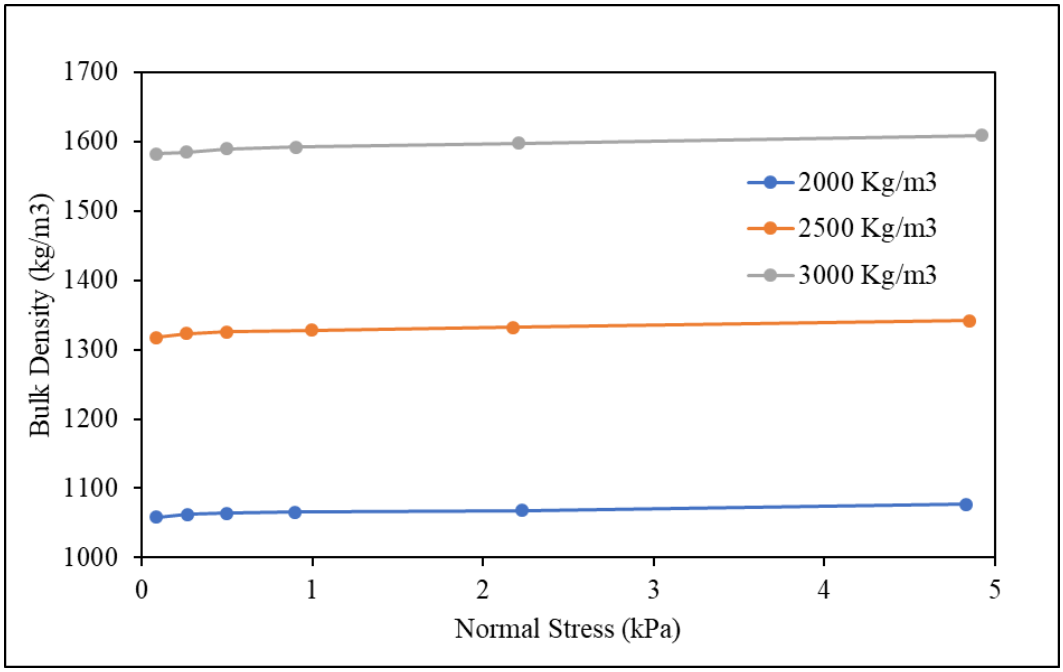

Figure 4.29 : Effect of particle density on bulk density test

2. **Size:** The effect of changing the particle size, keeping all other parameters same can be seen in Figure 5.30. It shows that as the size of the particle is reduced the graph offsets to a higher value. This is because in the case of small spherical particles the void fraction reduces thus the density increases. It was found that the shape of the graphs was identical. If should be noted that the offset is not equal for an equal change in the particle diameter. The change for the smaller sized particle is more than that of the change in larger particles.

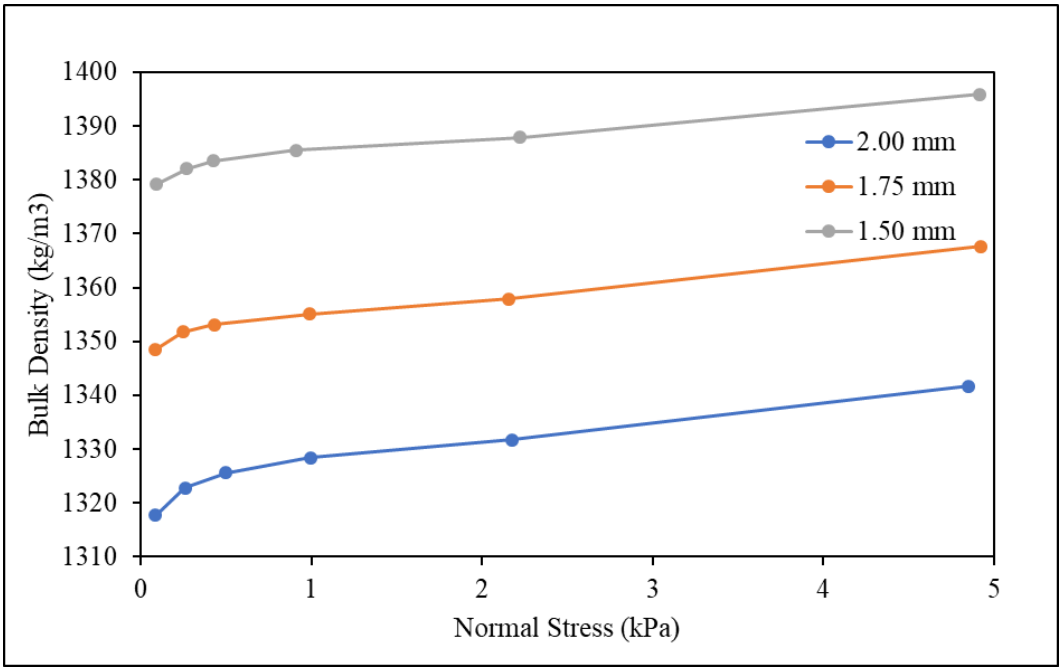

Figure 4.30 : Effect of particle size on bulk density test

3. **Shear Modulus:** The effect of changing the shear modulus, keeping all other parameters same can be seen in Figure 4.31. Change in the shear modulus changes the shape of the graph. The density of particles having larger shear modulus value is higher than that of others. The starting point is almost the same for all the particles but as the normal stress increases the graph segregates.

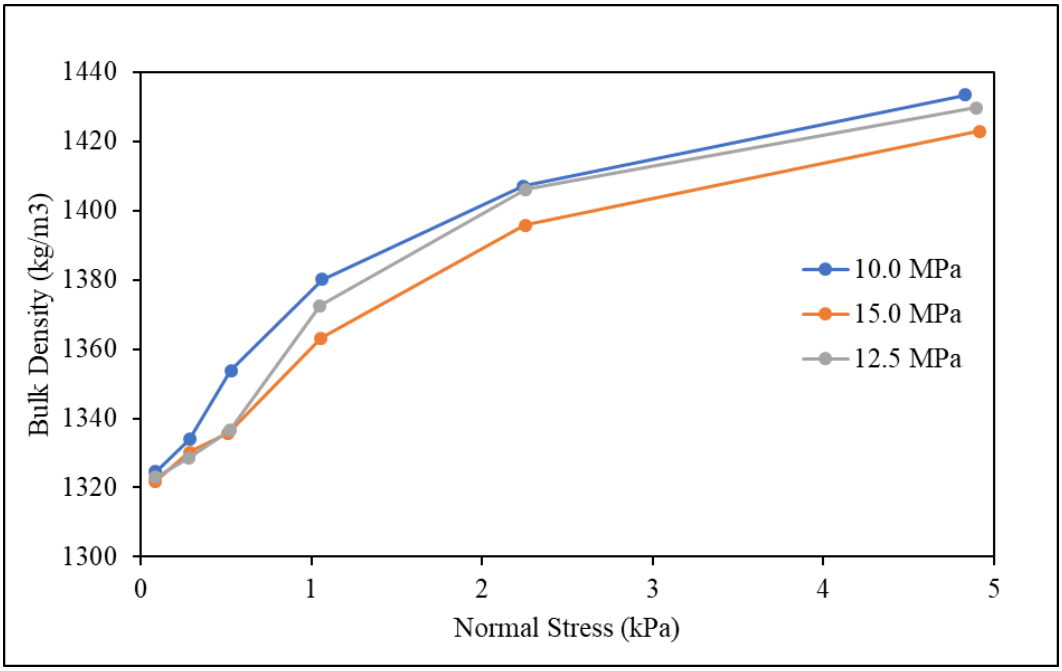

Figure 4.31 : Effect of shear modulus on bulk density test

4. **Poisson's Ratio:** The effect of changing Poisson's ratio, keeping all other parameters same can be seen in Figure 4.32. Similar to shear modulus the graph originates from the same place. Initially, the graph has no direct relationship with the increase in Poisson's ratio. But, with the decrease in Poisson ratio the slope of the graph increases towards the end of the graph.

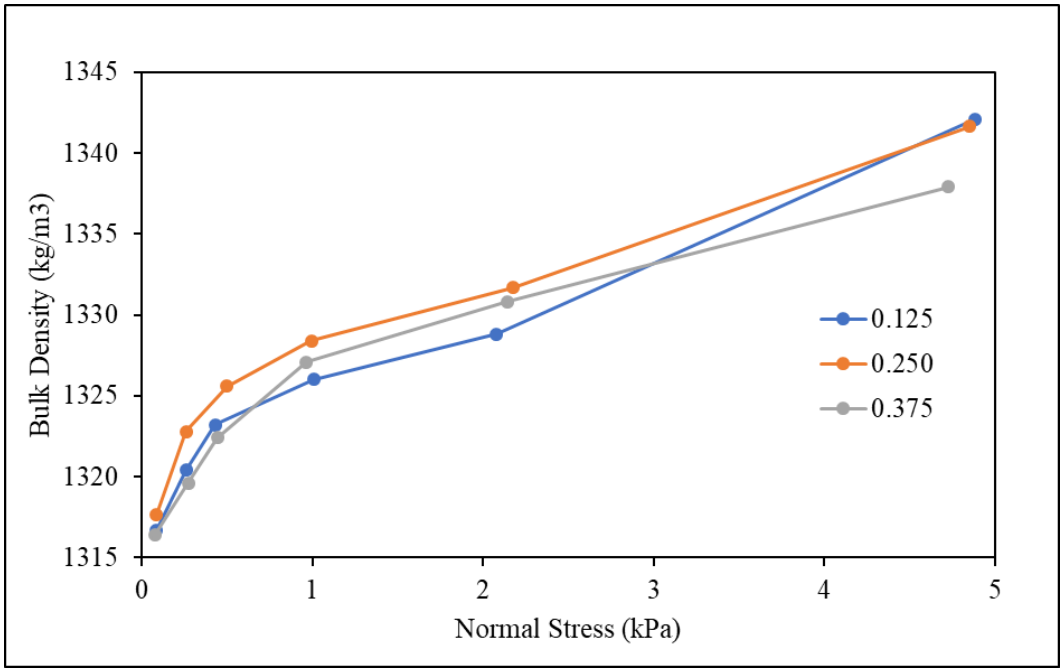

Figure 4.32 : Effect of Poisson's ratio on bulk density test

5. **Coefficient of restitution:** The effect of changing the coefficient of restitution, keeping all other parameters same can be seen in Figure 4.33. Here the graphs don't start from the same place. The graph for a higher coefficient of restitution is at the top and the change caused is nonlinear. This is because while filling the container the particles having a higher coefficient of restitution fill the voids properly due to higher kinetic energy available to them. The slope of the graph for higher stress values is more for low coefficient of restitution values. This sudden rise is because of the fact that particles with a low coefficient of restitution occupy a relatively unstable position during filling. Thus, when pressure is applied the particles, they immediately start to reorganize themselves leading to a quick increase in density.

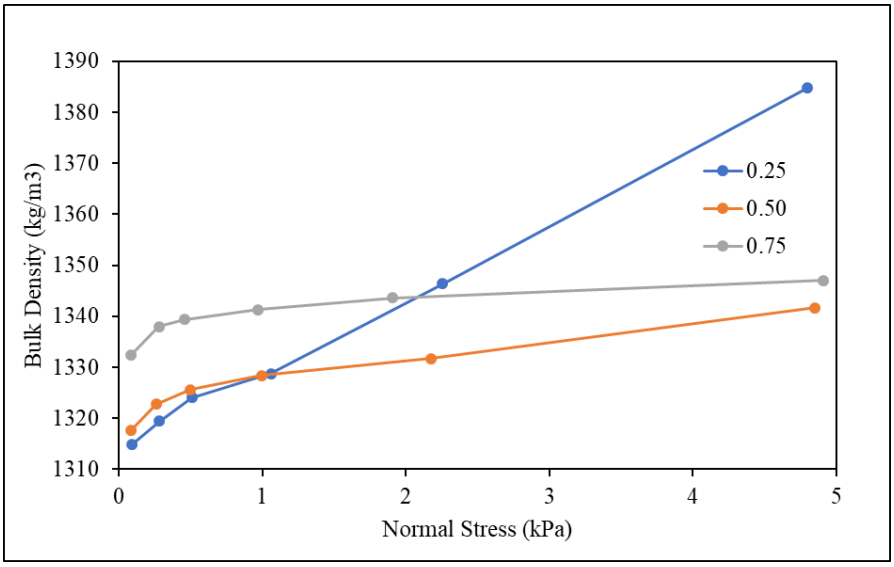

Figure 4.33 : Effect of coefficient of restitution on bulk density test

6. **Coefficient of static friction:** The effect of changing the coefficient of static friction, keeping all other parameters same can be seen in Figure 4.34. The graph here offsets to a higher value with a decrease in the coefficient of sliding friction. The change in the offset in nonlinear and increases with a decrease in static friction. This is because the particles having low static friction easily occupy a stable position. The fact that the shape of the graph remains the same indicates that the change in static friction does not affect the particle arrangement taking place towards the end of compression. Although the curve slope is slightly higher for minimum static friction towards the end. This can be attributed to the fact that these particles face less resistance to movement for their adjustment.

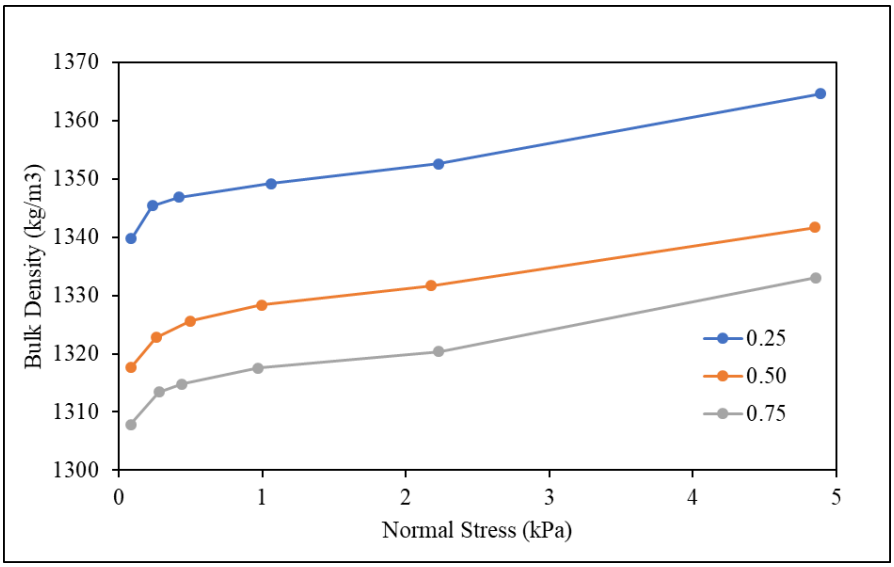

Figure 4.34 : Effect of coefficient of static friction on bulk density test

7. **Coefficient of Rolling Friction:** The effect of changing the coefficient of rolling friction, keeping all other parameters same can be seen in Figure 4.35. The graph here offsets to a higher value with a decrease in the coefficient of rolling friction. The change in the offset of the first point is nonlinear. The density for the first data point drastically increases for lower rolling friction values. This is because the particle is subjected to less friction force in order to arrange itself while the filling process. The slope of the graphs towards the end increase for higher values of rolling friction. This is because the rolling friction caused the particle to occupy unstable positions. As the pressure is increased the particles are quickly adjusted to increase the density.

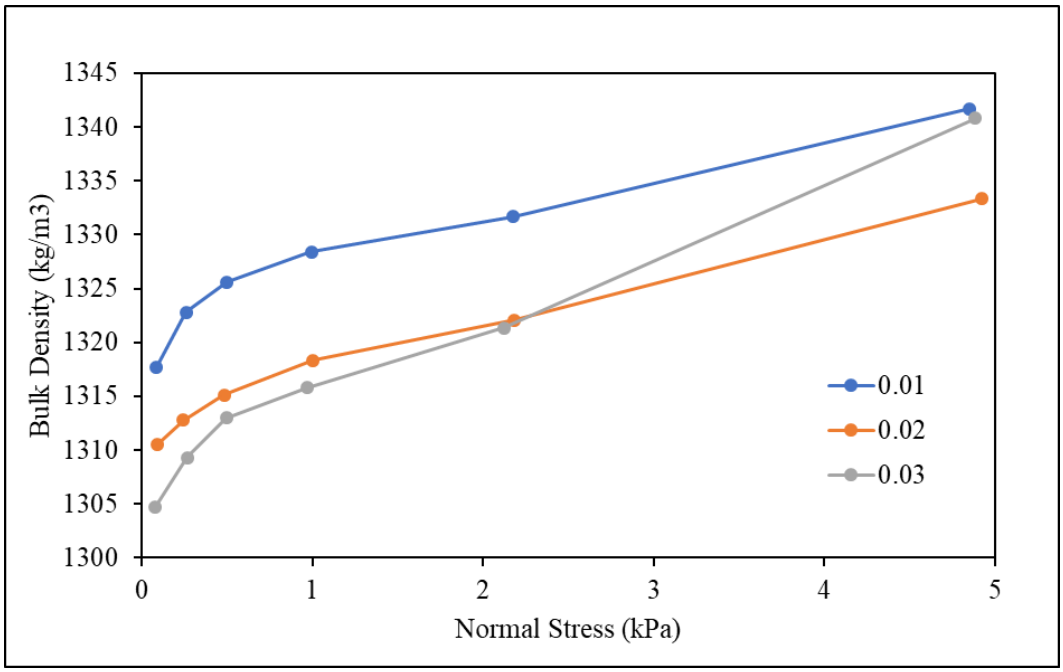

Figure 4.35 : Effect of coefficient of rolling friction on bulk density test

8. **Shape:** Here a comparison was made between spherical particles and tetragonal particles (Figure 4.36). The geometric parameters of the tetragonal particle are given in Table 4.5. The diameter of the sphere used is 1.2 mm and the distance between the center of two adjoining spheres is 1mm. The effect of changing the particle shape, keeping all other parameters same can be seen in Figure 4.37. The tetragonal model was used because it could provide more unstable orientations while filling that could help in modelling of fine powders. It was found that the density of the tetragonal particle was less compared to the density of the spherical particle. This was due to the shape of the particles.

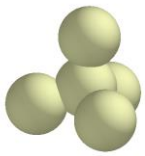

Figure 4.36 : Tetrahedral Particle

Particle No.	x	y	z
1	0	0	0
2	0	1	0
3	0.94281	-0.33333	0
4	-0.54433	-0.33333	0.7698
5	-0.54433	-0.33333	-0.7698

Table 4.5 : Geometric parameters of tetrahedral shape

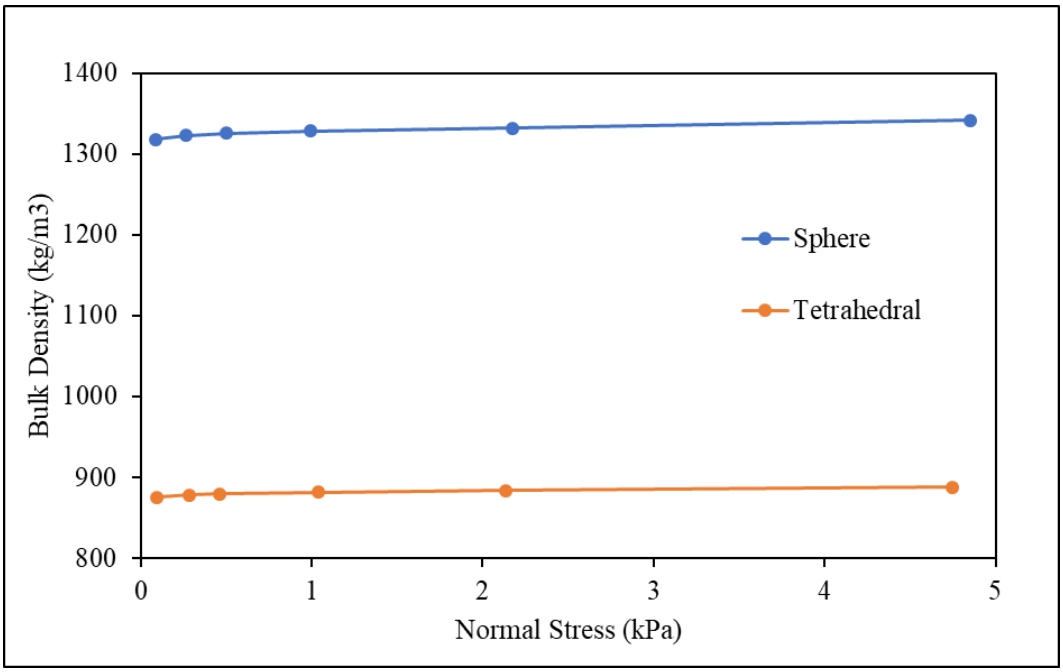

Figure 4.37 : Effect of particle shape on bulk density test

Calibration

i. **Using Spherical Particles:** Figure 4.38 shows the various attempts that were made to replicate the actual data obtained by experimentation. But a large amount of compressibility that was exhibited by the experimentation results could not be replicated. This can be attributed to the deficiency of particle arrangement and adjustment during the compression in the spherical particles. The spherical particles couldn't provide a large amount of density change by only changing the DEM parameter.

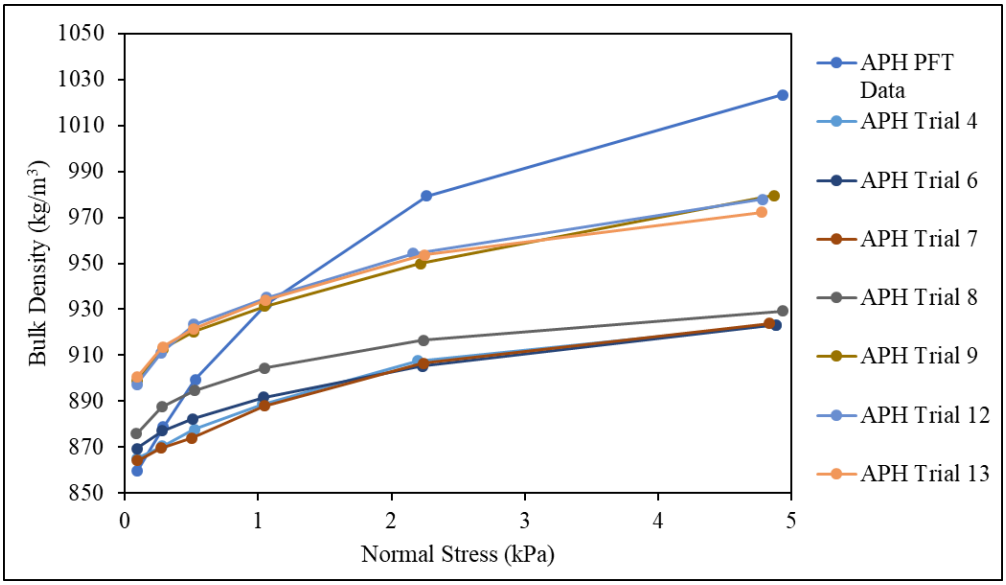

Figure 4.38 : Calibration of bulk density test using spherical particles

ii. **Using Tetragonal Particles:** Tetrahedral particles performed better in capturing the compressible nature of fine powder in comparison to spherical particles. Figure 4.39 shows the results of various simulation that were done to replicate the experimental simulation. The reason why tetrahedral particles performed well was due to the fact that large density increase was registered for the same stress values. This was because the tetragonal shape allows more nonstable filling in comparison to spherical particles. The nature of the graph changed from convex to concave for a particular value of Shear Modulus. Although trial 3, 4 and 8 showed promising results but the experimental data could not be replicated.

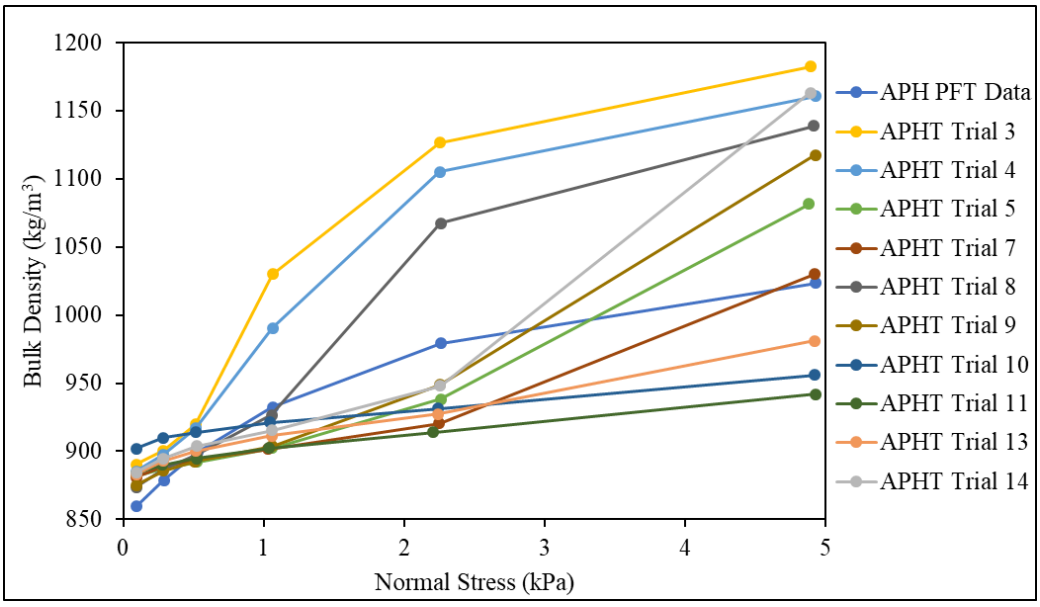

Figure 4.39 : Calibration of bulk density using tetrahedral particle

4.7 CONCLUSION

Simulation of standard bulk density test was performed in EDEM software. The various DEM parameters require for modelling of the particles were varied to find their effect on the result of standard bulk density test. It was found that properties such as particle size, Shear Modulus, particle shape, coefficient of static and rolling friction affected the results profoundly. Changing the poison's ratio did not bring about any significant change in the test results. It was found that calibration of fine powders using spherical shaped particles is difficult because they were not very compressible even after making many variations in the property. Tetrahedral shape particles, on the other hand, were successful in modelling the compressible nature of particles but they were not able to entirely replicate the experimental results.

CHAPTER 5 : CONCLUSION AND FUTURE SCOPE

5.1 CONCLUSION

A number of flow meters were designed, fabricated and installed for measuring air flow in the pneumatic conveying test rig in bulk solids handling lab. The flow meters were used to measure total air, conveying air, fluidizing air, and top air. The calibration for all the flow meters was done and the coefficient of discharge values for all the flow meters was obtained.

A separate flow meter was fabricated and calibrated to measure fluidization air at NTPC thermal power plant Mauda, Maharashtra.

A case study was carried out to solve dew formation problem inside pneumatic conveying pipeline at NTPC thermal power plants. It was found that due to the absence of air-drying plant, the compressed air in the pneumatic conveying line facilitated the formation of dew in pipeline. These water droplets combined with the fly ash to form a coating inside the pipeline. The reduced internal diameter of the conveying pipeline increases the pressure drop and causes pipeline blockage, especially during winter and monsoon season. Thus, it was suggested that air drying plants be installed with compressors used for pneumatic conveying at thermal power plants.

An attempt was made to calibrate DEM parameters of fine powder using bulk density test. Air preheater fly ash sample was used for the calibration process. The effect of various parameters on the bulk density test was studied. The simulation was done using spherical and tetrahedral shaped particles to match the results obtained by experimentation. It was found that spherical shaped particles were not able to model the compressive nature exhibited by fine powders. On the other hand, tetrahedral particles were able to model the compressible behavior exhibited by fine powder. But it could not replicate the exact behavior of the fine powder.

5.2 FUTURE SCOPE

Calibration of DEM parameters still remain an unsolved problem. Various industries suffer hugely due to absence of fine powder calibration. One can employ various other shapes of particle for calibration of DEM parameters. Other test such as flow function test, time consolidation test, wall friction test could be used to calibrate of DEM parameters such that all the important behaviour of fine powders can be modelled.

REFERENCES

Abdelmotalib, H. M. *et al.* (2015) ‘Heat transfer process in gas-solid fluidized bed combustors: A review’, *International Journal of Heat and Mass Transfer*. Elsevier Ltd, 89, pp. 567–575. doi: 10.1016/j.ijheatmasstransfer.2015.05.085.

Alizadeh, M. *et al.* (2018) ‘A methodology for calibration of DEM input parameters in simulation of segregation of powder mixtures, a special focus on adhesion’, *Powder Technology*. Elsevier B.V., 339, pp. 789–800. doi: 10.1016/j.powtec.2018.08.028.

Benvenuti, L., Kloss, C. and Pirker, S. (2016) ‘Identification of DEM simulation parameters by Artificial Neural Networks and bulk experiments’, *Powder Technology*, 291, pp. 456–465. doi: 10.1016/j.powtec.2016.01.003.

Cabiscol, R., Finke, J. H. and Kwade, A. (2018) ‘Calibration and interpretation of DEM parameters for simulations of cylindrical tablets with multi-sphere approach’, *Powder Technology*. Elsevier B.V., 327, pp. 232–245. doi: 10.1016/j.powtec.2017.12.041.

Campbell, C. S. (1985) ‘Computer simulation of granular shear flows’, *Journal of Fluid Mechanics*, 151, pp. 167–188. Available at: http://journals.cambridge.org/production/action/cjoGetFulltext?fulltextid=390509.

Choo, K. S. and Kim, S. J. (2010) ‘Comparison of thermal characteristics of confined and unconfined impinging jets’, *International Journal of Heat and Mass Transfer*. Elsevier Ltd, 53(15–16), pp. 3366–3371. doi: 10.1016/j.ijheatmasstransfer.2010.02.023.

Dahl, S. R. and Hrenya, C. M. (2004) ‘Size segregation in rapid, granular flows with continuous size distributions’, *Physics of Fluids*, 16(1), pp. 1–13. doi: 10.1063/1.1626682.

Dahl, S. R. and Hrenya, C. M. (2005) ‘Size segregation in gas-solid fluidized beds with continuous size distributions’, *Chemical Engineering Science*, 60(23), pp. 6658–6673. doi: 10.1016/j.ces.2005.05.057.

Derakhshani, S. M., Schott, D. L. and Lodewijks, G. (2015) ‘Micro-macro properties of quartz sand: Experimental investigation and DEM simulation’, *Powder Technology*. Elsevier B.V., 269, pp. 127–138. doi: 10.1016/j.powtec.2014.08.072.

Fraczek, J., Złobecki, A. and Zemanek, J. (2007) ‘Assessment of angle of repose of granular plant material using computer image analysis’, *Journal of Food Engineering*, 83(1), pp. 17–

22. doi: 10.1016/j.jfoodeng.2006.11.028.

Geldart, D. (1973) ‘Types of Fluidization’, *Powder Technology*, 7(5), pp. 285–292. Available at: http://dns2.asia.edu.tw/~ysho/YSHO-English/1000 CE/PDF/Pow Tec7, 285.pdf.

González-Montellano, C. *et al.* (2012) ‘Determination of the mechanical properties of maize grains and olives required for use in DEM simulations’, *Journal of Food Engineering*, 111(4), pp. 553–562. doi: 10.1016/j.jfoodeng.2012.03.017.

Gui, N. and Fan, J. R. (2009) ‘Numerical simulation of motion of rigid spherical particles in a rotating tumbler with an inner wavelike surface’, *Powder Technology*. Elsevier B.V., 192(2), pp. 234–241. doi: 10.1016/j.powtec.2009.01.004.

Hertz, V. H. H. (1882) ‘lieber die Berührung fester elastischer Körper .’, pp. 156–171.

Hofer, G., Schöny, G. and Pröll, T. (2018) ‘Acting on hydrodynamics to improve the local bed-to-wall heat transfer in bubbling fluidized beds’, *Chemical Engineering Research and Design*. Institution of Chemical Engineers, 134, pp. 309–318. doi: 10.1016/j.cherd.2018.04.015.

Hoomans, B. P. B. *et al.* (1996) ‘Discrete particle Simulation of Bubble and Slug Formation in a 2D Gas-Fluidised Bed: A Hard-Sphere Approach’, *Science*, 51(1), pp. 99–118.

Hoomans, B. P. B., Kuipers, J. A. M. and Van Swaaij, W. P. M. (2000) ‘Granular dynamics simulation of segregation phenomena in bubbling gas- fluidised beds’, *Powder Technology*, 109(1–3), pp. 41–48. doi: 10.1016/S0032-5910(99)00225-9.

‘ISO 1239 (Part 1)’ (2004). India: Bureau of Indian Standards (BIS).

ISO 5167-1: 2003, 2003. Measurement of fluid flow by means of pressure differential devices inserted in circular cross-section conduits running full–Part 1: General principles and requirements.

ISO 5167-2 (2003) ‘Measurement of fluid flow by means of pressure differential devices inserted in circular cross-section conduits running full -- Part 2: Orifice plates’, *International Standard Organisation*, 3, p. 24.

ISO TR 9464 (1998) ‘Guidelines for the use of ISO 5167-1:1991’, *Iso Tr*, 3.

Janssen, H., Blocken, B. and Carmeliet, J. (2007) ‘Conservative modelling of the moisture and heat transfer in building components under atmospheric excitation’, *International Journal of Heat and Mass Transfer*, 50(5–6), pp. 1128–1140. doi:

10.1016/j.ijheatmasstransfer.2006.06.048.

Kanakabandi, C. K. and Goswami, T. K. (2019) ‘Determination of properties of black pepper to use in discrete element modelling’, *Journal of Food Engineering*. Elsevier, 246(November 2018), pp. 111–118. doi: 10.1016/j.jfoodeng.2018.11.005.

Kuraan, A. M., Moldovan, S. I. and Choo, K. (2017) ‘Heat transfer and hydrodynamics of free water jet impingement at low nozzle-to-plate spacings’, *International Journal of Heat and Mass Transfer*. Elsevier Ltd, 108, pp. 2211–2216. doi: 10.1016/j.ijheatmasstransfer.2017.01.084.

Li, J. and Kuipers, J. A. M. (2002) ‘Effect of pressure on gas-solid flow behavior in dense gas-fluidized beds: A discrete particle simulation study’, *Powder Technology*, 127(2), pp. 173–184. doi: 10.1016/S0032-5910(02)00116-X.

Li, J. and Kuipers, J. A. M. (2005) ‘On the origin of heterogeneous structure in dense gas-solid flows’, *Chemical Engineering Science*, 60(5), pp. 1251–1265. doi: 10.1016/j.ces.2004.09.083.

Marigo, M. and Stitt, E. H. (2015) ‘Discrete element method (DEM) for industrial applications: Comments on calibration and validation for the modelling of cylindrical pellets’, *KONA Powder and Particle Journal*, 32(32), pp. 236–252. doi: 10.14356/kona.2015016.

Mindlin and D., R. (1953) ‘Elastic Spheres in Contact Under Varying Oblique Forces’, *J. Applied Mech.*, 20, pp. 327–344.

Mittal, A. and Mallick, S. S. (2016) *Investigation into Pressure Signal Fluctuations during Fluidized Dense-Phase Pneumatic Conveying of Powders*. Thapar University, Patiala.

Powers, M. C. (1953) ‘Journal of Sedimentary Research Volume Vol. 23 issue 1953 [doi 10.1306%2FD4269567-2B26-11D7-8648000102C1865D] M. C. Powers, -- A New Roundness Scale for Sedimentary Particles.pdf’, 23(2), pp. 117–119.

Quist, J. and Evertsson, M. (2015) ‘Framework for DEM Model Calibration and Validation’, *Proceedings of the 14th European symposium on comminution and classification*, pp. 103–108.

Rackl, M. and Hanley, K. J. (2017) ‘A methodical calibration procedure for discrete element models’, *Powder Technology*. Elsevier B.V., 307, pp. 73–83. doi:

10.1016/j.powtec.2016.11.048.

Ramgopal, M. (2009) *Refrigeration and Air Conditioning, National Programme on Technology Enhanced Learning (NPTEL)*. Available at: https://nptel.ac.in/courses/112105129/pdf/R&AC Lecture 27.pdf (Accessed: 11 August 2018).

Reza Norouzi, H. *et al.* (2016) *Coupled CFD-DEM Modelling Formulation, Implementation and Application to Multiphase Flows, John Wiley & Sons, Ltd*. John Wiley & Sons, Ltd.

Richardson, D. C. *et al.* (2011) 'Numerical simulations of granular dynamics: I. Hard-sphere discrete element method and tests', *Icarus*. Elsevier Inc., 212(1), pp. 427–437. doi: 10.1016/j.icarus.2010.11.030.

Roessler, T. and Katterfeld, A. (2018) 'Scaling of the angle of repose test and its influence on the calibration of DEM parameters using upscaled particles', *Powder Technology*. Elsevier B.V., 330, pp. 58–66. doi: 10.1016/j.powtec.2018.01.044.

Roessler, T. and Katterfeld, A. (2019) 'DEM parameter calibration of cohesive bulk materials using a simple angle of repose test', *Particuology*. Chinese Society of Particuology, (2018). doi: 10.1016/j.partic.2018.08.005.

Schulze, D. (2010) *Powders and Bulk Solids, Chemie Ingenieur Technik*. doi: 10.1002/cite.201090034.

Weber, M. W., Hoffman, D. K. and Hrenya, C. M. (2004) 'Discrete-particle simulations of cohesive granular flow using a square-well potential', *Granular Matter*, 6(4), pp. 239–254. doi: 10.1007/s10035-004-0179-5.

Yan, Z. *et al.* (2015) 'Discrete element modelling (DEM) input parameters: understanding their impact on model predictions using statistical analysis', *Computational Particle Mechanics*. Springer International Publishing, 2(3), pp. 283–299. doi: 10.1007/s40571-015-0056-5.

Ye, F. *et al.* (2019) 'Calibration and verification of DEM parameters for dynamic particle flow conditions using a backpropagation neural network', *Advanced Powder Technology*. The Society of Powder Technology Japan, 30(2), pp. 292–301. doi: 10.1016/j.apt.2018.11.005.

COMMUNICATIONS

Kamaluddin, K., Mallick, S.S., Mittal, A. (2019), An Investigation into the requirement of air drying plant in transport air system for pneumatic conveying of fly ash – A case Study, International O&M Conference – Indian Power Stations – 2019, 13-14 Feb 2019, Raipur, p.53

APPENDIX I

The graphs used for selection of β values for all the flow range are as follows:

I. Total air line (3 Inch)

i. 0.01 to 0.08 kg/s; β=0.40

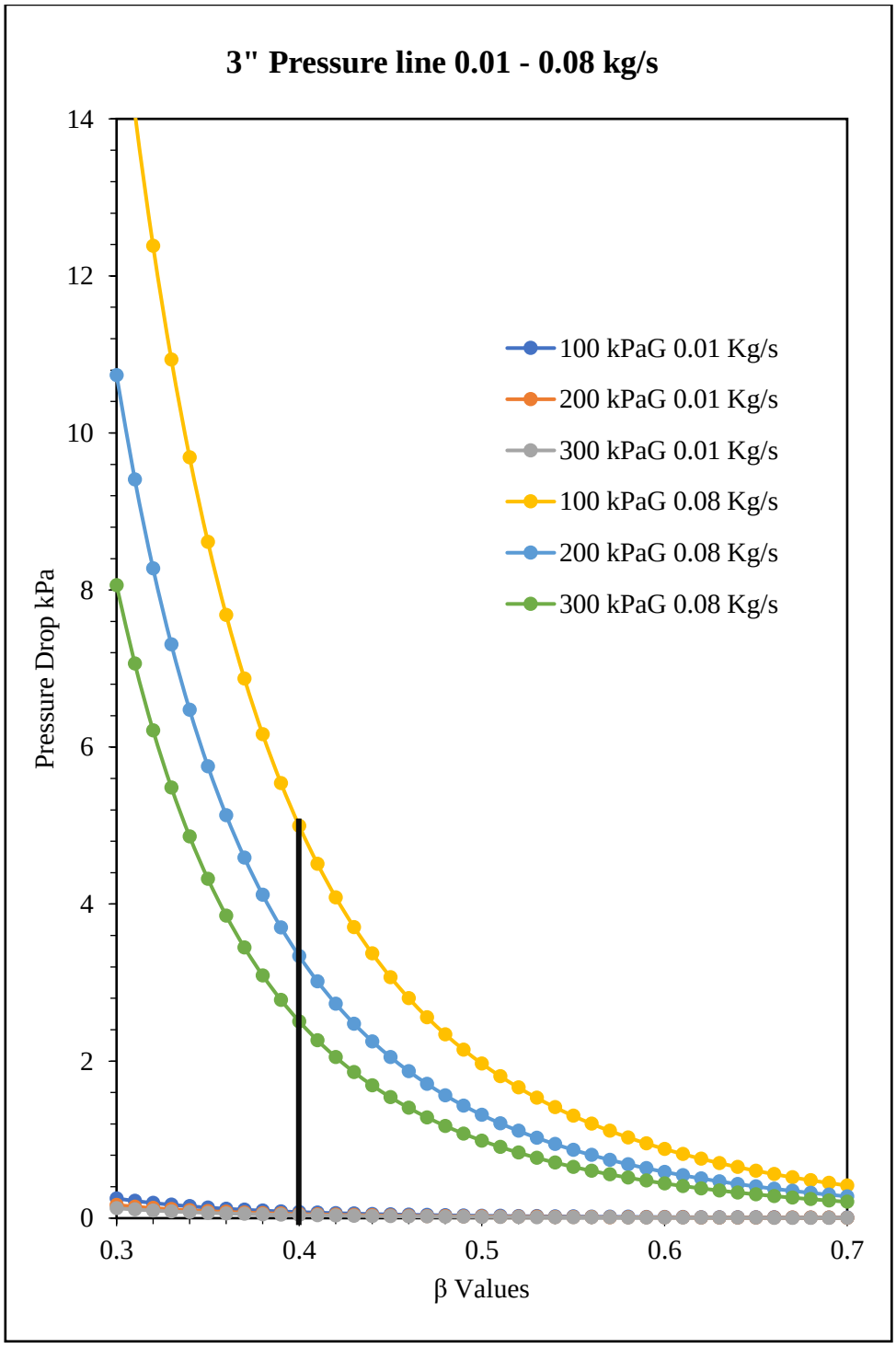

ii. 0.08 to 0.15 kg/s; β=0.50

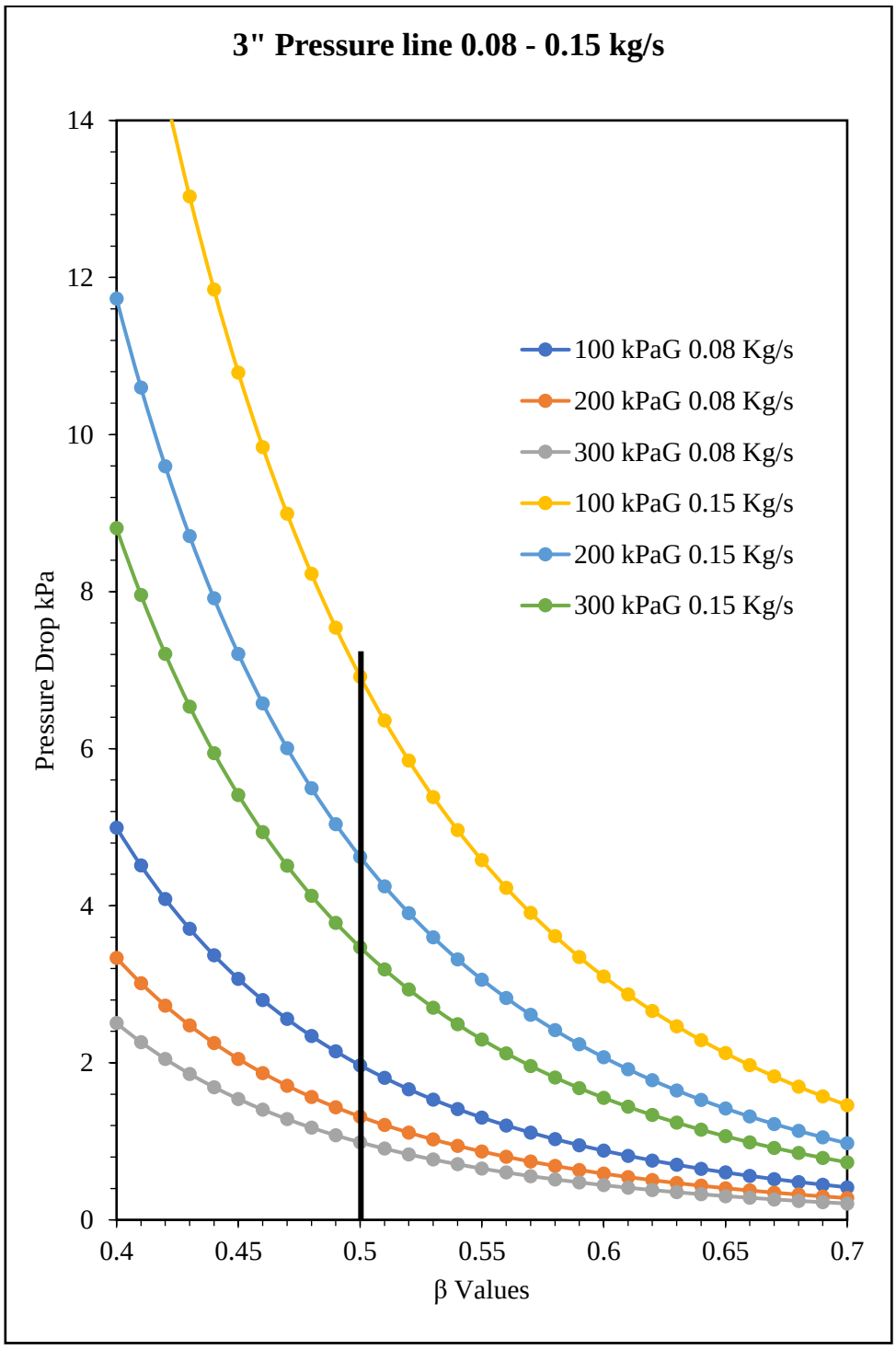

iii. 0.15 to 0.20 kg/s: β=0.60

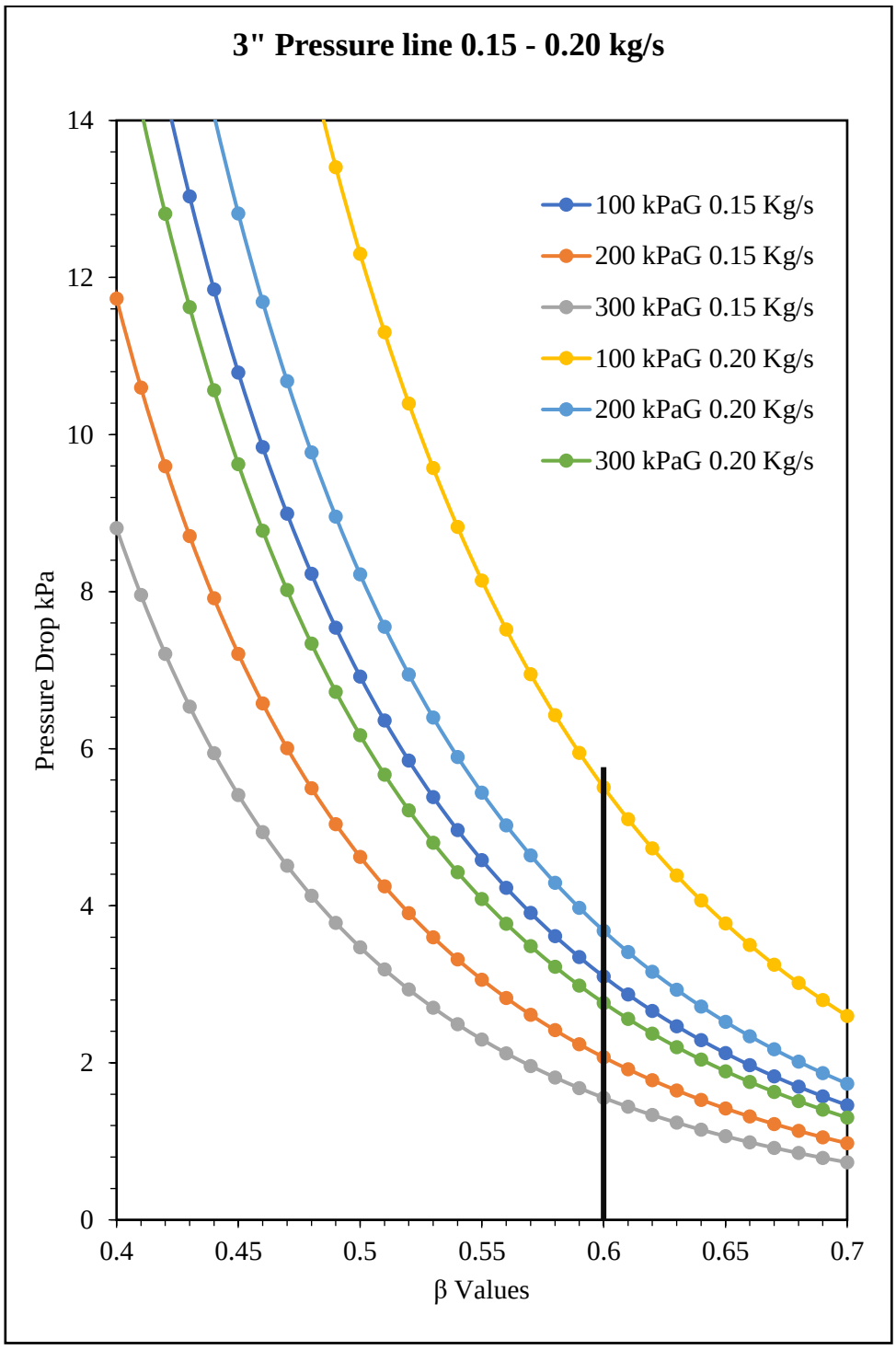

II. Conveying air line for pressure system (2 Inch)

i. 0.04 to 0.06 kg/s; β=0.40

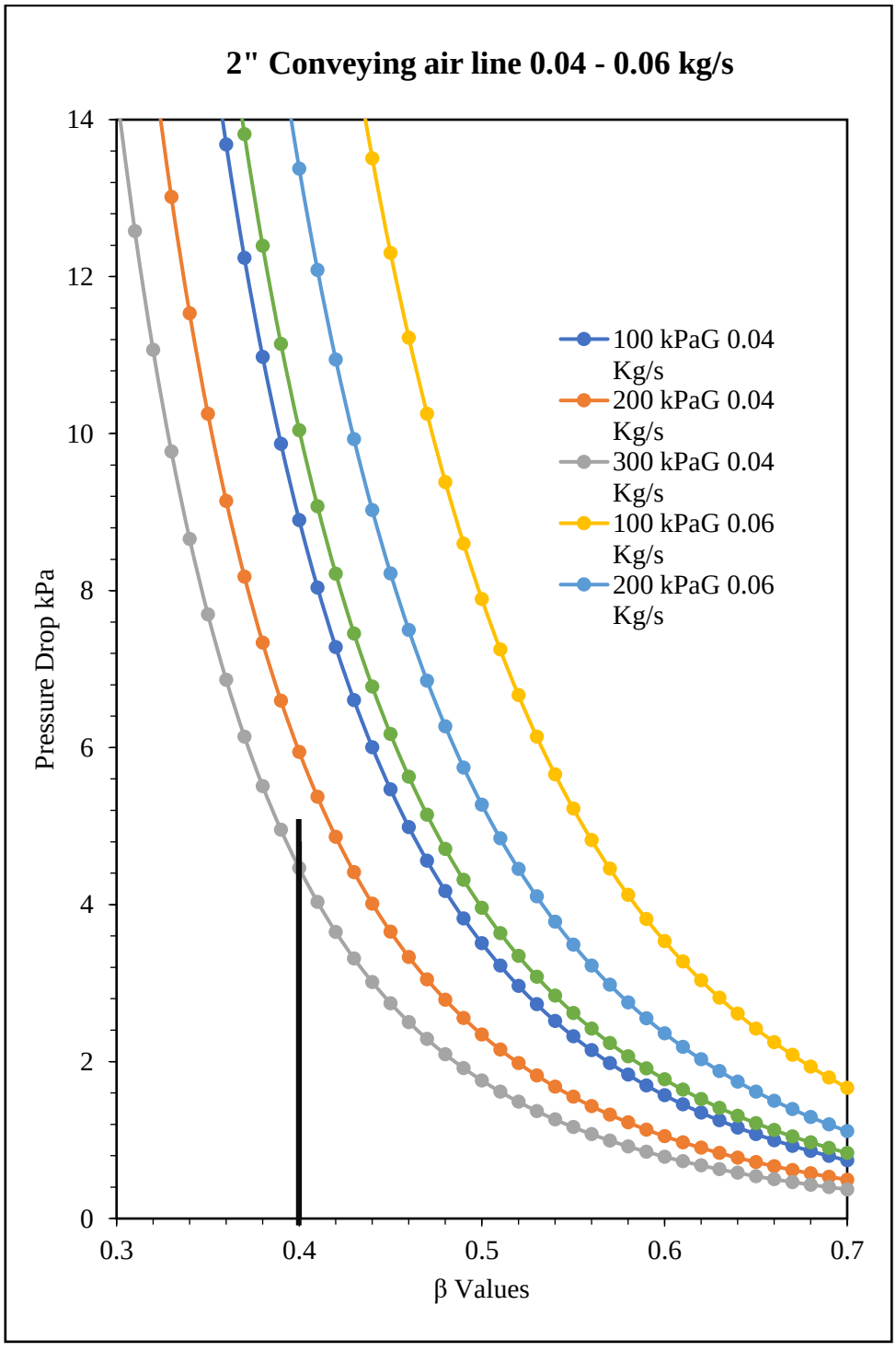

ii. 0.06 to 0.12 kg/s; β=0.55

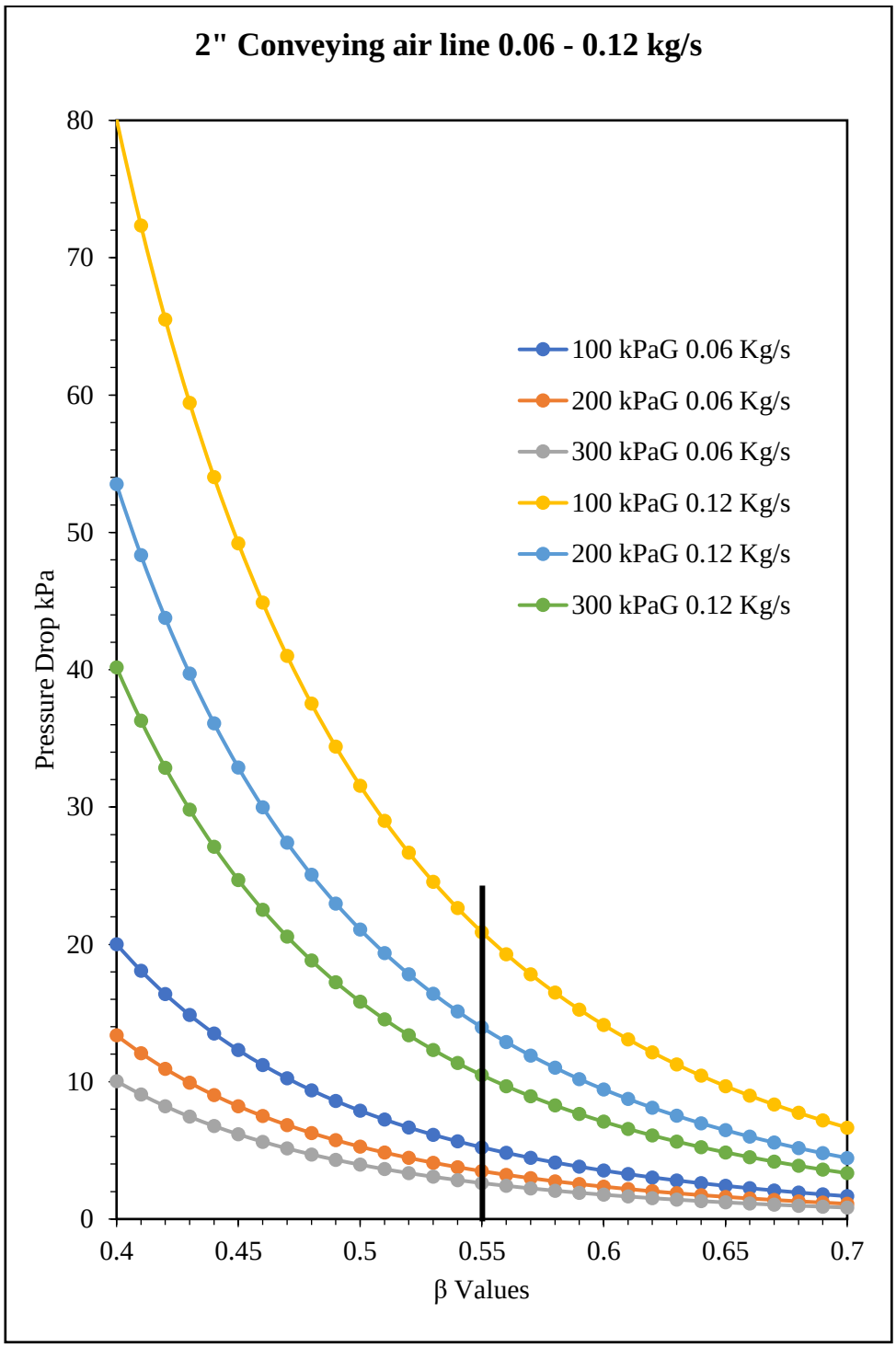

iii. 0.12 to 0.20 kg/s; β=0.70

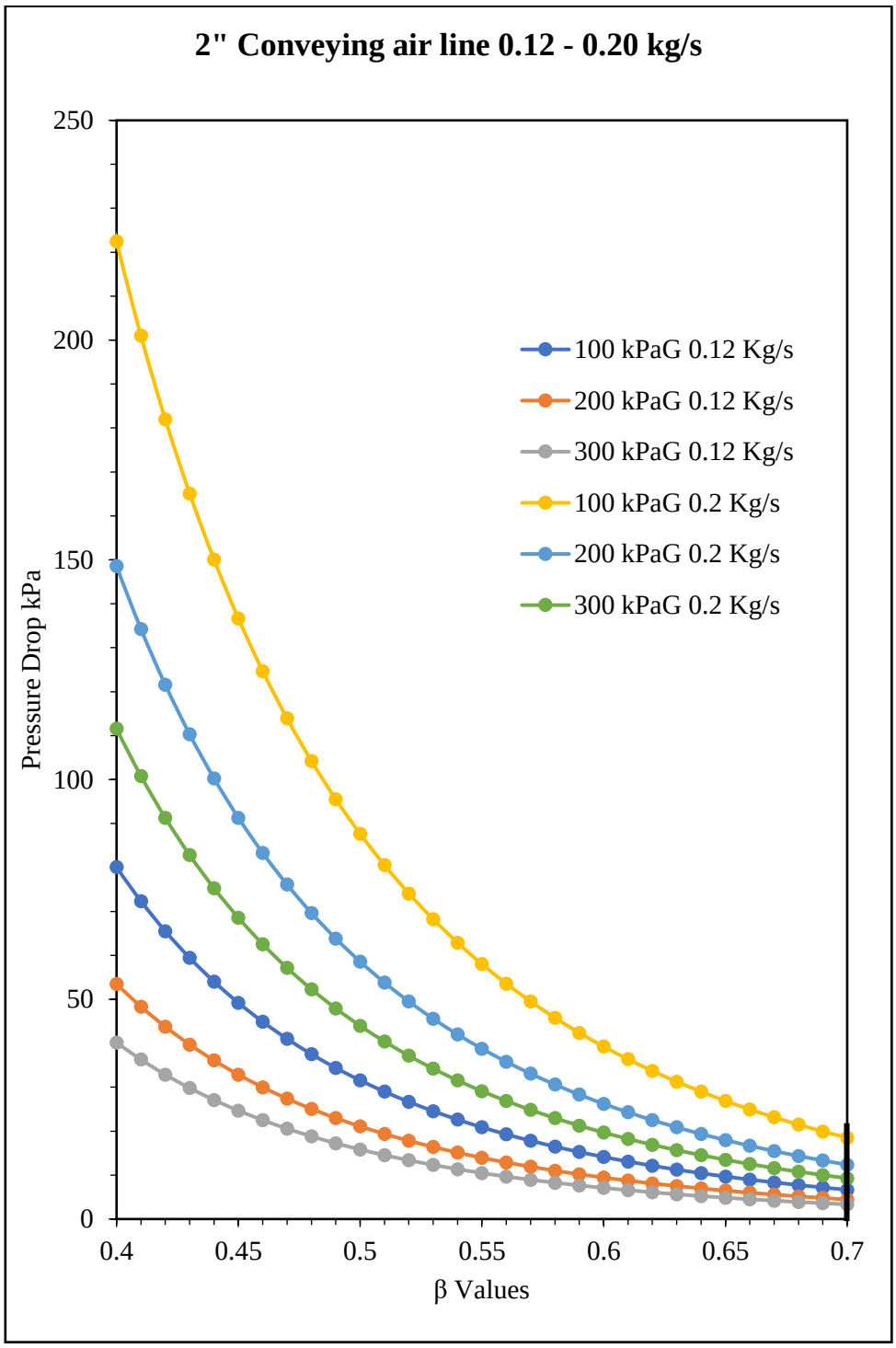

III. Fluidizing air (2 Inch)

i. 0.02 to 0.04 kg/s; β=0.40

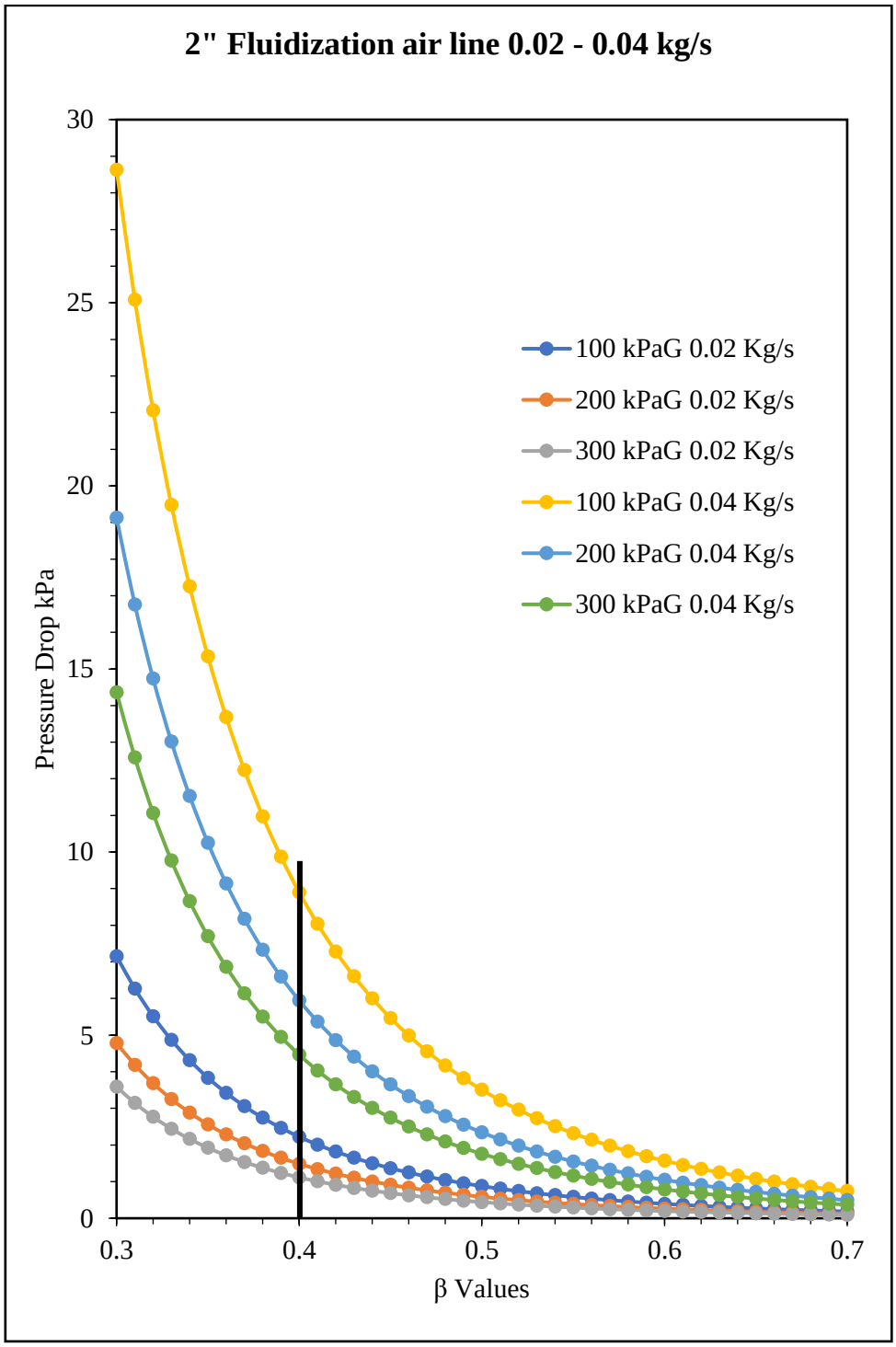

ii. 0.04 to 0.06 kg/s; β=0.45

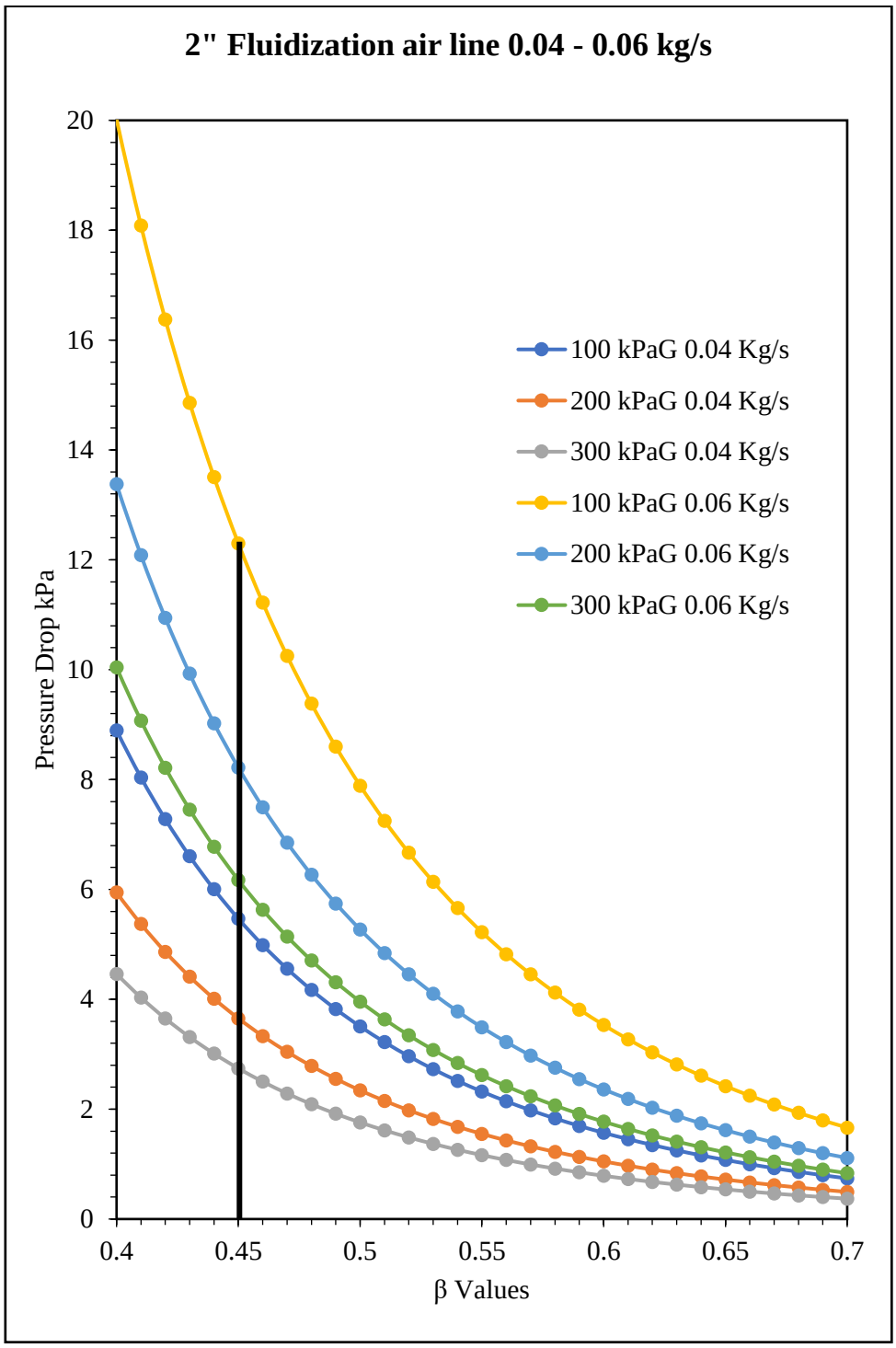

iii. 0.06 to 0.08 kg/s; β=0.50

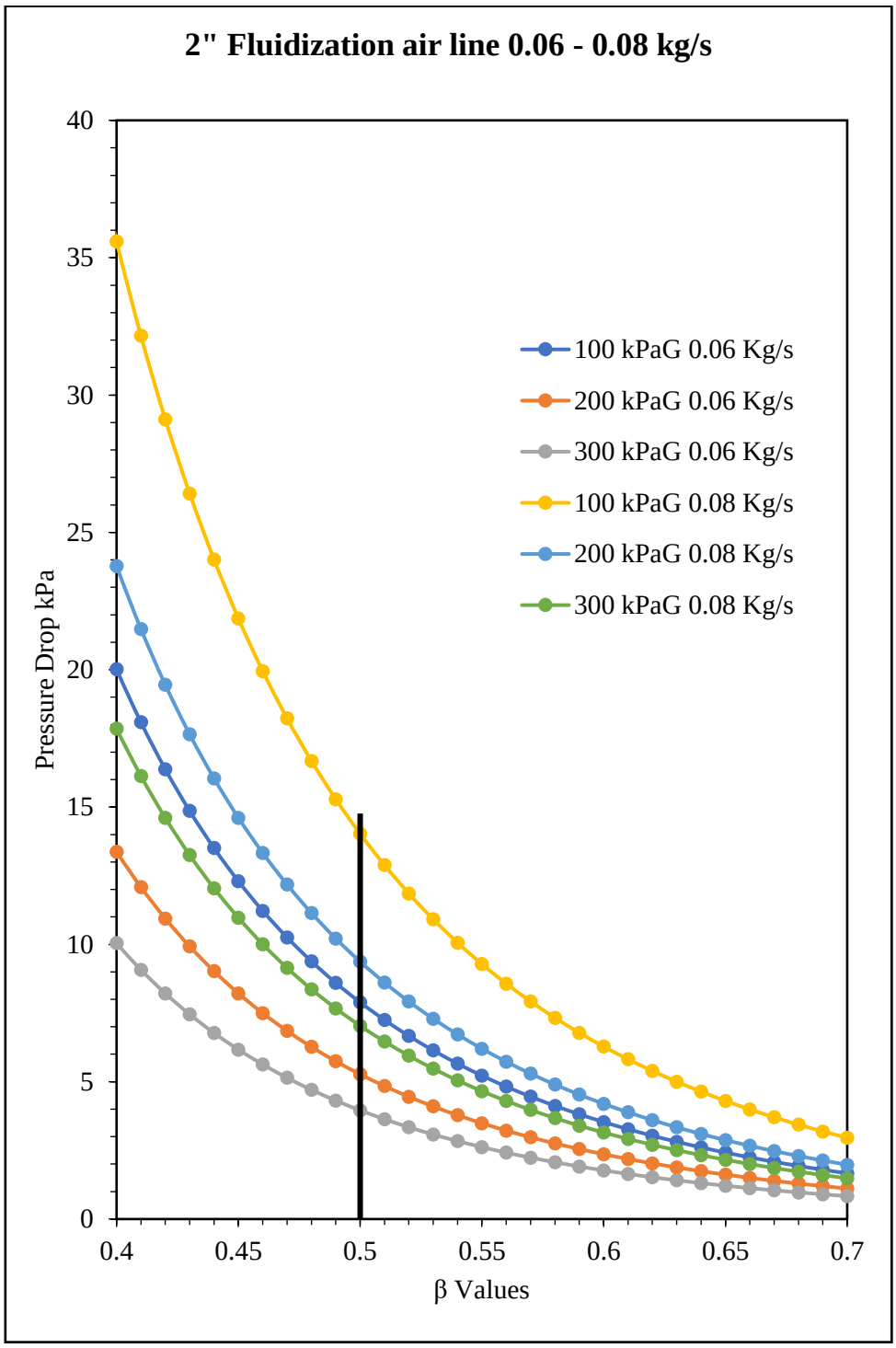

IV. Top/side air (2 Inch)

i. 0.04 to 0.06 kg/s; β=0.40

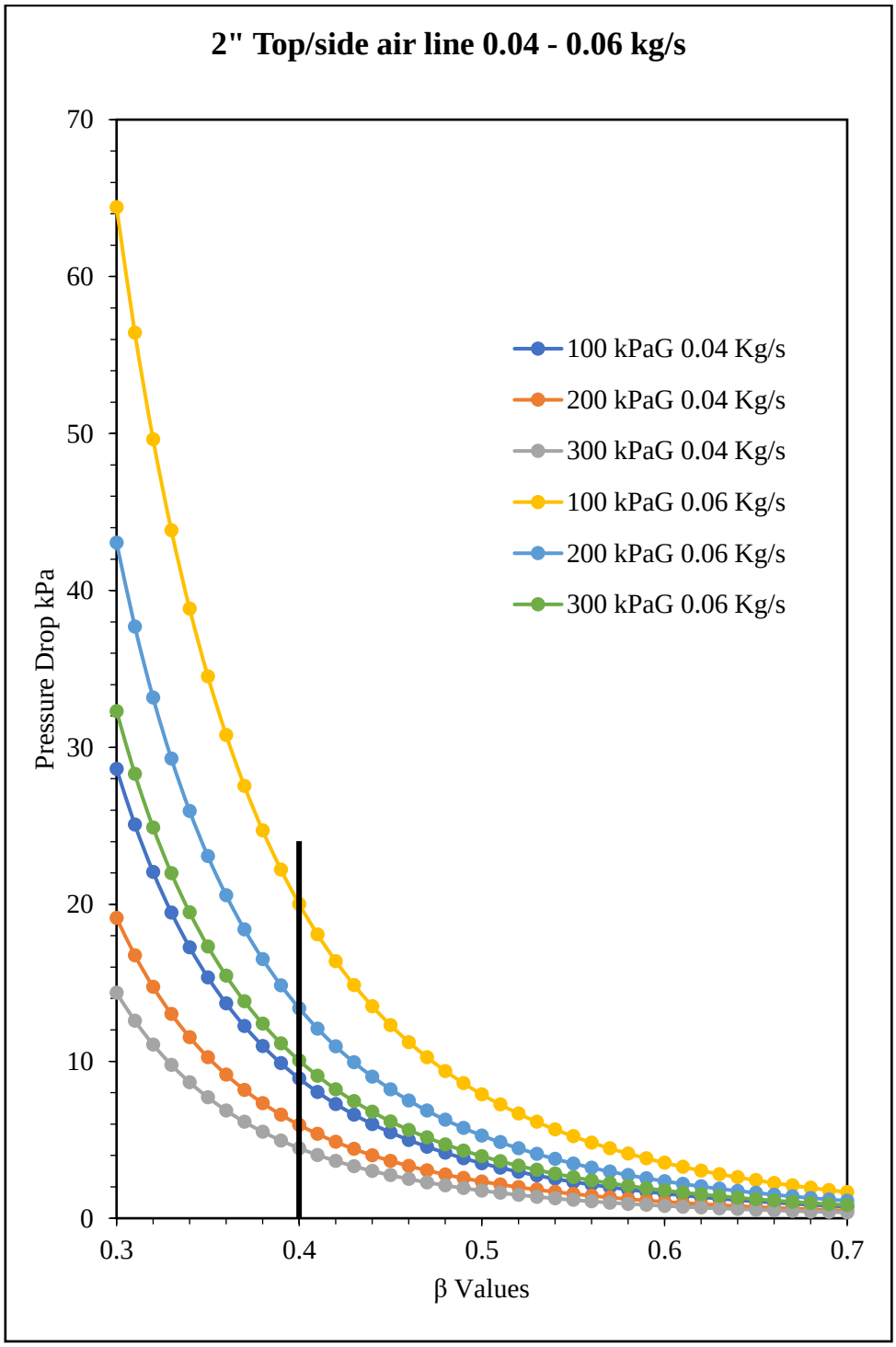

ii. 0.06 to 0.12 kg/s; β=0.55

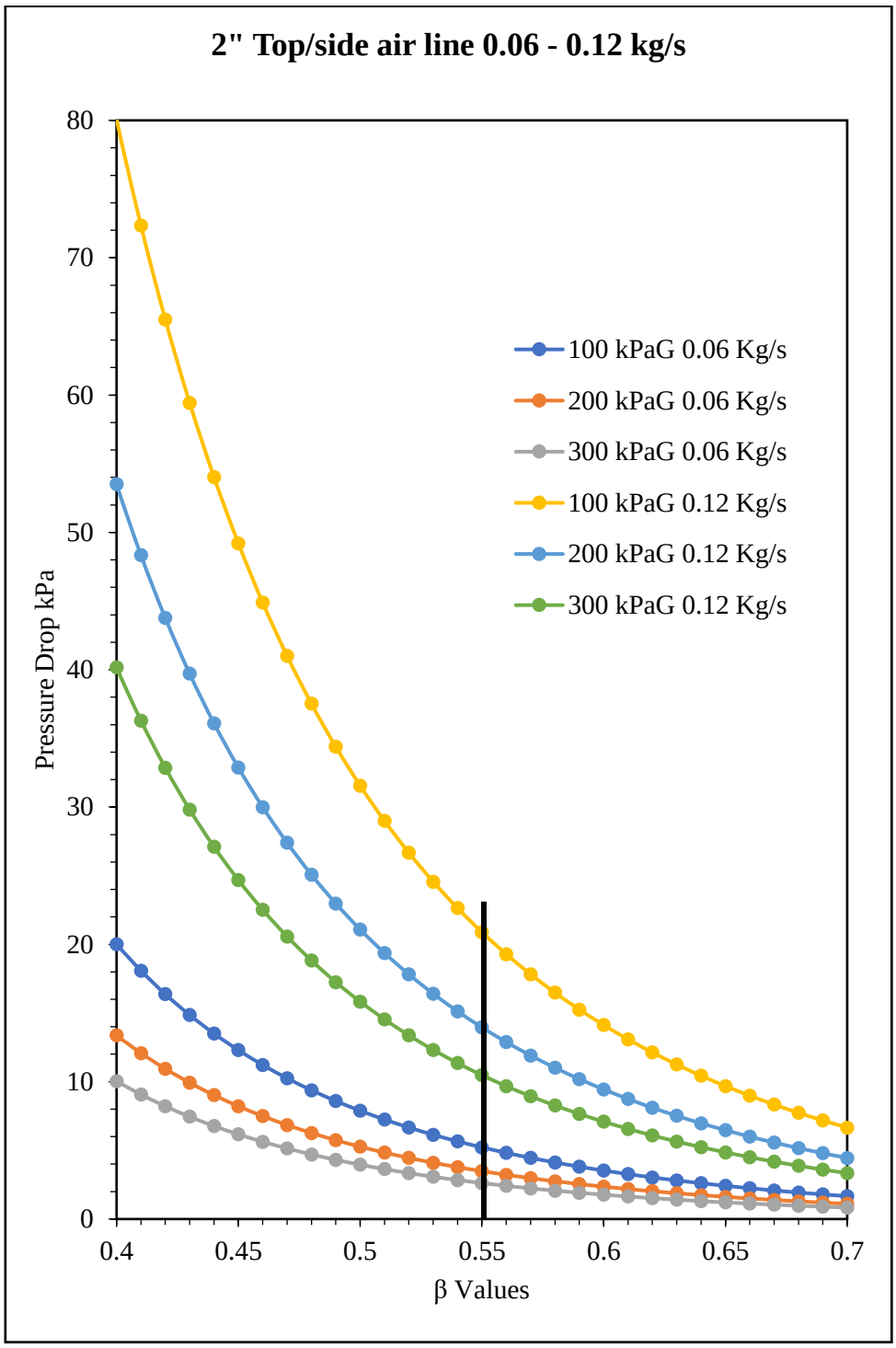

iii. 0.12 to 0.20 kg/s; β=0.70

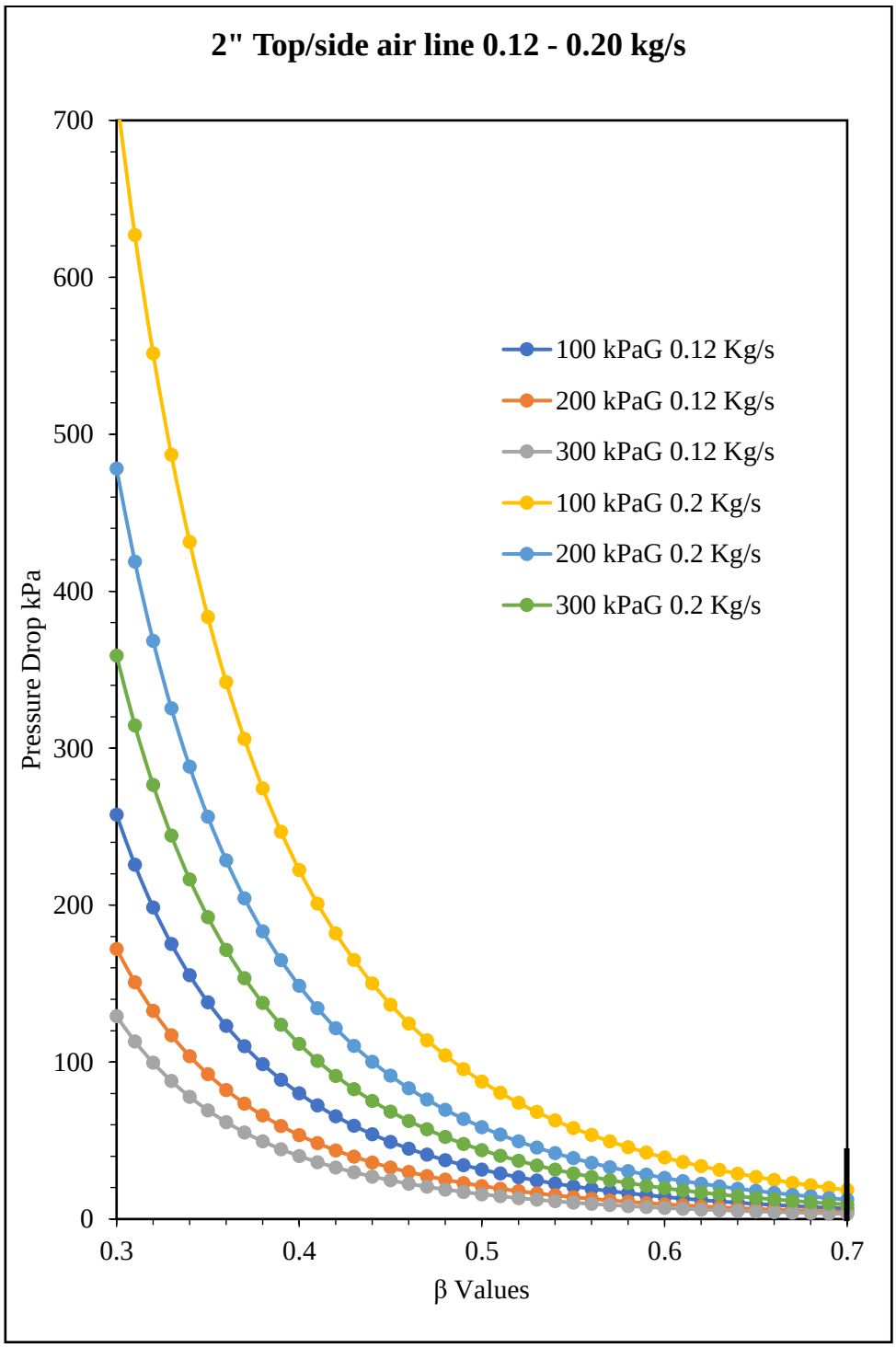

V. Conveying air line for vacuum system (3 Inch)

i. 0.04 to 0.06 kg/s; β=0.40

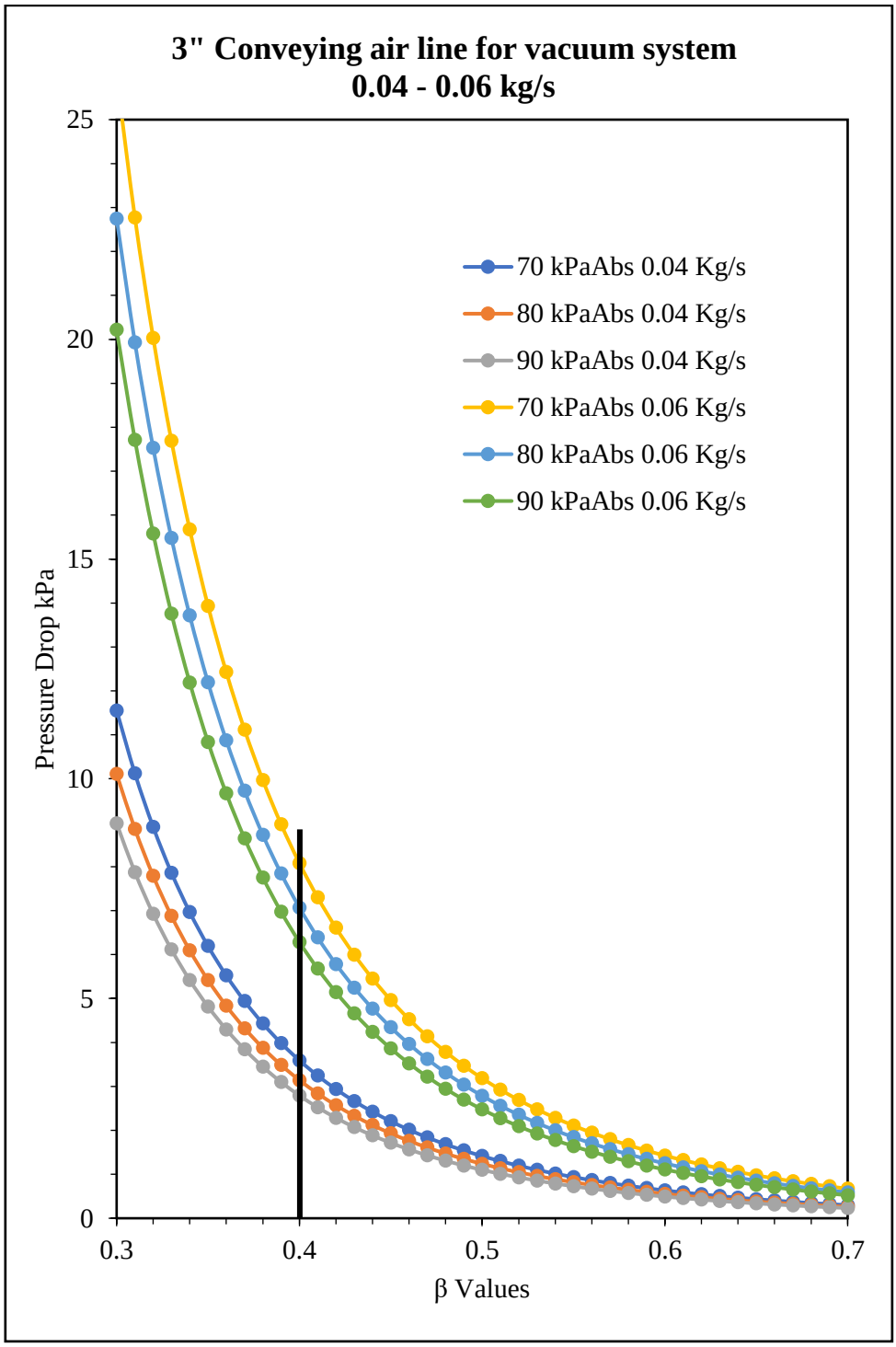

ii. 0.06 to 0.12 kg/s; β=0.55

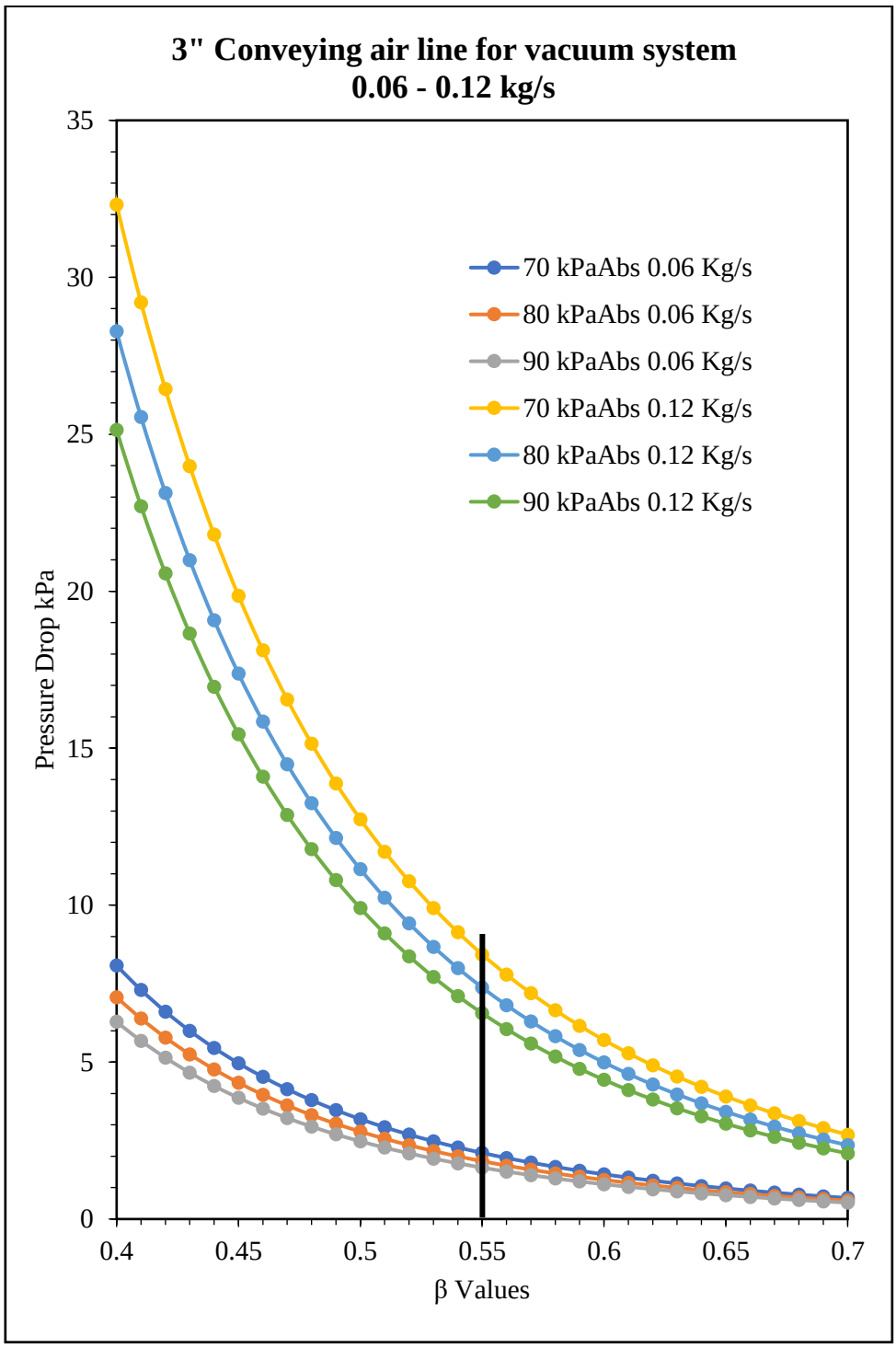

iii. 0.12 to 0.20 kg/s; β=0.70

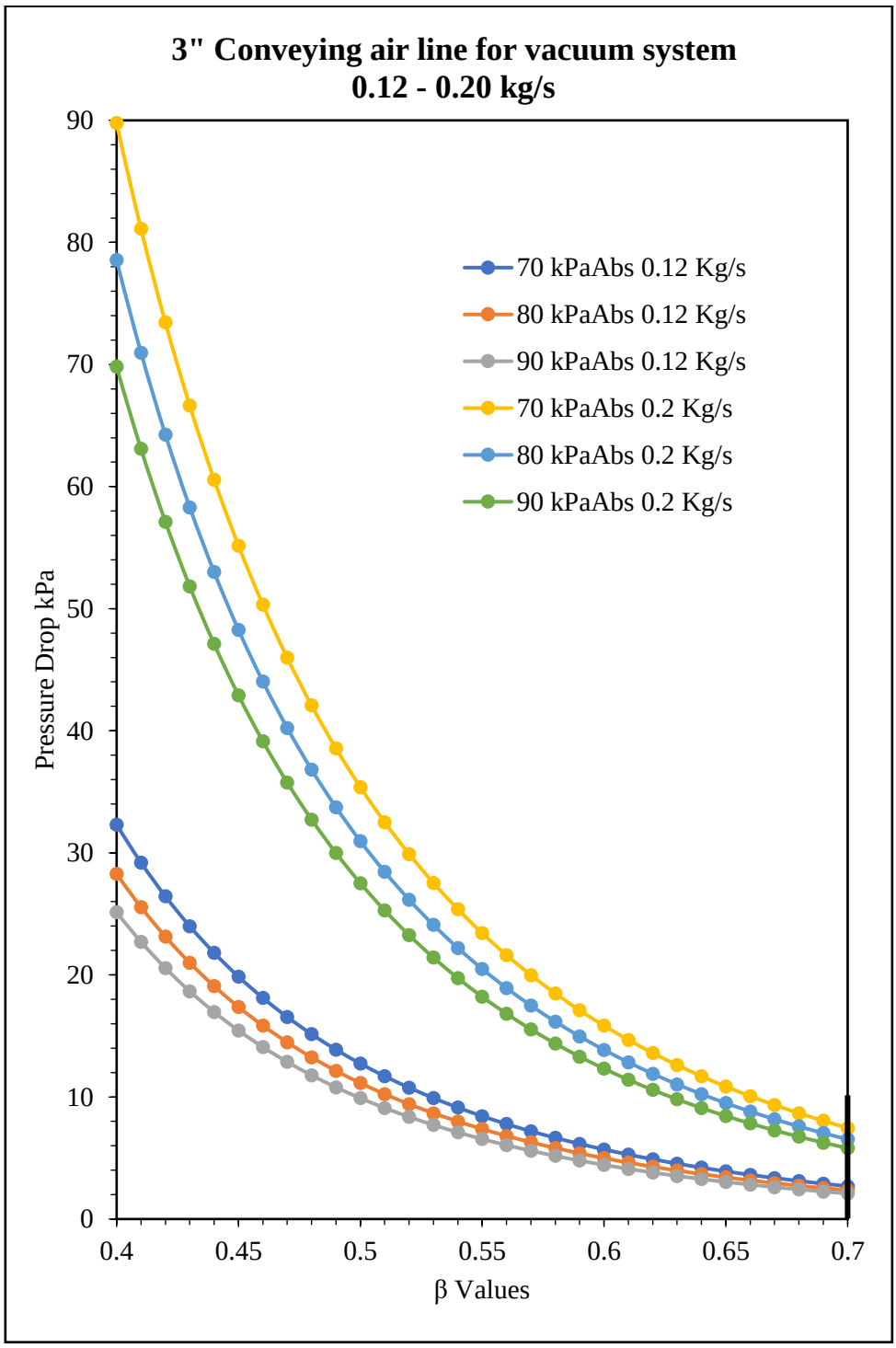

APPENDIX II

Sensitivity Analysis Data:

Poisson's Ratio	ν	0.25		0.25		0.25	
Particle Density	ρ_p(kg/m^3)	2500		2500		2500	
Shear Modulus	G (Pa)	1.00E+08		1.00E+08		1.00E+08	
Youngs's Modulus	E (Pa)	2.50E+08		2.50E+08		2.50E+08	
Coefficient of Restitution	e	0.5		0.5		0.5	
Coefficient of Static Frction	μ_s	0.5		0.5		0.5	
Coefficient of Rolling Friction	μ_r	0.01		0.01		0.01	
Dia	d (mm)	2		1.75		1.5	
		σ_n	ρ	σ_n	ρ	σ_n	ρ
		0.0858	1317.689	0.0844	1348.389	0.089	1379.103
		0.2613	1322.789	0.2488	1351.713	0.2702	1382.023
		0.4985	1325.588	0.4315	1353.144	0.4259	1383.491
		0.9949	1328.398	0.9881	1355.053	0.9089	1385.448
		2.173	1331.691	2.1592	1357.929	2.2243	1387.906
		4.8506	1341.663	4.9228	1367.601	4.916	1395.819
Poisson's Ratio	ν	0.25		0.25		0.25	
Particle Density	ρ_p(kg/m^3)	2500		2500		2500	
Shear Modulus	G (Pa)	1.00E+07		1.50E+07		1.25E+07	
Youngs's Modulus	E (Pa)	2.50E+07		3.75E+07		3.13E+07	
Coefficient of Restitution	e	0.5		0.5		0.5	
Coefficient of Static Frction	μ_s	0.5		0.5		0.5	
Coefficient of Rolling Friction	μ_r	0.01		0.01		0.01	
Dia	d (mm)	2		2		2	
		σ_n	ρ	σ_n	ρ	σ_n	ρ
		0.0867	1324.579	0.0855	1321.793	0.087	1322.984
		0.2861	1333.888	0.2867	1330.166	0.2844	1328.577
		0.5282	1353.852	0.5113	1335.802	0.5238	1336.577
		1.0625	1380.109	1.0562	1363.218	1.0498	1372.492
		2.2418	1407.093	2.2523	1395.811	2.2575	1406.107
		4.8302	1433.478	4.9135	1422.966	4.8923	1429.752
Poisson's Ratio	ν	0.125		0.25		0.375	
Particle Density	ρ_p(kg/m^3)	2500		2500		2500	
Shear Modulus	G (Pa)	1.00E+08		1.00E+08		1.00E+08	
Youngs's Modulus	E (Pa)	2.25E+08		2.50E+08		2.75E+08	
Coefficient of Restitution	e	0.5		0.5		0.5	
Coefficient of Static Frction	μ_s	0.5		0.5		0.5	
Coefficient of Rolling Friction	μ_r	0.01		0.01		0.01	
Dia	d (mm)	2		2		2	

		σ_n	ρ	σ_n	ρ	σ_n	ρ
		0.0879	1316.713	0.0858	1317.689	0.0787	1316.39
		0.261	1320.415	0.2613	1322.789	0.2729	1319.622
		0.432	1323.201	0.4985	1325.588	0.4436	1322.408
		1.0068	1326.004	0.9949	1328.398	0.9646	1327.075
		2.08	1328.814	2.173	1331.691	2.146	1330.827
		4.885	1342.085	4.8506	1341.663	4.7258	1337.924
Poisson's Ratio	ν	0.25		0.25		0.25	
Particle Density	ρ_p(kg/m^3)	2500		2500		2500	
Shear Modulus	G (Pa)	1.00E+08		1.00E+08		1.00E+08	
Youngs's Modulus	E (Pa)	2.50E+08		2.50E+08		2.50E+08	
Coefficient of Restitution	e	0.25		0.5		0.75	
Coefficient of Static Frction	μ_s	0.5		0.5		0.5	
Coefficient of Rolling Friction	μ_r	0.01		0.01		0.01	
Dia	d (mm)	2		2		2	
		σ_n	ρ	σ_n	ρ	σ_n	ρ
		0.0909	1314.802	0.0858	1317.689	0.0844	1332.369
		0.2824	1319.42	0.2613	1322.789	0.2816	1337.988
		0.5083	1324.071	0.4985	1325.588	0.4569	1339.401
		1.0603	1328.753	0.9949	1328.398	0.9717	1341.287
		2.2547	1346.353	2.173	1331.691	1.9073	1343.653
		4.7962	1384.777	4.8506	1341.663	4.911	1346.979
Poisson's Ratio	ν	0.25		0.25		0.25	
Particle Density	ρ_p(kg/m^3)	2500		2500		2500	
Shear Modulus	G (Pa)	1.00E+08		1.00E+08		1.00E+08	
Youngs's Modulus	E (Pa)	2.50E+08		2.50E+08		2.50E+08	
Coefficient of Restitution	e	0.5		0.5		0.5	
Coefficient of Static Frction	μ_s	0.25		0.5		0.75	
Coefficient of Rolling Friction	μ_r	0.01		0.01		0.01	
Dia	d (mm)	2		2		2	
		σ_n	ρ	σ_n	ρ	σ_n	ρ
		0.0882	1339.769	0.0858	1317.689	0.0848	1307.882
		0.2349	1345.425	0.2613	1322.789	0.2807	1313.396
		0.419	1346.848	0.4985	1325.588	0.4403	1314.78
		1.0606	1349.224	0.9949	1328.398	0.9714	1317.56
		2.2259	1352.565	2.173	1331.691	2.2304	1320.351
		4.8868	1364.62	4.8506	1341.663	4.8556	1333.046
Poisson's Ratio	ν	0.25		0.25		0.25	
Particle Density	ρ_p(kg/m^3)	2500		2500		2500	
Shear Modulus	G (Pa)	1.00E+08		1.00E+08		1.00E+08	
Youngs's Modulus	E (Pa)	2.50E+08		2.50E+08		2.50E+08	
Coefficient of Restitution	e	0.5		0.5		0.5	

Coefficient of Static Frction	μ_s	0.5		0.5		0.5	
Coefficient of Rolling Friction	μ_r	0.01		0.02		0.03	
Dia	d (mm)	2		2		2	
		σ_n	ρ	σ_n	ρ	σ_n	ρ
		0.0858	1317.689	0.0916	1310.498	0.079	1304.719
		0.2613	1322.789	0.2442	1312.794	0.2667	1309.304
		0.4985	1325.588	0.4837	1315.1	0.498	1312.991
		0.9949	1328.398	1.0055	1318.341	0.9692	1315.772
		2.173	1331.691	2.1843	1322.059	2.1214	1321.367
		4.8506	1341.663	4.9205	1333.344	4.8828	1340.822
Poisson's Ratio	ν	0.25		0.25		0.25	
Particle Density	ρ_p(kg/m^3)	2000		2500		3000	
Shear Modulus	G (Pa)	1.00E+08		1.00E+08		1.00E+08	
Youngs's Modulus	E (Pa)	2.50E+08		2.50E+08		2.50E+08	
Coefficient of Restitution	e	0.5		0.5		0.5	
Coefficient of Static Frction	μ_s	0.5		0.5		0.5	
Coefficient of Rolling Friction	μ_r	0.01		0.01		0.01	
Dia	d (mm)	2		2		2	
		σ_n	ρ	σ_n	ρ	σ_n	ρ
		0.0854	1058.79	0.0858	1317.689	0.0873	1582.139
		0.271	1062.135	0.2613	1322.789	0.26	1584.915
		0.4955	1064.001	0.4985	1325.588	0.4967	1589.378
		0.8946	1065.874	0.9949	1328.398	0.9056	1592.18
		2.2291	1068.129	2.173	1331.691	2.2105	1597.808
		4.8309	1076.861	4.8506	1341.663	4.9196	1609.184

Spherical Particle Calibration Data:

		APH Trial 1		**APH Trial 2**		**APH Trial 3**	
Poisson's Ratio	ν	0.25		0.25		0.25	
Particle Density	ρp(kg/m3)	800		1600		1600	
Shear Modulus	G (Pa)	1.00E+08		1.00E+08		1.00E+07	
Youngs's Modulus	E (Pa)	2.50E+08		2.50E+08		2.50E+07	
Coefficient of Restitution	e	0.5		0.5		0.5	
Coefficient of Static Frction	μs	0.5		0.5		0.5	
Coefficient of Rolling Friction	μr	0.01		0.01		0.01	
Dia	d (mm)	2		2		2	
		σn	ρ	σn	ρ	σn	ρ
		0.0914	422.078	0.0922	843.7276	0.0875	836.4815
		0.2377	423.7136	0.2403	846.1054	0.2878	840.325
		0.4944	424.0119	0.4	847.9007	0.5191	843.6024
		0.8489	424.3106	0.8926	849.0997	1.0641	843.302
		1.9393	425.0601	2.2498	851.5079	1.9685	845.0983
		4.9092	429.915	4.8051	861.2756	4.9278	854.193

		APH Trial 4		APH Trial 5		APH Trial 6	
Poisson's Ratio	ν	0.25		0.25		0.25	
Particle Density	ρp(kg/m3)	1600		1600		1600	
Shear Modulus	G (Pa)	1.00E+07		1.00E+07		1.00E+07	
Youngs's Modulus	E (Pa)	2.50E+07		2.50E+07		2.50E+07	
Coefficient of Restitution	e	0.5		0.5		0.5	
Coefficient of Static Frction	μs	0.25		0.2		0.15	
Coefficient of Rolling Friction	μr	0.01		0.01		0.01	
Dia	d (mm)	2		2		2	
		σn	ρ	σn	ρ	σn	ρ
		0.0941	865.1902	0.0934	865.8934	0.0929	869.4559
		0.2831	870.4317	0.2853	872.0713	0.2817	876.98
		0.5216	877.6145	0.5177	881.5036	0.511	882.3875
		1.0359	888.7695	1.0643	890.802	1.0423	891.7532
		2.1959	907.5223	2.2202	906.6126	2.2329	905.3264
		4.8823	923.2101	4.909	922.2723	4.8844	923.1093

		APH Trial 7		APH Trial 8		APH Trial 9	
Poisson's Ratio	ν	0.25		0.25		0.25	
Particle Density	ρp(kg/m3)	1600		1600		1600	
Shear Modulus	G (Pa)	1.00E+07		1.00E+07		1.50E+06	
Youngs's Modulus	E (Pa)	2.50E+07		2.50E+07		3.75E+06	
Coefficient of Restitution	e	0.5		0.25		0.25	
Coefficient of Static Frction	μs	0.25		0.25		0.25	
Coefficient of Rolling Friction	μr	0.001		0.001		0.001	
Dia	d (mm)	2		2		2	
		σn	ρ	σn	ρ	σn	ρ
		0.0948	864.0792	0.0898	875.7605	0.0937	898.8339
		0.2706	869.6313	0.2791	887.4775	0.2867	912.7982
		0.5035	873.9985	0.523	894.5842	0.5199	920.2742
		1.0452	888.0009	1.0502	904.453	1.0505	931.3622
		2.2392	906.4454	2.2385	916.5682	2.2156	949.9241
		4.8311	923.8848	4.9295	929.3478	4.8655	979.5011

		APH Trial 10		APH Trial 11		APH Trial 12	
Poisson's Ratio	ν	0.25		0.25		0.125	
Particle Density	ρp(kg/m3)	1600		1600		1600	
Shear Modulus	G (Pa)	1.75E+06		1.75E+06		1.75E+06	
Youngs's Modulus	E (Pa)	4.38E+06		4.38E+06		3.94E+06	
Coefficient of Restitution	e	0.15		0.2		0.2	
Coefficient of Static Frction	μs	0.25		0.25		0.25	
Coefficient of Rolling Friction	μr	0.001		0.001		0.001	
Dia	d (mm)	2		2		2	
		σn	ρ	σn	ρ	σn	ρ
		0.0943	900.4011	0.0906	900.3872	0.0914	897.3762
		0.2782	909.68	0.2819	910.309	0.2762	911.1787
		0.5254	918.4595	0.5122	917.0424	0.5189	923.3324
		1.0111	928.7906	1.0523	928.008	1.0646	935.0984

		2.2367	947.2277	2.2222	945.2902	2.1627	954.3723
		4.7774	962.6311	4.8743	965.4238	4.7801	977.8304

		APH Trial 13	APH Trial 14	APH Trial 15
Poisson's Ratio	ν	0.1	0.125	0.125
Particle Density	ρp(kg/m3)	1600	1600	1600
Shear Modulus	G (Pa)	1.75E+06	1.75E+06	1.75E+06
Youngs's Modulus	E (Pa)	3.94E+06	3.94E+06	3.94E+06
Coefficient of Restitution	e	0.2	0.2	0.2
Coefficient of Static Frction	μs	0.25	0.25	0.25
Coefficient of Rolling Friction	μr	0.001	0.1	0.5
Dia	d (mm)	2	2	2

σn	ρ	σn	ρ	σn	ρ
0.0946	900.6258	0.0925	899.2418	0.0922	899.696
0.2849	913.5176	0.2798	909.588	0.2874	911.0432
0.5199	921.6234	0.5242	918.0979	0.5195	919.2166
1.0562	934.0481	1.0611	928.1563	1.051	931.0351
2.2456	953.6466	2.2589	948.1847	2.1229	950.0387
4.7739	972.1475	4.8997	965.2515	4.8716	979.7632

Tetrahedral Particle Calibration Data:

		APHT Trial 1	APHT Trial 2	APHT Trial 3
Poisson's Ratio	ν	0.25	0.25	0.25
Particle Density	ρp(kg/m3)	2500	2500	2500
Shear Modulus	G (Pa)	1.00E+08	1.00E+07	1.50E+06
Youngs's Modulus	E (Pa)	2.50E+08	2.50E+07	3.75E+06
Coefficient of Restitution	e	0.5	0.5	0.5
Coefficient of Static Frction	μs	0.5	0.5	0.5
Coefficient of Rolling Friction	μr	0.01	0.01	0.01

σn	ρ	σn	ρ	σn	ρ
0.0948	875.2527	0.0883	868.4968	0.0939	890.3185
0.2837	878.0818	0.2872	874.3582	0.2845	900.5592
0.4577	879.661	0.5197	879.6627	0.5161	919.7074
1.038	881.563	1.0593	888.5392	1.064	1030.061
2.1327	883.7919	2.2579	898.8994	2.2529	1126.479
4.7495	887.9617	4.6001	931.0544	4.894	1182.358

		APHT Trial 4	APHT Trial 5	APHT Trial 6
Poisson's Ratio	ν	0.25	0.25	0.25
Particle Density	ρp(kg/m3)	2500	2500	2500
Shear Modulus	G (Pa)	1.75E+06	5.00E+06	5.00E+06
Youngs's Modulus	E (Pa)	4.38E+06	1.25E+07	1.25E+07
Coefficient of Restitution	e	0.5	0.5	0.5
Coefficient of Static Frction	μs	0.5	0.5	0.5
Coefficient of Rolling Friction	μr	0.01	0.01	0.02

σn	ρ	σn	ρ	σn	ρ
0.0924	885.2818	0.0941	882.0649	0.0902	869.967
0.286	897.6561	0.2762	887.1063	0.2832	879.5337
0.5146	917.0214	0.5263	892.199	0.5246	885.8093
1.0635	990.5867	1.0596	902.2316	1.0451	892.175
2.2541	1105.102	2.261	938.2357	2.2616	953.6515
4.927	1160.547	4.8803	1081.521	4.4252	1082.114

		APHT Trial 7	**APHT Trial 8**	**APHT Trial 9**
Poisson's Ratio	ν	0.25	0.25	0.25
Particle Density	ρp(kg/m3)	2500	2500	2500
Shear Modulus	G (Pa)	7.50E+06	2.50E+06	2.50E+06
Youngs's Modulus	E (Pa)	1.88E+07	6.25E+06	6.25E+06
Coefficient of Restitution	e	0.5	0.5	0.6
Coefficient of Static Frction	μs	0.5	0.5	0.5
Coefficient of Rolling Friction	μr	0.01	0.01	0.01

σn	ρ	σn	ρ	σn	ρ
0.0941	880.9406	0.094	873.8549	0.0928	875.073
0.2762	888.4598	0.2869	886.9847	0.2877	885.6271
0.5019	893.2235	0.5245	897.5668	0.5102	892.5871
1.0338	901.5996	1.0567	926.665	1.061	903.8796
2.2488	920.4952	2.2612	1067.535	2.2519	948.6909
4.9212	1030.054	4.9184	1138.947	4.9267	1117.346

		APHT Trial 10	**APHT Trial 11**	**APHT Trial 12**
Poisson's Ratio	ν	0.25	0.25	0.25
Particle Density	ρp(kg/m3)	2500	2500	2500
Shear Modulus	G (Pa)	2.50E+06	2.50E+06	2.00E+06
Youngs's Modulus	E (Pa)	6.25E+06	6.25E+06	5.00E+06
Coefficient of Restitution	e	0.8	0.8	0.8
Coefficient of Static Frction	μs	0.5	0.6	0.6
Coefficient of Rolling Friction	μr	0.01	0.01	0.01

σn	ρ	σn	ρ	σn	ρ
0.0934	902.0842	0.0918	883.9848	0.0904	883.2901
0.2876	909.8642	0.2793	889.9289	0.2873	889.5364
0.5188	913.8014	0.5235	894.6734	0.5255	895.5475
1.0464	921.1064	1.0395	902.3694	1.0382	903.2523
2.2442	931.2506	2.2087	913.8269	2.2469	914.7197
4.9255	956.1285	4.9279	941.7847	4.9134	938.8595

		APHT Trial 13	**APHT Trial 14**	**APHT Trial 15**
Poisson's Ratio	ν	0.25	0.25	0.125
Particle Density	ρp(kg/m3)	2500	2500	2500
Shear Modulus	G (Pa)	1.50E+06	1.00E+06	1.00E+06
Youngs's Modulus	E (Pa)	3.75E+06	2.50E+06	2.50E+06
Coefficient of Restitution	e	0.8	0.8	0.8

Coefficient of Static Frction	μs	0.6	0.6	0.6
Coefficient of Rolling Friction	μr	0.01	0.01	0.01

σn	ρ	σn	ρ	σn	ρ
0.0923	883.0281	0.0909	884.465	0.094	889.5723
0.2814	892.8189	0.2862	894.5908	0.2812	896.8471
0.5158	900.2188	0.5205	903.6365	0.5171	903.2701
1.0564	911.3736	1.0612	915.5262	1.0534	917.0431
2.2417	927.2405	2.2555	948.0265	2.2596	945.8336
4.9193	981.214	4.8931	1163.375	4.8907	1175.41

		APHT Trial 16	**APHT Trial 17**
Poisson's Ratio	ν	0.375	0.25
Particle Density	ρp(kg/m3)	2500	2500
Shear Modulus	G (Pa)	1.00E+06	1499000
Youngs's Modulus	E (Pa)	2.50E+06	2500000
Coefficient of Restitution	e	0.8	0.8
Coefficient of Static Frction	μs	0.6	0.6
Coefficient of Rolling Friction	μr	0.01	0.01

σn	ρ	σn	ρ
0.090329	1412.248	0.0917	1009.252
0.2526	1417.382	0.2867	1020.378
0.487066	1421.072	0.5171	1026.582
1.059505	1424.782	1.057	1035.463
2.23652	1430.008	2.2318	1052.904
4.890478	1444.387	4.8944	1081.358

Khusro's M.Tech. Thesis

ORIGINALITY REPORT

11%	4%	7%	8%
SIMILARITY INDEX	INTERNET SOURCES	PUBLICATIONS	STUDENT PAPERS

PRIMARY SOURCES

1	Submitted to University of Newcastle Student Paper	1%
2	Submitted to University of Sheffield Student Paper	1%
3	www2.hcmuaf.edu.vn Internet Source	1%
4	tailieu.vn Internet Source	<1%
5	Submitted to University of Wollongong Student Paper	<1%
6	www.fxsolver.com Internet Source	<1%
7	C. R. Woodcock, J. S. Mason. "Bulk Solids Handling", Springer Nature, 1988 Publication	<1%
8	"Powders and Bulk Solids", Springer Nature, 2007 Publication	<1%

9	www.freepatentsonline.com Internet Source	<1%
10	C.K. Kanakabandi, T.K. Goswami. "Determination of properties of black pepper to use in discrete element modeling", Journal of Food Engineering, 2019 Publication	<1%
11	Submitted to University of Edinburgh Student Paper	<1%
12	www.martin-eng.pe Internet Source	<1%
13	Jauhari Ashish, Gharde Swaroop, Kandasubramanian Balasubramanian. "Effect of Ammonium Perchlorate Particle Size on Flow, Ballistic, and Mechanical Properties of Composite Propellant", Elsevier BV, 2019 Publication	<1%
14	Submitted to University of Bahrain Student Paper	<1%
15	Submitted to Edith Cowan University Student Paper	<1%
16	archive.org Internet Source	<1%
17	B.G.M. van Wachem, A.E. Almstedt. "Methods for multiphase computational fluid dynamics",	<1%

	Chemical Engineering Journal, 2003 Publication	
18	Encyclopedia of Earth Sciences Series, 2011. Publication	<1%
19	Gonzalez-Montellano, C.. "Determination of the mechanical properties of maize grains and olives required for use in DEM simulations", Journal of Food Engineering, 201208 Publication	<1%
20	Submitted to Dr. Pillai Global Academy Student Paper	<1%
21	"Proceedings of the 7th International Conference on Discrete Element Methods", Springer Science and Business Media LLC, 2017 Publication	<1%
22	José Neves, António Correia Diogo, Ana Cristina Freire, Jorge de Brito. "Chapter 20 Aggregates", Springer Science and Business Media LLC, 2015 Publication	<1%
23	serc.carleton.edu Internet Source	<1%
24	www.brookfieldengineering.com Internet Source	<1%
	"Flow properties of bulk solids", Powders and	

25	Bulk Solids, 2007 Publication	<1%
26	Submitted to University of Huddersfield Student Paper	<1%
27	Maitraye Sen, Subhodh Karkala, Savitha Panikar, Olav Lyngberg, Mark Johnson, Alexander Marchut, Elisäbeth Schäfer, Rohit Ramachandran. "Analyzing the Mixing Dynamics of an Industrial Batch Bin Blender via Discrete Element Modeling Method", Processes, 2017 Publication	<1%
28	www.dgci.be Internet Source	<1%
29	R Pan. "Material properties and flow modes in pneumatic conveying", Powder Technology, 1999 Publication	<1%
30	Submitted to Universität Stuttgart Fakultät Bau Student Paper	<1%
31	epdf.tips Internet Source	<1%
32	drum.lib.umd.edu Internet Source	<1%
33	Submitted to University of Leeds	

	Student Paper	<1%
34	G.E. Klinzing, F. Rizk, R. Marcus, L.S. Leung. "Pneumatic Conveying of Solids", Springer Science and Business Media LLC, 2010 Publication	<1%
35	Submitted to University of Birmingham Student Paper	<1%
36	Hamzah M. Beakawi Al-Hashemi, Omar S. Baghabra Al-Amoudi. "A review on the angle of repose of granular materials", Powder Technology, 2018 Publication	<1%
37	Submitted to University of Liverpool Student Paper	<1%
38	Submitted to Shri GS Institute of Technology and Science, Indore Student Paper	<1%
39	M. Lachi, N. El Wakil, J. Padet. "The time constant of double pipe and one pass shell-and-tube heat exchangers in the case of varying fluid flow rates", International Journal of Heat and Mass Transfer, 1997 Publication	<1%
40	Kapil Sharma, S.S. Mallick, Anu Mittal, Renhu Pan. "On developing improved modelling for	<1%

	particle velocity and solids friction for fluidized dense-phase pneumatic transport systems", Powder Technology, 2018 Publication	
41	S. P. Singh. "Factors affecting the productivity of loaders in surface mines", International Journal of Mining Reclamation and Environment, 3/1/2006 Publication	<1%
42	Submitted to University of Greenwich Student Paper	<1%
43	www.azom.com Internet Source	<1%
44	Engineering Computations, Volume 28, Issue 3 (2011-03-20) Publication	<1%
45	slideblast.com Internet Source	<1%
46	Lijun Wang, Rui Li, Baoxin Wu, Zhenchao Wu, Zhenjun Ding. "Determination of the coefficient of rolling friction of an irregularly shaped maize particle group using physical experiment and simulations", Particuology, 2017 Publication	<1%
47	"Computational Fluid Dynamics for Bioreactor Design", Bioreactors, 2016.	<1%

Publication

48	Submitted to Warrington Collegiate Student Paper	<1%
49	Jorge Loureiro, Jayr Amorim. "Kinetics and Spectroscopy of Low Temperature Plasmas", Springer Science and Business Media LLC, 2016 Publication	<1%
50	Submitted to Higher Education Commission Pakistan Student Paper	<1%
51	P. Stevenson. "Velocity of isolated particles along a pipe in stratified gas–liquid flow", AIChE Journal, 05/2002 Publication	<1%
52	can-am.net Internet Source	<1%
53	Submitted to PSB Academy (ACP eSolutions) Student Paper	<1%
54	Submitted to Cardiff University Student Paper	<1%
55	Submitted to University of Witwatersrand Student Paper	<1%
56	Ulrich Teipel. "Using DPM on the Way to Tailored Prismatic Spouted Beds", Chemie	<1%

	Ingenieur Technik, 03/2012 Publication	
57	Harold Brannon. "Using Industry Standards As a Way to Predict Sand Performance and Approve Sand Deposits: Is There a Catch 22?", Proceedings of SPE Annual Technical Conference and Exhibition ATCE, 09/2008 Publication	<1%
58	gbt.buildcentral.com Internet Source	<1%
59	shodhganga.inflibnet.ac.in:8080 Internet Source	<1%
60	Submitted to Central Queensland University Student Paper	<1%
61	www.uniassignment.com Internet Source	<1%
62	Submitted to North Carolina State University Student Paper	<1%
63	Submitted to Imperial College of Science, Technology and Medicine Student Paper	<1%
64	Submitted to Hacettepe University Student Paper	<1%
65	zombiedoc.com Internet Source	<1%

66	en.wikipedia.org Internet Source	<1%
67	Submitted to University of Limerick Student Paper	<1%
68	Submitted to University Of Tasmania Student Paper	<1%
69	nfogm.no Internet Source	<1%
70	Submitted to Tshwane University of Technology Student Paper	<1%

Exclude quotes	On	Exclude matches	< 10 words
Exclude bibliography	On		